12-14-2015

Tool Material Degradation Due to Friction Stir Welding of Aluminum Alloys

Corbin T. Collier
University of South Carolina - Columbia

TOOL MATERIAL DEGRADATION DUE TO FRICTION STIR WELDING OF ALUMINUM ALLOYS

by

Corbin T. Collier

Bachelor of Science
University of South Carolina 2014

Submitted in Partial Fulfillment of the Requirements

For the Degree of Master of Science in

Aerospace Engineering

College of Engineering and Computing

University of South Carolina

2015

Accepted by:

Anthony Reynolds, Director of Thesis

Addis Kidane, Reader

Lacy Ford, Senior Vice Provost and Dean of Graduate Studies

DEDICATION

Dedicated in loving memory of my late grandfathers, James Edward Corbin and Warren Thomas Collier.

ACKNOWLEDGEMENTS

The work presented here is in thanks to the support of Dr. Reynolds, the FSW research group, my family, and friends. The financial support for this work is from the Center for Friction Stir Processing (CFSP), a National Science Foundation (NSF) Industry/University Cooperative Research Center (IUCRC). This work is sponsored by Airbus, Kaiser Aluminum, Gulfstream Aerospace, and PAR Systems.

ABSTRACT

The purpose of this study is to investigate the friction stir welding (FSW) tool material degradation factors due variation in tool material properties and the effect of an aluminum diffusion wear mechanism on three different FSW tool material when exposed to various welding temperatures and times. The degradation factors are essential to FSW tool design due to the effect of the tool pin and shoulders on the heat generation and material flow which directly correlated to the weld quality created during the FSW process. For this investigation the three materials used are H13, TSP1, and MP159. To determine degradation factors the variations in microstructure, hardness, nominal impact energy, fracture surface of impacted specimens, surface roughness of impacted specimens, and the effect of aluminum diffusion on each of the materials is analyzed. The hardness test revealed that in the range of welding temperature and time exposure testing there is a hardness variation of 550-460 HV for H13, 550 - 526 HV for MP159, and 813-704 HV for TSP1. The Izod testing concluded that MP159 requires the highest nominal impact energy to cause failure, correlating to the highest surface roughness, while TSP1 requires the lowest nominal impact energy to cause failure, which correlates to the lowest surface roughness. Based off of the fractography results all of the materials failed due to microvoid coalescence and this is proof of a ductile failure mechanism. Lastly, the aluminum diffusion experiments did show evidence an aluminum diffusion surface reaction in TSP1 and MP159 along with mechanical mix layers in each of the materials however, there is no proof of aluminum penetration along the tool materials' grain boundaries.

TABLE OF CONTENTS

LIST OF TABLES

LIST OF FIGURES

LIST OF SYMBOLS

δ	Fractional Slip Condition
ω	Tool Rotational Speed
r	Tool Radius
μ	Dynamic Viscosity
τ	Temperature-Dependent Shear Strength
σ	Temperature-Dependent Yield Strength
P	Normal Pressure
dA	Infinitesimal Area Element
M	Total Torque
M_T	Sticking Component of Torque
M_L	Sliding Component of Torque
F	Total Tool Traverse Force
F_S	Force Component of the Shoulder
F_P	Force Component of the Pin
P	Applied Vickers Hardness Force
d	Micro-Indentation Diagonal Length
A	Cross-Sectional Area of Izod Specimen
A_{circle}	Diameter of Izod Specimen
A_{sector}	Area of a Sector of a Cicle
$A_{triangle}$	Area of Triangle in Sector
$A_{segment}$	Area of Removed Segment

r	Radius of Izod Specimen
d	Notch Depth of Izod Specimen
β	Sector Angle
L	Evaluation Length
$Z(x)$	Profile Height Function
a_{pq}	Coefficient of the Polynomial Function
s	Least Square Equation
ω_g	Weight Function

List of Abbreviations

ABI ..... Automated Ball Indentation

BSE ..... Backscattered Electrons

CFD ..... Computational Fluid Dynamics

DHP ..... Deoxidized High Phosphorous

EDS ..... Energy Dispersive Spectroscopy

EHT ..... Extra High Tension

EsB ..... Energy Selective Backscatter

fcc ..... Face Centered Cubic

FE-SEM ..... Field Emission Scanning Election Microscope

FSW ..... Friction-Stir Welding

hcp ..... Hexagonal Close Packed

HRC ..... Rockwell Hardness C

RA ..... Arithmetic Average

RMS ..... Root Mean Square Average

SE2 ..... Type I Secondary Electrons

TMAZ ..... Thermomechanically Affected Zone

TSP ..... Thyseen Steel Powder Metallurgy

CHAPTER 1

INTRODUCTION

1.1 MOTIVATION FOR STUDY

Extensive research has been performed on the optimization of friction stir welding (FSW) processing parameters, material flow, and weld characteristics of aluminum alloys. This research has been the fundamental foundation leading to the growth of friction stir welding into the railroad, automobile, and aerospace industries, but there has been little investigation into the effects of tool pin and shoulder material degradation. It is essential to know what the leading causes of tool material wear, deformation, and failure are when a friction stir welding process is being performed on specific materials. Tool material degradation will vary greatly depending on which tool material is used and which base materials are being welded. Specifically for this study an analysis of H13, MP159, and TSP1 tool materials is conducted. The experimental results can be most accurately utilized for the friction stir welding of aluminum alloys, however, some of the results obtained can be applicable to other base metal when using an H13, MP159, or TSP1 tool material. The results obtained are for pin or shoulder tool temperatures between 400 °C to 525 °C which is a common temperature range for the FSW of aluminum alloys. It is the goal of this study to investigate the effect of aluminum alloy friction stir welding temperatures (400 °C to 525 °C) and welding times (1/2 hour to 50 hours) on the mechanical properties, such as

hardness and fracture toughness, of the tool materials along with the effect of aluminum diffusion causing tool material degradation and likelihood of failure.

1.2 Basics of Friction Stir Welding and Tool Importance

Friction Stir Welding (FSW) is a solid state joining process that was invented by the Welding Institute,UK in 1991 [1]. The process has been proven to optimize the weld characteristics and properties of adjoining metallic materials, primarily aluminum alloys, dissimilar materials, and harder steels. Since there is no bulk melting of the base materials many of the common problems associated with fusion welding, such as weld porosity, solidification cracking, and loss or dissociation of essential alloying elements are diminished [2]. A non-consumable tool pin and shoulder of a specific geometry is chosen for some specialized welding requirement and the tool is used to weld the material of choice using a set of process parameters. Some of the most essential process parameters for FSW are tool rotation speed, tool traverse speed, tool tilt, plunge force, and plunge depth.

The non-consumable tool is rotated and plunged into the base metals such that friction is created on the tool-base material interface. The friction will plasticize the base metal and the tool will then traverse along the joint line. For this reason the primary functions of the tool is to heat the welding area and to create the flow of material along the joint line [3]. The heating of the base material along with the tool rotation creates the plastic deformation that flows around the pin from the advancing side to the retreating side of the work piece. A schematic of the FSW process and terminology is seen in Fig. 1.1 [4]. Due to a reduction in energy and harmful gases the FSW process is considered to be an environmentally friendly alternative to conventional welding methods. No consumables are needed for the FSW process and it is predominantly used for butt and lap joints. The solid-state welding

process has shown to create substantial improvement in weld formation of aluminum alloys in comparison to standard fusion methods [4].

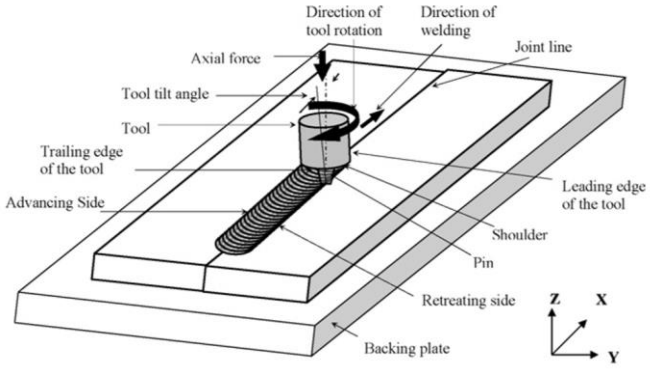

Fig. 1.1 Schematic of FSW Process and Terminology [4]

1.3 Loads Experienced by the Friction Stir Welding Tool

1.3.1 Overview

In order to create the most efficient friction stir welding tool the possible forces and loads experienced during the welding process must be thoroughly understood and accurately estimated prior to tool fabrication. Loads applied to the tool will vary greatly depending on welding parameters and tool geometry which will affect the weld flow characteristics and material properties in the plasticized region. The loads that are applied to tool pin and shoulder are due to the viscous and inertial effects determined by the axial, longitudinal, and lateral forces that the tool is subjected to during friction stir welding [5]. These forces are created during the translational motions of the initial plunge and lateral traversing along the weld line combined rotation of the tool through the plasticized material which creates axial compression, bending moments, and shear stresses in the tool. Lateral forces can also be contributed to the Magnus effect that creates a force perpendicular to the direction of linear motion. This is caused by the asymmetric flow field created around the

tool pin. This flow field is generated due to velocity and pressure gradients created when the material is traveling from the advancing side to the retreating side [5,6]. If the flow field and heat generation created by tool pin and shoulder are not sufficient then an increase in tool loading and resulting stress state will be observed leading to quicker degradation and premature tool failure.

1.3.2 Computational Numerical Analysis

Due to the complexity of the interactions during the welding process typical analytical and numerical analysis can lead to large deviations in stress calculations in comparison to the actual stress experienced by the tool and thus experimental analysis is commonly used to verify numerical assumptions. Chen and Kovacevic [7] used ANSYS parametric design to create a finite element code that could accurately estimate longitudinal and axial forces over time applied to a FSW tool that is welding 6061-T6 aluminum alloy and AISI 1018 steel. By only changing the travel and rotational speed, keeping tool geometry constant, and only assuming heat input due to frictional effects they were able to successfully estimate the forces at various points along the tool pin when comparing the numerical model to their experimental values. Similarly, Colegrove and Shercliff [8] used FLUENT, a computational fluid dynamics (CFD) package, to compare numerical values of traverse forces applied to a FSW tool to experimental values. The numerical results did not coincide with the experimental values for traverse forces and heat input but they were able to show that a 50% reduction in force can be achieved by tilting the tool pin about the normal axis in comparison to a pin that is positioned vertically perpendicular to a horizontal plate.

Artharifar, Lin, and Kovacevic [5] also use a CFD model to simulate the material flow and heat transfer during the friction stir welding process of 6061-T6 aluminum alloy in

which the FSW tool loads are analyzed when adjusting welding parameters. For this experiment temperature dependent material properties, a stick/slip condition, and a tilted right-handed one-way thread with a smooth concave shoulder is chosen and proven to give accurate results in comparison to experimental values. Numerical and experimental results showed that axial force varies with time and is maximized after the end of tool plunging due to axial compression leading to a work hardened material. Also a higher angular velocity and lower traverse velocity will lead to a higher axial compression. The axial compression however, will be counteracted by a lifting force created by the tool and will vary in magnitude depending on tool geometry. A graph of the change in axial force throughout the FSW process can be seen in Fig. 1.2.

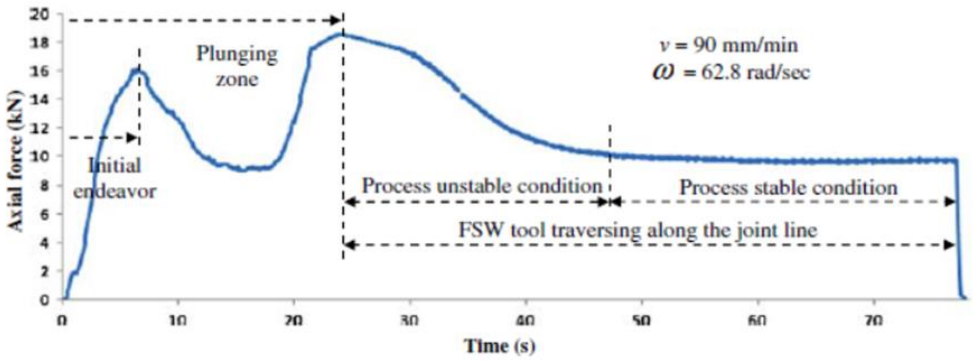

Fig. 1.2 Axial Force Applied to the FSW Tool [5]

Artharifar, Lin, and Kovacevic [5] also determined the effect of the forces and moments on the tool pin and the tool shoulder due to inertial and viscous loading. In this case inertial loading is considered the resistance of the tool when being accelerated during the plunging and traversing motions creating a pressure field on the tool. The viscous loading in this case is considered the tools resistance to motion created by the rotation of the tool through the material that has a temperature dependent viscosity which will create shear stresses in the tool. Their research claimed that increasing rotational velocity will decrease

longitudinal inertia and viscous forces on the tool pin and shoulder due to an increase flow temperature causing a decrease in the viscosity in the thermomechanically affected zone (TMAZ). Conversely, higher weld travel speed will increase the lateral force due to an increase in pressure on the tool pin and shoulder. In both cases the axial force is dominated by inertia effects, lateral force and the moment applied are dominated by the viscous effects, and longitudinal force is affected at same level of magnitude for both inertia and viscous effects when altering welding parameters. While the trends for both pin and shoulder appear to be the same, the magnitudes of specific forces and moments created by the inertia and viscous effects vary greatly. The results claimed that the tool shoulder experiences a higher level of longitudinal, lateral, and axial force along with a higher moment applied when altering the welding parameters. Visual representation of these results can be seen in Fig. 1.3 for the tool pin and Fig. 1.4 for the tool shoulder.

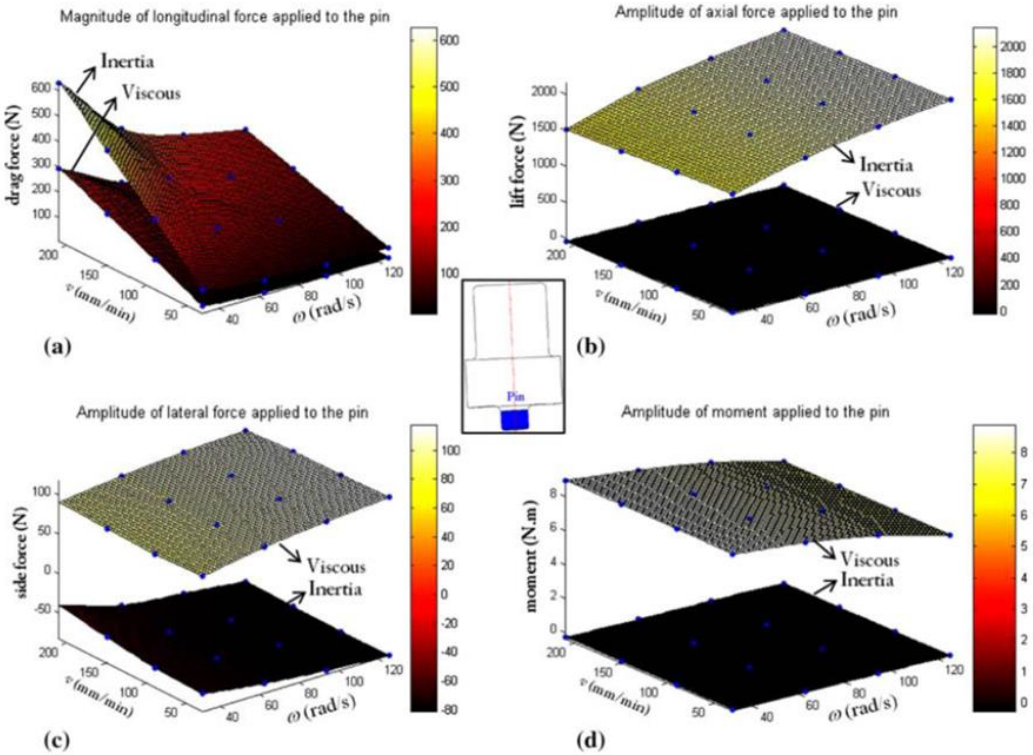

Fig. 1.3 Loads Applied to Tool Pin with Changing Weld Parameters [5]

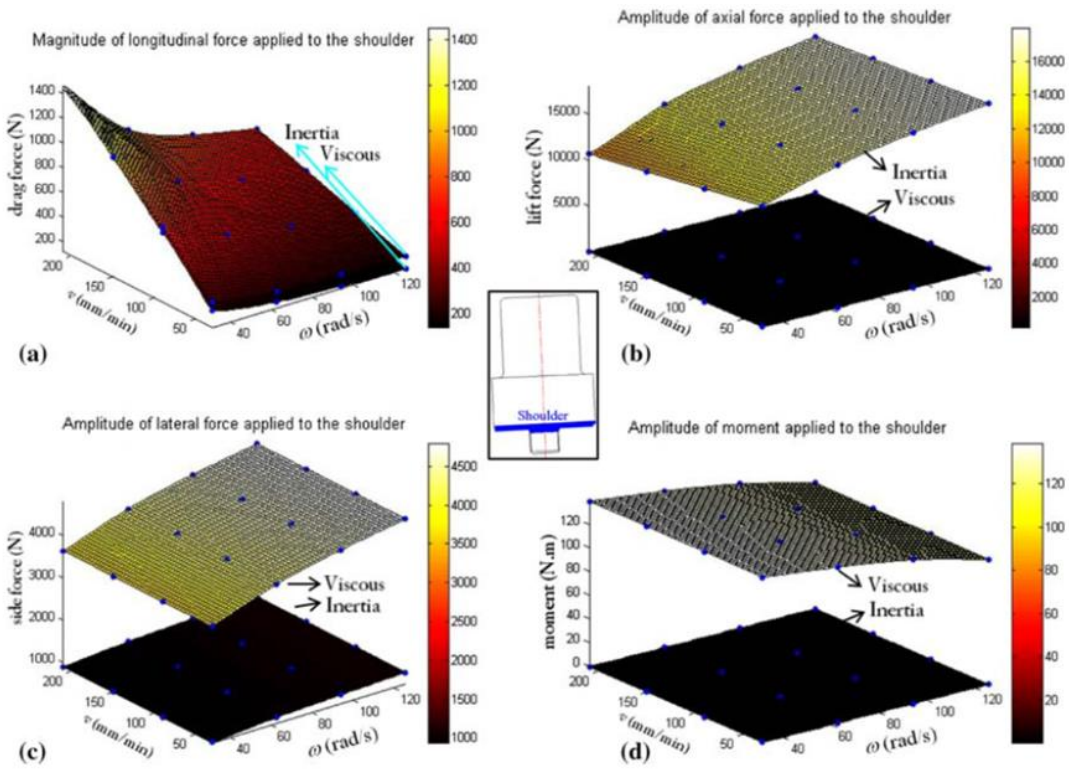

Fig. 1.4 Loads Applied to Tool Shoulder with Changing Weld Parameters [5]

1.3.3 Analytical Analysis

Another methodology of determining the forces, moments, and stresses on the tool is through analytical analysis. An accurate model of the loading criteria must be established and fundamental equations must be known, but if done properly a good estimation of the forces, moments, and stresses can be determined. Since the tool pin is the weakest member of the tool and experiences the most severe stresses at the highest temperatures due to bending and torsion it is critical that the loads and stresses be known at all points along the tool pin surface [9].

Accounting for every loading situation in an analytical analysis can be very cumbersome and for that reason analytical analysis can be simplified by only using a single force acting on the pin as the loading scenario to decipher how that single force

independently will affect the stress levels in the pin. This methodology is used by Arora and Mehta [9] to determine the forces, moments, and stresses due to bending and torsion created by a traverse force on the tool. In their experiment they use various welding conditions and tool geometries to simulate the FSW of AA2024, AA6061, and Ti-6A1-4V alloys but a constant flat shoulder and straight pin is used for simplified analysis. A schematic of the pin and loading condition can be seen in Fig. 1.5.

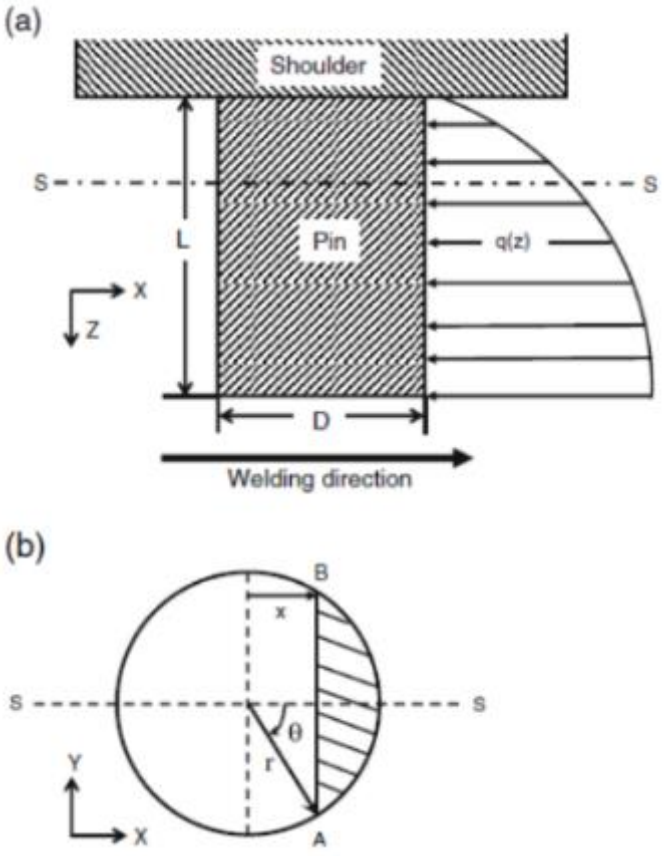

Fig. 1.5 Schematic of Pin & Loading Condition (a) Cross-Section at S-S (b) [9]

Arora and Mehta [9] showed that torque (in-plane moment) and force on the tool could be analytically calculated as long as the torques and forces applied accounted for the fractional slip condition (δ), tool rotational speed (ω), tool radius (r), dynamic viscosity (μ), temperature dependent shear strength (τ), temperature-dependent yield strength (σ),

normal pressure (P), and infinitesimal area element (dA). The total torque (M) required is shown in Eq. 1.1 [10,11] where M_T and M_L are the sticking and sliding components of torque, respectively. Equations for M_T and M_L are shown in Eq. 1.2 and Eq. 1.3[10,11], respectively. The total tool traverse force (F) applied to the tool can be seen in Eq. 1.4 where F_S and F_P are the force components on the shoulder and pin, respectively. Equations for F_S, F_P, δ, and μ are shown in Eq. 1.5 – 1.8, respectively, where δ and μ are valid through $0.1\ m/s \leq \omega r \leq 1.6\ m/s$ [12]. It is important to note, as stated in the name, that the temperature-dependent shear strength and yield strength will vary depending on the welding temperature and an example of the relationship between these variables and temperature can be seen in Fig. 1.6 [13]. As temperature increases shear strength of the H13 tool will decrease and typically this relationship is true for yield strength and dynamic viscosity as well at high temperature ranges. This means that as temperature increases the torque and force along with the components of torque and force will all decrease.

$$M = M_{\mathrm{T}} + M_{\mathrm{L}} \tag{1.1}$$

$$M_{\mathrm{T}} = \oint_{\mathrm{A}} r_{\mathrm{A}} \times (1-\delta)\tau \times d_{\mathrm{A}} \tag{1.2}$$

$$M_{\mathrm{L}} = \oint_{\mathrm{A}} r_{\mathrm{A}} \times \delta\,\mu P \times d_{\mathrm{A}} \tag{1.3}$$

$$F = F_{\mathrm{S}} + F_{\mathrm{P}} \tag{1.4}$$

$$F_{\mathrm{S}} = \oint_{\mathrm{A}} \delta \times \mu P \times d_{\mathrm{A}} \tag{1.5}$$

$$F_{\mathrm{P}} = \oint_{\mathrm{A}} \sigma \times d_{\mathrm{A}} \tag{1.6}$$

$$\delta = 0.31 \times \exp\left(\frac{\omega r}{1.87}\right) - 0.026 \tag{1.7}$$

$$\mu = 0.5 \times \exp(-\delta \omega r) \tag{1.8}$$

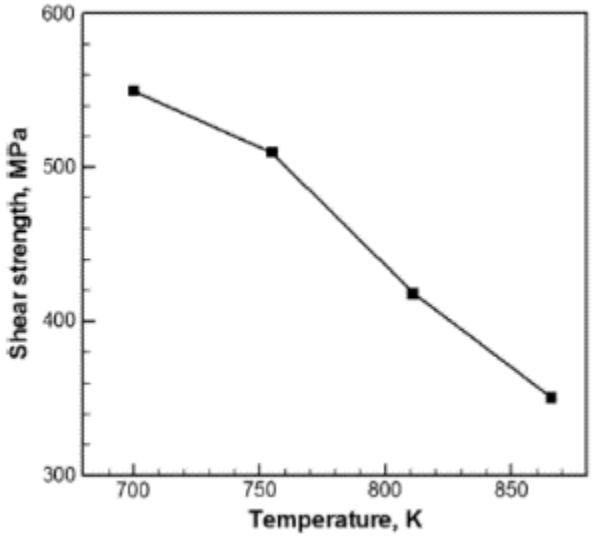

Fig. 1.6 Temperature Dependent Shear Strength vs Temperature of H13 Tool [13]

Arora and Mehta [9] also showed that simple solid mechanics based around cantilever beam theory can be utilized to calculate the torsional and bending stress in the pin with known values of the torque and force distribution (*q(z)*) that is acting against the traversing weld path. The bending moment (M_y) at point *A* shown in Fig. 1.5 can be calculated using Eq. 1.9 [14] where *z* is the distance from the pin root and *dz* is the infinitesimal distance. With known values of M_y the normal stress due to bending can be calculated, as shown in Eq. 1.10 [14], where *x* is the distance to the root cord of *AB* (shown in Fig 1.5 (b)), I_{yy} is the second moment of area, and θ is the angle from the line connecting the center of the pin to point A and the horizontal x-direction. With known values of the

sticking component of the torque (M_T), the radius of the pin (r), and the polar moment of area (J_{zz}) the torsional shear stress (τ_T) can be calculated, as shown in Eq. 1.11 [14]. The bending shear stress (τ_B) can also be calculated with known values of shear force (V), first moment of area (Q), second moment of area (I_{yy}), and the length of the chord AB (g), as shown in Eq. 1.12 [14]. With all bending and torsional stress components known the maximum (σ_1) and minimum (σ_1) principle stress can be calculated along with the maximum shear stress (τ_{max}), as shown in Eq. 1.13 [14] and Eq. 1.14 [14] respectively.

$$\mathrm{M}_y = \int_{z_1}^{L} z\, q(z)\, dz \tag{1.9}$$

$$\sigma_{\mathrm{B}} = \frac{M_y x}{I_{yy}} = \frac{M_y (r\, \cos\theta)}{\pi r^4/4} = \frac{4\, \cos\theta}{\pi r^3} \int_{z_1}^{L} z\, q(z)\, dz \tag{1.10}$$

$$\tau_{\mathrm{T}} = \frac{\mathrm{M}_{\mathrm{T}}\, r}{J_{zz}} = \frac{M_{\mathrm{T}}\, r}{\pi r^4/2} \tag{1.11}$$

$$\tau_{\mathrm{B}} = \frac{VQ}{I_{yy} g} = \frac{4}{3} \frac{\sin^2\theta}{\pi r^2} \int_{z_1}^{L} q(z)\, dz \tag{1.12}$$

$$\sigma_{1,2} = \frac{\sigma_{\mathrm{B}}}{2} \pm \sqrt{\left(\frac{\sigma_{\mathrm{B}}}{2}\right)^2 + (\tau_{\mathrm{B}} + \tau_{\mathrm{T}} \sin\theta)^2 + (\tau_{\mathrm{T}} \cos\theta)^2} \tag{1.13}$$

$$\tau_{\max} = \frac{\sigma_1 - \sigma_2}{2} = \sqrt{\left(\frac{\sigma_{\mathrm{B}}}{2}\right)^2 + (\tau_{\mathrm{B}} + \tau_T \sin\theta)^2 + (\tau_{\mathrm{T}} \cos\theta)^2} \tag{1.14}$$

From the results of Arora and Mehta [9] the total traverse force will increase with pin length, shown in Fig. 1.7 (a), but as determined by Sorensen and Stahl [15] the total traverse force is not affected by pin diameter, shown in Fig. 1.7 (b). However, as the pin diameter increased the maximum shear stress would decrease in the tool and this relationship is shown in Fig. 1.8 (a) [9]. The opposite response was determined when comparing the maximum shear stress to the pin length. An increase in pin length resulted in an increase

in the maximum shear stress, as shown in Fig. 1.8 (b) [9]. When designing a tool it is recommended that the calculated maximum shear stress and principle stress be multiplied by a reasonable factor of safety and this value with factor of safety should always fall underneath the yield stress of the tool material. Also since the normal bending stress and torsional shear stress can be represented by a sinusoidal function this means that the maximum and minimum shear stress value will occur in every rotation of the tool leading to a dynamic loading cycle that must be accounted for when analyzing tool failure modes.

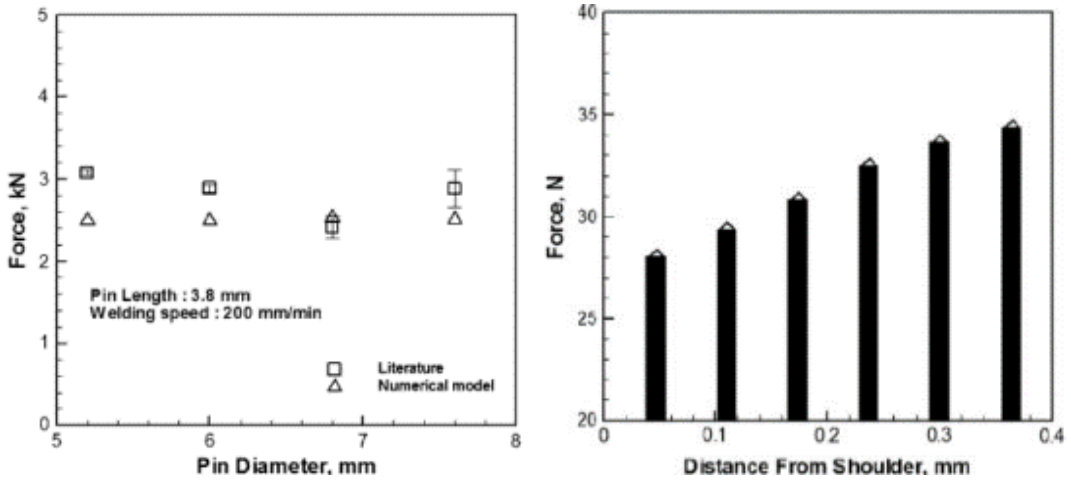

(a) **(b)**

Fig. 1.7 Effect of Pin Diameter (a) [9] & Pin Length (b) [15] on the Traverse Force

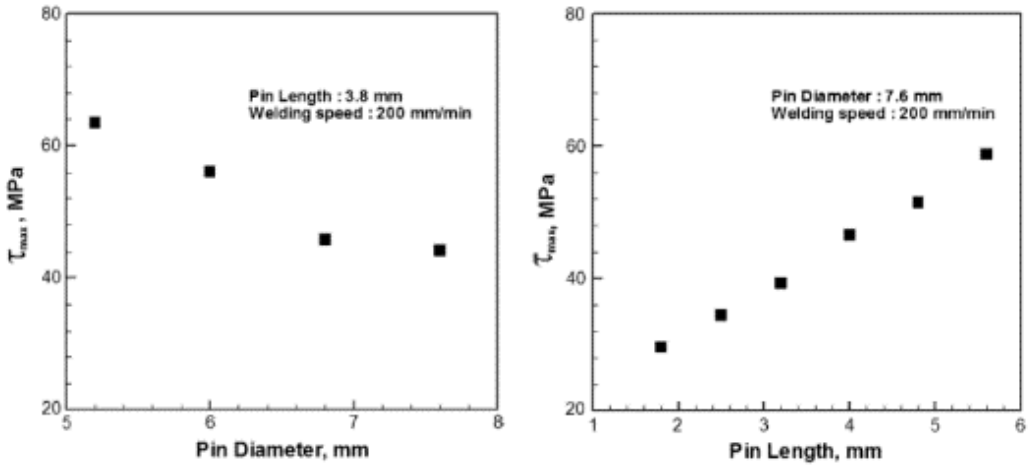

(a) (b)

Fig. 1.8 Effect of Pin Diameter (a) & Pin Length (b) on the Maximum Shear Stress [9]

1.4 Tool Geometry and Wear

1.4.1 Overview

During FSW heat is generated as the tool is rotated and plunged into a base materials. As heat is generated the material plasticizes and flows around the tool making the tool geometry a critical component in material flow characteristics and process parameters. Defects in the tools can have adverse effects on the quality of the weld and can lead to tool failure as the pin and shoulder are exposed to extreme heat and stress due to the required mechanical deformation of the weld. Various different tool geometries have been proposed for the FSW of aluminum alloys such that a defect-free weld with desired properties is obtained. Geometrical variation in the shoulder and pin play a critical role in the heat generation in the weld by the tool which can affect the loading of the tool, process parameters, and the properties of the weld. If wear is present the asymmetrical flow regime can be affected and thus a defect-free weld cannot be obtained [4] because the proper pin-driven and shoulder driven flow is not achieved. Improper tool design, overloading of the tool, and hours of operation will lead to tool wear and eventually failure. Depending on the tool material choice and tool fabrication time consistent tool failure can become a costly process.

1.4.2 Tool Pin Geometrical Influence

The tool pin can be optimized by adjusting the tool shape and thread pattern such that quality weld properties and sufficient tool strength exist. Biswas and Kumar [16] showed that tapered tool pins can create a better quality weld with respect to the mechanical properties. In the investigation straight, tapered, trapezoidal, hexagonal, and a threaded straight pins were analyze and all of the pins were made from SS310 alloy. Grain

refinement was observed using every tool at the weld nugget zone but was the greatest in trapezoidal and tapered tools. The hardness value of the weld also was affected by the geometry of the pin and the highest hardness throughout the width of the weld was shown with cylindrical and hexagonal pins. However, the most critical variation was observed in the tensile testing of the weld strength where the hexagonal, 5mm cylindrical, trapezoidal, and hexagonal pins increase in ductility by 50% in comparison to the non-welded metal, as seen in Fig. 1.9.

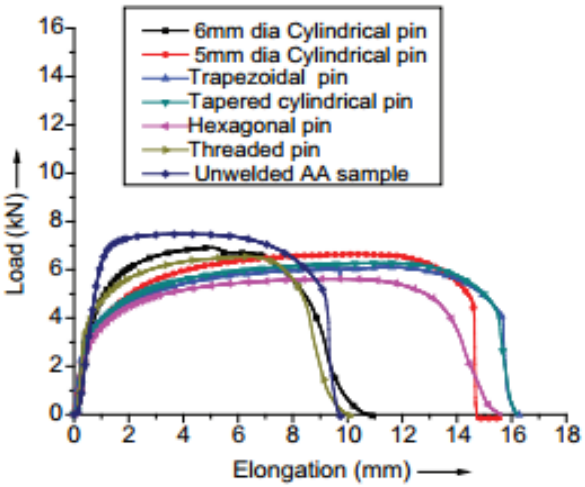

Fig. 1.9 Elongation vs Axial Load of FSW Tensile Specimens Welded using Various Tool Geometries [16]

Similar investigative studies have been conducted by Elangovan and Balasubramanian [17] where they wanted to study the microstructural details of the weld zone along with the tensile properties created in the weld using various shapes. The pin profiles chosen were straight cylindrical, tapered cylindrical, threaded cylindrical, triangular, and square. Due to the geometry of the pin and the process parameters various friction stir path zones were created producing good quality welds for all parameters and pins except for the straight cylindrical pin and tapered cylindrical pin. These pins showed a lack of heat generation and insufficient axial force causing weld defects due to improper material flow. Based off

of the results the most efficient tool was shown to be the square tool due to the fine microstructure that is created which leads to a higher hardness and yield strength of the weld. This is believed to be associated with the fact that flat faced profiles create higher eccentricity and there is a pulsating action created which allows for a finer stirring of the material from leading edge to trailing edge [18].

Right-handed threads vs left-handed threads were analyzed by Chowdhury and Chen [19] in which it was concluded that left-handed threads rotating clock-wise achieved the highest quality weld joints due to the fact that the hotter material will flow downward into the weld cavity due to the downward force created by the left-handed tool thread and rotation. This downward force also will decrease the required compressive axial force being applied to the tool. Various different thread variations have been created and are commonly used due to the belief that higher surface area will resort to an increase in heat generation due to the larger contact area, as shown in Fig. 1.10 [2]. The conical geometry with threads vs cylindrical with threads are analyzed by Buffa and Hau [20] using DEFORM3D, a 3D FEA software, for the estimation of material flow patterns and process variables. They revealed that larger pin angles will create a larger weld nugget and a more uniform temperature distribution which is a very valuable quality for the FSW of thicker plates. It was also concluded that the threaded conical pin when rotated would create a downward helical movement that would force material for the leading edge to the trailing edge which is ideal for uniform material flow and distribution.

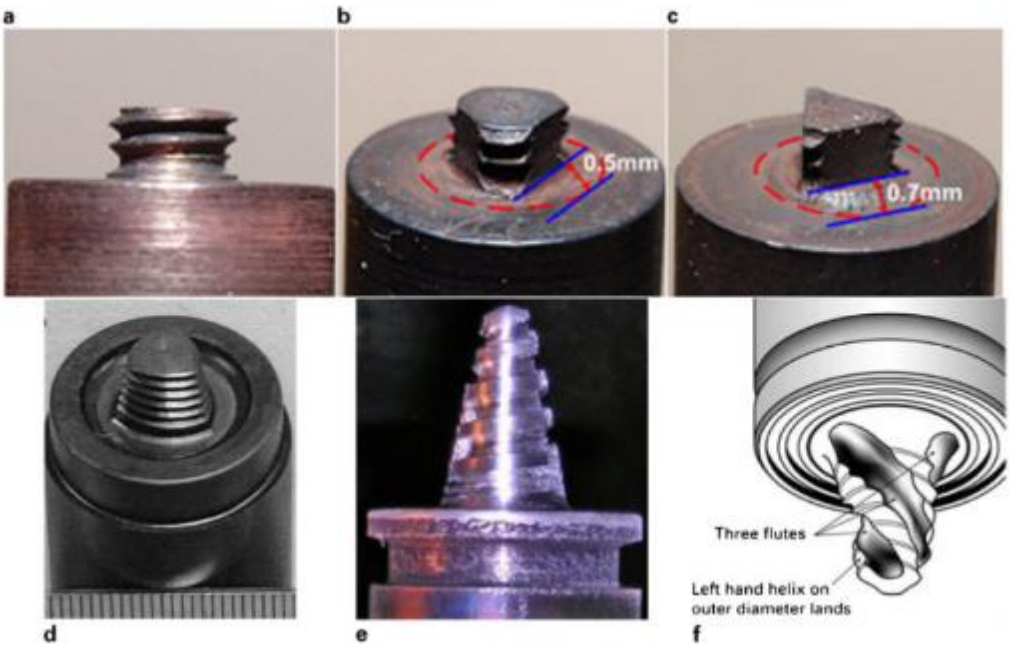

Fig. 1.10 Cylindrical (a), Three-Flat (b), Triangular(c), Trivex (d), Conical (e), Triflute (f) Threaded Pin Geometries

1.4.3 TOOL SHOULDER GEOMETRICAL INFLUENCE

The tool shoulder also contributes to the material flow [4] and is needed to coalesce the pin driven upward flowing material on the retreating side of the weld during the FSW process. The shoulder will contains the plasticized material in the weld cavity such that the upward material flow created by the pin at the retreating side of the weld will be driven back downward compressing against the advancing side material. If designed improperly the material flow field may not be established, creating defects in the weld or early tool failure due to an increase in stresses on the tool because of lack of heat generation creating plastic material flow. The shoulder also contributes to the heat generation in the weld [2] being the reason for the occurrence of defects if improper compressional force is applied during the FSW process. By modifying the shoulder diameter, the surface, and degrees of freedom various optimized tool shoulder design can be created.

Aurora and De [10] claimed that the effect of shoulder diameter could be numerically optimized using Eq.1.1-1.3 and they based their criterion on the principle of maximum utilization of torque for traction. This meaning that there is optimal surface diameter for specific process parameters that will obtain the highest possible strength weld. By changing the diameter of the shoulder components of the torque can be numerically calculated while an objective function (*O(f)*), shown in Eq. 1.15 [10], is used to calculate the optimum diameter. The sticking and sliding components of torque are critical to the flow path and flow stress and thus it is essential that these parameters are known to ensure proper parameters are used so that the highest quality weld can be achieved.

$$M = M_{\mathrm{T}} + M_{\mathrm{L}} \tag{1.1}$$

$$M_{\mathrm{T}} = \oint_{\mathrm{A}} r_{\mathrm{A}} \times (1-\delta)\tau \times d_{\mathrm{A}} \tag{1.2}$$

$$M_{\mathrm{L}} = \oint_{\mathrm{A}} r_{\mathrm{A}} \times \delta\,\mu P \times d_{\mathrm{A}} \tag{1.3}$$

$$O(f) = \left(\frac{M_T}{M_T + M_L} \times \frac{M_L}{M_T + M_L}\right) \tag{1.15}$$

The optimum shoulder diameter was shown to be the 18mm diameter which was rotated at 1200 rpm [10] when using the objective function composed of the sticking and sliding torque components. This was further confirmed by the results of Elangovan and Balsubramanian [21] where in there experimental investigation using five different tool pin geometries and three different shoulder diameters for the FSW of Al6061 aluminum alloy. The five tool pin geometries were straight, cylindrical, tapered cylindrical, triangular, and square with diameters fabricated at 15mm, 18, and 21 mm with a constant rotational speed

of 1200 rpm. Defect free welds were seen on all tools that contained an 18mm shoulder diameter and higher tensile properties were consistently observed. Metallographic images revealed that joints with the 18mm should diameter created fine, equiaxed grains with a uniform distribution of precipitates. The higher tensile properties and microhardness can be largely contributed to these precipitates that add strength into the matrix [21]. The variations in yield strength, ultimate tensile strength, percent elongation, and joint efficiency are shown in Fig. 1.11 (a), (b), (c), and (d) respectively, which all show maximum values at the shoulder diameter of 18mm for this specific material and welding parameters.

The impact of the shoulder geometry has also been investigated by Galvao and Leal [22] where they used flat, conical, and scrolled geometries while also varying the traverse and rotational speed of the tool that is used to weld 1-mm thick DHP (Deoxidized High Phosphorous) copper plates. It was concluded that flat shoulders require less torque than scrolled and conical but defects were observed in the in the flat shoulder due to improper material flow. The scrolled showed the best material flow characteristics producing the least amount of defects and also showed the highest level of grain refinement in the weld nugget. This grain refinements increases the tensile properties of the weld and also will increase the hardness. Flat shoulders consistently showed root defect, conical showed root defects and voids at 400 and 750 rpm but not at 1000 rpm, and root defect and voids were also seen in the scrolled at 400 rpm.

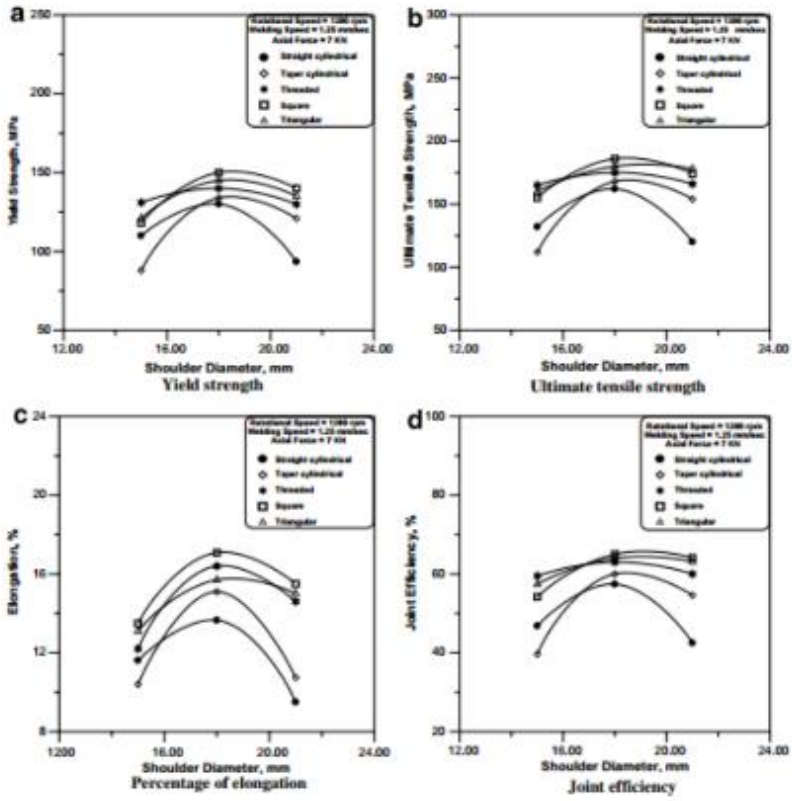

Fig. 1.11 Effect of Tool Shoulder Diameter on FSW Al-6061 Tensile Properties [21]

The effect of shoulder geometry was also experimentally tested by L. Cererqvist, C.D. Sorensen, and A.P. Reynolds [23] using 60 mm concave, 70 mm concave, 70 mm flat scroll, 70 mm convex scroll, and 70 mm convex-concave scroll as the tool should geometries. The results revealed the least amount of flash was obtained with the 70 mm convex shoulder while the flat scroll showed the highest level of flash. The concave shoulder also showed the lowest values of tool temperature and a reduction in over plunging of tool which can contribute to the decrease in flash. The convex scroll geometry also created more stable welds due to proper heat generation and material flow that is influenced by the shoulder geometry. This is due to the greater contact area between the base material and shoulder for convex geometries in comparison to concave and this greater contact area will affect the axial pressure imposed on the tool.

Conventional shoulders rotate with the tool pin however, the Welding Institute created a stationary shoulder that is non-rotating and simply slides along the base material [2] rather that rotate and slide like the conventional shoulder. Altering the sticking and sliding conditions of the tool will then affect the mechanical and thermal stress state due to variations in required torque and heat generation. The reason the Welding Institute created the stationary shoulder was to mitigate the high surface temperatures and thermal gradients that were believed to be created by during the FSW of low thermal conductivity alloys [24]. This was motivation for using the stationary shoulder as a method of improve the FSW of titanium alloys [25].

1.4.4 TOOL WEAR

The thermomechanical environment that the tool is exposed to during FSW will impose high mechanical and thermal stress states due to the applied forces, moments, and extreme temperatures that the tool is experiencing during friction stir welding. At high temperature the material properties of the tool will alter leading to a higher likelihood of tool degradation or potential failure [2]. If the yield strength or hardness decreases with the temperature then there is a higher risk of plastic deformation in the tool which will create unanticipated flow paths and an unknown tool geometry that is likely going to create inadequate welds depending on the severity of the deformation. Fracture energy can also be affected by the elevated temperature which will increase the likelihood of brittle failure. Tool wear may also potentially be contributed to diffusion of base materials, such as aluminum alloys, into tool metal causing tool defects and failure. Very little research has been conducted on the wear mechanisms of the tool materials and the relationship between degradation of tool materials and tool temperature.

Experimental investigations by Prado and Murr [26] have been conducted on tool wear of hardened steel right-hand threaded FSW tool pins and they measured the rate of wear for various traverse speeds but constant welding distance and rotation. Investigation concluded that a self-optimized shape is created that is capable of still producing defect-free welds that have satisfactory material properties throughout the cross-section of the weld. The creation of the self-optimized shape reveals the presence a wear mechanism in an area of high stress concentration due to the fact that loading conditions and thermal effects can alter that area's material properties even though the bulk of the material in the pin is not yielding. Greater deformation in the tool pin was seen at higher rotational speeds likely due to the increase in heat generation causing a drop in tensile properties at the tool surface. The progression of the tool shapes as the threaded pin is deformed and worn into to a smooth shaped pin is shown in Fig. 1.12 [26] where the traversing weld speed is 1mm/s, 3mm/s, 6mm/s, and 9mm/s as shown in (a), (b), (c), and (d) respectively.

Aluminum diffusion has also shown to be a degradation factor in FSW tools, as shown by Tarasov and Rubtsov [27]. The experiment was conducted to study the wear mechanism of a 1.2344X40CrMoV5-1 FSW tool when welding AMg5M aluminum alloys. The annealed aluminum alloy sheets are welded using a FSW tool with a 19mm shoulder diameter and a 6 mm pin dimeter. The tool was used to weld 2000 m of the aluminum alloy at 560 rpm using 2600 kg of plunge force and a feed rate of 500mm/min. A tribology approach is used to define the interaction of tool and base material sliding effects which can lead to plastic deformation and high heat output at the interface creating mechanically mixed layers of materials [28]. An iron/aluminum diffusion reaction is created due to the high thermal and mechanical effects on the FSW tool. This reaction and the chemical

composition of the affected area is observed using a Carl Zeiss SEM (Scanning Election Microscope) with EDS (Energy Dispersive X-ray Spectroscopy) capabilities. This leads to the formation of a brittle $FeAl_3$ intermetallic compound of continuous and spiked morphologies. The embrittlement created at the grain boundaries of the tool materials will increase likelihood of fracture under the severe stress that the tool surface is exposed to. Examples of the mechanically mixed layers can be seen in Fig. 1.13 [27] where the areas along the tool boundary appear to be a faded mix of the light and dark color signifying the presence of Fe-Al metallic compound.

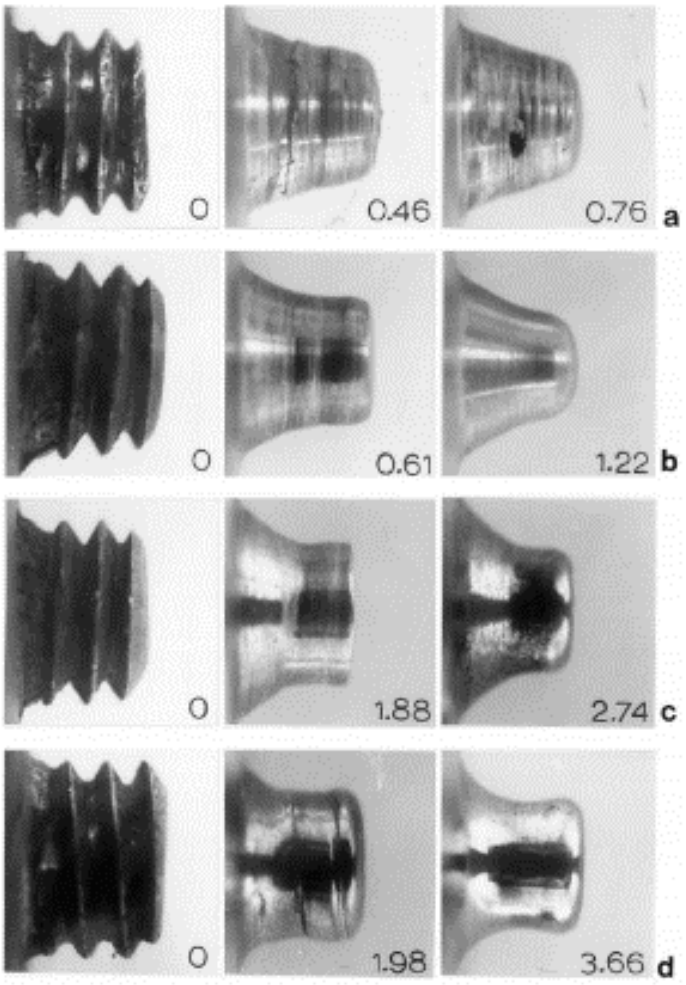

Fig. 1.12 Tool Wear Progression of Hardened Steel Pins FSW Al-6061 [26]

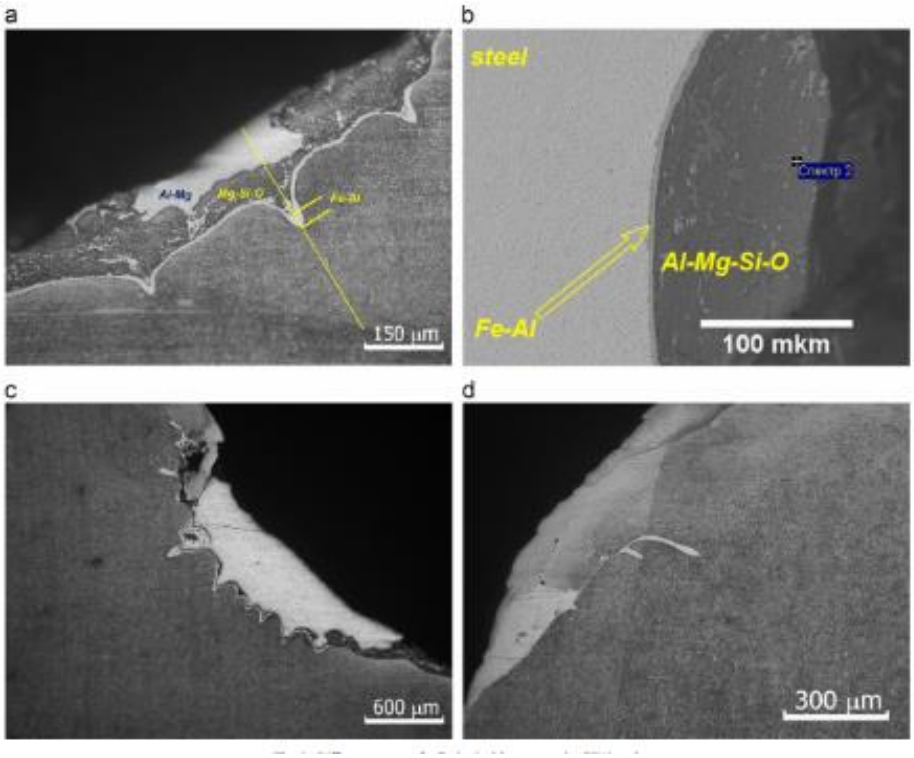

Fig. 1.13 Mechanically Mixed Layers on the FSW Tool Surface [27]

1.5 H13, MP159, AND TSP1 TOOL MATERIALS

Tool material selection is critical to the FSW tool pin and shoulder design. The choice of material to be welded will be a critical component to the tool material selection due to the variation in required heat generation and inertial forces imposed on the tool when welding materials ranging from aluminum alloys to titanium alloys. For the FSW of aluminum alloys the H13, MP159, and TSP1 tool materials exhibit the required material properties needed to sufficiently create a defect free weld under proper processing parameters. However, after substantial use or improper design degradation and failure of the tool will occur.

During the FSW process the welded material must heat up close to melting temperature such that a plasticized state is formed and higher melting temperatures are required when

welding steels in comparison to aluminum alloys. It is estimated that the maximum temperature typically reached during the welding is approximately 80% of melting temperature [16]. The amount of energy that it takes in order to reach this critical temperature will vary with the thermal conductivity and specific heat capacity of the material. Also yield strength, ultimate strength, hardness, and fracture toughness must be considered depending on the anticipated tool loading criterion that is dependent on the effectiveness of the tool to generate the required frictional heat and material flow. Due to the high temperature exposure the adjusted material properties due to thermal effects have to be considered to prevent tool degradation and potential failure. By adjusting the tool pin and shoulder material an optimization of weld quality, tool life, and cost can be achieve for the FSW of a specific base material.

1.5.1 H13

H13 is a 5% chromium hot work tool steel that is commonly used for hot work applications that require a high degree of toughness [29]. The microstructure of the hardened tool steel will consist of carbides, martensite, residual cementite, and possibly a small amount of retained austenite. The minimization of the retained austenite is optimal for FSW tool applications due to the fact that austenite is significantly softer than martensite which will deviate the material properties away from the desired values [30]. The formation of martensite and the presence of carbides, mostly chromium carbides, hardens the material preventing deformation in the structure. The chemical composition of H13 can be seen in Table 1.1 [31].

Table 1.1 H13 Element Composition [31]

H13 Element Composition	
Element	**Percentage (%)**
Carbon (C)	0.32 - 0.40
Chromium (Cr)	5.13 - 5.25
Iron (Fe)	≥ 90.95
Molybdenum (Mo)	1.33 - 1.40
Silicon (Si)	1.00
Vanadium (V)	1.00

Two metallographic images of an H13 microstructure is shown in Fig. 1.14 [32]. A lower hardness microstructure is shown in Fig. 1.14 (a) when a 843 °C austenitizing temperature is used which is followed by 7.45 °C/hr until 649 °C followed by air cooling which results in a hardness of 11-12 RC. A ferrite matrix with spherical chromium carbides is formed and observable when immersing etching the material in a Picral with HCl solution for 10 seconds. A higher hardness microstructure is shown in Fig. 1.14 (b) when a 543°C austenitizing temperature is used which is followed by an oil quench and double temper at 593 °C for 2 hours per temper resulting in a hardness of 47-48 RC. Due to the rapid cooling rate a matrix of martensite mixed with carbides is formed and optically observable when using Picral with HCl for 10 seconds for the etch [32]. For the friction stir welding of aluminum alloys a Rockwell C hardness of approximately 48 HRC has shown to provide sufficient weld quality and life time durability for a FSW tool.

The reason H13 is a favorable FSW tool material is due to its extreme toughness, good red hardness, high hardenability, and excellent wear resistance [29][31]. H13 is a hot work tool steel that is forged between 1149-899 °C and then annealed around 871 °C slowly cooling at a maximum rate of 22 °C/hr. At this time the material has a hardness of approximately 192-229 HBW on the Brinell scale but hardening and tempering using various methods can be used to achieve hardness value between 28-53 on the Rockwell C

scale (RC)[29][31]. Mechanical properties of hardness, ultimate strength, yield strength, elongation at break, modulus of elasticity, bulk modulus, Poisons ratio, machinability, and shear modulus at room temperature for a 55 RC H13 specimen are shown in Table 1.2 [31]. The thermal properties of coefficient of thermal expansion, specific heat capacity, and thermal conductivity are shown in Table 1.3 [31].

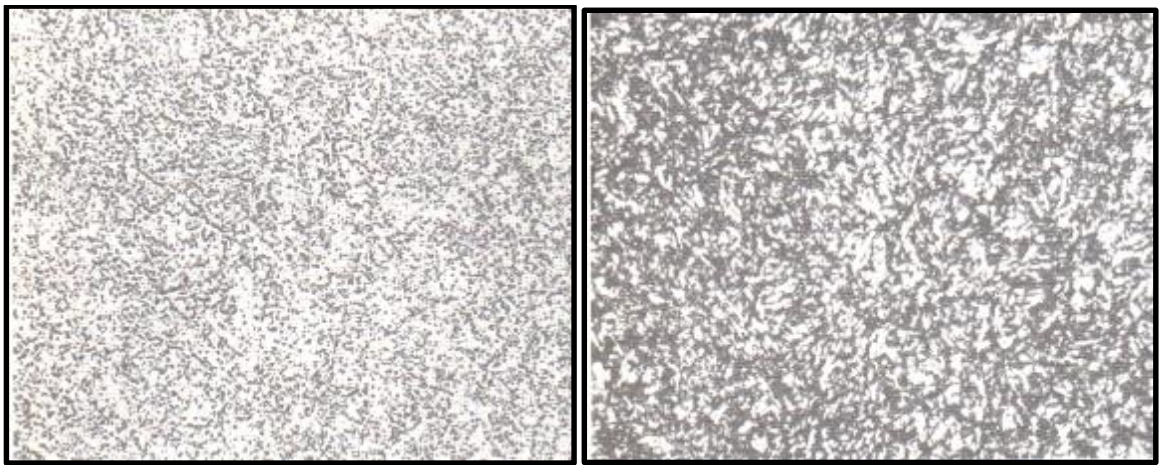

(a) (b)

Fig. 1.14 Metallographic Optical Images of H13 Microstructure [32]

Table 1.2 H13 Mechanical Properties at Room Temperature (55 HRC) [31]

H13 Mechanical Properties		
	Metric	**English**
Hardness (Rockwell C)	28-54	28-54
Ultimate Strength	1,900 MPa	289,000 psi
Yeild Strength	1,650 MPa	239,000 psi
Elongation at Break	9.0%	9.0%
Modulus of Elasticity	210 GPa	30,500 ksi
Bulk Modulus	160 GPa	23,200 ksi
Poissons Ratio	0.3	0.3
Shear Modulus	81 GPa	11,700 ksi

Table 1.3 H13 Thermal Properties at Room Temperature (55 HRC) [31]

H13 Thermal Properties		
	Metric	**English**
Coeffiect of Thermal Expansion	11.0-12.4 µm/m-°C	6.11-6.89 µin/in-°F
Specific Heat Capacity	0.460 J/g-°C	0.110 BTU/lb-°F
Thermal Conductivity	24.3-24.7 W/m-K	169-171 BTU-in/hr-ft^2-°F psi

1.5.2 TSP1

TSP1 is a semi-medium speed steel alloy that is manufactured using a power metallurgy production process [33]. The relatively new tool steel was invented by the Thyssen Krupp corporation in Essen, Germany and the term "TSP" stand for T=Thyssen, S=Steel, and P=Powder Metallurgy [34]. Very little research has been conducted on TSP1 with the exception of what has been published by Thyssen Krupp. TSP1 is the toughest of the TSP family but the toughness come at a cost of the wear resistance. The material matrix of a TSP1 tool steel with Rockwell C hardness between 56-65 HRC will consist of martensite with a fine distribution of carbides and retained austenite [30]. The carbides present in TSP1 that contribute strongly to the high toughness and wear resistance are Vanadium, Niobium, Molybdenum, and Chromium. The high carbon content allows for ductility in material and contributed the high tensile and compressive strength [34]. The element composition of TSP1 can be seen in Table 1.4 [33].

Table 1.4 TSP1 Element Composition [32]

TSP1 Element Composition	
Element	**Percentage (%)**
Carbon (C)	0.8
Chromium (Cr)	6.2
Iron (Fe)	84.9
Molybdenum (Mo)	3.0
Cobalt (Co)	3.0
Vanadium (V)	1.10
Niobium (Nb)	1.00

Two metallographic images of the microstructure of similar materials to TSP1 are shown in Fig. 1.15. A slightly harder material than TSP1 is shown in Fig. 1.15 (a) [33] and this material is a part of the TSP family, TSP5. TSP5 has higher carbon content than TSP1 and also contains Tungsten while TSP1 does not [35]. TSP5 used the same powder

metallurgy production process as TSP1 and the only main difference is that a higher austenitizing temperature must be obtained in TSP5 in comparison to TSP1 to ensure the proper hardening of the material. A fine grained, uniformly distributed matrix of various carbides mixed with retained austenite and martensite can be optically seen in the microstructure. Another similar powder metallurgy metal is M2 which is a Molybdenum high speed tool steel and is shown in Fig. 1.15 (b) [30]. M2 has a higher Molybdenum content and also contains Tungsten however, the iron content is very similar and along with production process of the powdered steel. The M2 material shown in the image was pressed at 550 MPa and vacuum sintered for an hour at 1240 °C. Molybdenum carbide particles can be seen throughout the matrix of retained austenite and martensite. In order to obtain this image a 5% nital solution was used for an etching solution. Images of TSP1 could not be obtained but due to the similar material compositions and manufacturing processes between TSP1, TSP5, and M2 the microstructure will be very similar.

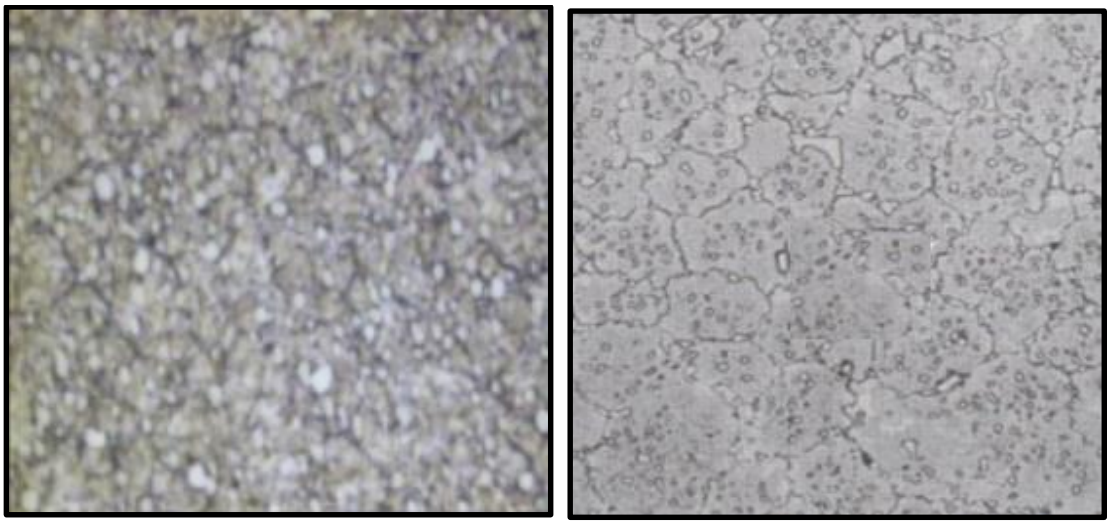

(a) (b)

Fig. 1.15 Metallographic Optical Images of TSP5 (a)[30] and M2 (b)[32] Microstructure

The TSP1 material is optimal for FSW due to the excellent toughness, high resistance to compression, and good hot work hardness [35]. TSP1 is manufacture by Thyssen Krupp Materials France in a production process that ensures a fully isotropic material of high quality and consistence. The metal is first melted in an induction furnace and then refined and degassed to purify the material. A nitrogen beam is then used to atomize the liquid steel into droplets that solidify and form fine metal powders that are a few thousandth of a millimeter in diameter. The powder is then encapsulated and the air is removed from the capsule before hot isostatic pressing is performed. A pressure of 1000 atmospheres and temperature of 1150 °C is obtained creating a tight steel block from a single quality of powder. The block is then preheated in three stages from room temperature to 400 °C then to 850 °C then to 1030 °C followed by an oil quench to 550 °C and then an air cool to room temperature. After austenitizing and quenching a tempering operation is then preformed in three stages. Each tempering involves the heating of the material between 520-550 °C and held at that temperature for two hours. Depending on tempering temperature a Rockwell C hardness of 59-63 HRC is obtained [32][35].

1.5.3 MP159

MP159 is a nickel-cobalt alloy and was developed as a fastener alloy that could operate at the high temperature in turbine engines [36][37]. By work strengthing the material through extruding, rolling, or drawing an intial strengthening mechanism is created where an hcp (hexagonal close packed) phase is formed in thin platelets approxiamately 2-100 nanometers in thickness on the planes of the annealed fcc (face centered cubic) matrix by mechanical deformation. This phase change can only happen though mechanical deformation and will not occur with any level of heat treatment. A secondary strengthening

mechanism is performed through age harding when the material will experience participation hardening due to the aluminum, titanium, and niobium present in the material composition [36][37]. The element composition of MP159 is shown in Table 1.5 [36].

Table 1.5 MP159 Element Composition [36]

MP159 Element Composition	
Element	**Percentage (%)**
Nickel (Ni)	25.5
Cobalt (Co)	35.7
Chromium (Cr)	19.0
Iron (Fe)	9.0
Molybdenum (Mo)	7.0
Titanium (Ti)	3.0
Niobium (Nb)	0.6
Aluminum (Al)	0.2

Two metallographic images of the microstructure of a MP159 round bar are shown in Fig. 1.16 [36]. Once MP159 is annealed an fcc phase is formed and a microstructure with uniform grain size and distribution is created, as shown in Fig. 1.16 (a) [36]. Grain twinning can also be observed in the microstructure and this is created when the boundaries of two crystals have an intergrowth and share at least one common plane. The material in this state has a Rockwell hardness of about 20 HRC. In order to obtain this metallographic image fine polishing and Frys plus HCl etch is used to reveal the microstructure. When cold worked the uniform grains from the annealed state will be stretched and elongated. This is evident by the metallographic image of the cold worked and aged MP159 specimen where grain boundaries and twinning is still present but the microstructure is deformed, as shown in Fig. 1.16 (b) [36]. The combination of the precipitates formed after age hardening and the hcp platelets gives the MP159 material a high thermal stability such that material properties are consistent up to temperatures approaching 600 °C. For this specimen a Frys plus HCl etch was used to reveal the microstructure.

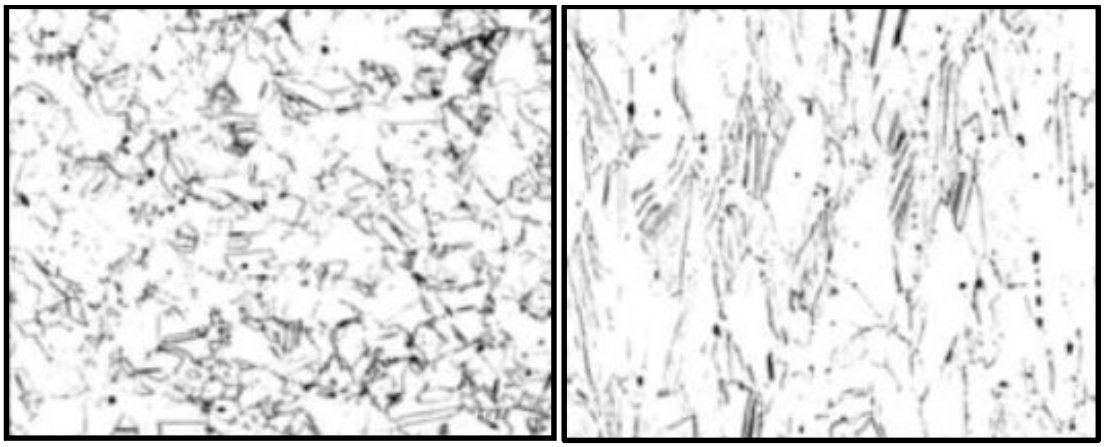

(a) (b)

Fig. 1.16 Metallographic Optical Images of MP159 Microstructure [36]

MP159 was designed to have a high strength, creep resistance, ductility, and corrosion resistance at high temperatures making the tool material ideal for the FSW process [38]. The optimal chemistry of MP159 is achieved through vacuum induction melting that is then followed up by a vacuum arc remelting process. This allows for a tightly regulated solidification process and the removal unwanted gasses that could potentially lead to unwanted defects and chemistry [37]. The material is then annealed by heating to 1040-1050 °C and held at this temperature for four hours followed by an oil or water quench to room temperature. The material is then cold worked through various possible manufacturing processes creating the initial work hardened strengthening mechanism. An age hardening process is then performed by heating the material to 660 °C and holding for four hours followed by an air cooling [36]. This creates a secondary hardening mechanism in the material through participation hardening resulting in excellent mechanical and thermal properties for the FSW of aluminum alloys. The tool material will maintain its structural integrity at temperatures below the age hardening temperature. The mechanical properties of hardness, ultimate strength, yield strength, elongation at break, modulus of

elasticity and shear modulus are shown in Table 1.6 [36] and the thermal property of coefficient of thermal expansion is shown in Table 1.7 [36].

Table 1.6 MP159 Mechanical Properties at Room Temperature (50 HRC) [36]

MP159 Mechanical Properties		
	Metric	**English**
Hardness (Rockwell C)	48-52	48-52
Ultimate Strength	840 MPa	123,000 psi
Yeild Strength	400 MPa	58,000 psi
Elongation at Break	12.0%	12.0%
Modulus of Elasticity	208 GPa	30,200 ksi
Shear Modulus	75.8 GPa	11,000 ksi

Table 1.7 MP159 Thermal Properties at Room Temperature [36]

MP159 Thermal Properties		
	Metric	**English**
Coeffiect of Thermal Expansion	14.3 µm/m-°C	7.94 µin/in-°F

CHAPTER 2

EXPERIMENTAL PROCEDURES

The following is a description of the experimental procedures used in the initial heat treatment, metallographic mapping, hardness testing, Izod fracture energy testing, and aluminum diffusion testing of the H13, MP159, and TSP1 tool materials.

2.1 INITIAL HEAT TREATMENT

2.1.1 H13 HEAT TREATMENT

The H13 tool steel is ordered from Cincinnati Tool Steel Company and is received by the University of South Carolina Mechanical Engineering Department in a non-heat treated state where the Rockwell C hardness is approximately 25 HRC. In order to be used as a FSW tool a Rockwell C hardness of approximately 48 HRC is needed and thus a heat treatment to harden the material must be performed. The H13 was ordered in ten foot lengths and ½" round rod was chosen for the metallographic mapping, hardness testing, and Izod fracture energy testing. The rods needed to be cut into lengths of approximately 18" using a SampleMet 2 abrasive cutter, shown in Fig. 2.1 (a), such that the rods can be fit into a Blue M convection oven for heat treatment, shown in Fig. 2.1 (b). The abrasive cutter uses a 9" cut off wheel ordered from MetLAb that is capable of cutting materials with hardness values 60+ HRC. The abrasive cutter provide constant cutting fluid to the wheel and a relatively smooth and quick cut can be made on the hard tool materials. The Blue M convection oven is heated to 980 °C and once preheated the rods are cleaned,

using common hand soap, and are inserted into the oven using proper safety procedures and clothing. The rods are kept in the oven for 20 minutes and an oil quench using room temperature oil is used to rapidly cool the material. Precaution must be used when handling the rod and placing it in the oil bath since the hot rod is capable of briefly igniting some of the oil and must be quickly submerged in the oil and covered. Once the rod has cooled to room temperature the oil needs to be cleaned off using soap and hot water

(a) (b)

Fig. 2.1 SampleMet 2 Abrasive Cutter (a) and Blue M Convection Oven (b)

2.1.2 MP159 HEAT TREATMENT

The MP159 tool material is received by the University of South Carolina Mechanical Engineering Department in a non-heat treated, cold drawn state, where the Rockwell C hardness is approximately 28 HRC. In order to be used as a FSW tool a Rockwell C hardness of approximately 52 HRC is needed and thus a heat treatment to harden the material is performed. The MP159 was ordered in five foot lengths and 0.515" round rod was chosen for the metallographic mapping, hardness testing, and Izod fracture energy testing. The same cutting procedure as H13 is used for the MP159. The Blue M convection

oven is heated to 660 °C and once preheated the rods are cleaned, using common hand soap, and are inserted into the oven using proper safety procedures and clothing. The rods are kept in the oven for 4 hours and then air cooled to room temperature.

2.1.3 TSP1 Heat Treatment

The TSP1 tool steel is ordered from Airbus, manufactured by Thyssen Krupt, and is received by the University of South Carolina Mechanical Engineering department in an already heat treated state where the Rockwell C hardness is approximately 62 HRC. The TSP1 was ordered in two foot lengths and 5/8" round rod was chosen for the metallographic mapping, hardness testing, and Izod fracture energy testing. No additional heat treatment is needed for TSP1 to be used as a FSW tool and section 1.5.3 can be referred to for the annealing and tempering heat treatment process perform by Thyssen Krupt.

2.2 Metallographic Mapping

2.2.1 Mounting

Each of the three materials are cut using the abrasive cutter into 1/4" thick disks that have to be finely polished and etched in order to obtained a sufficient metallographic image of the materials' microstructure. To simplify the polishing procedure the disks are mounting in an epoxy base, as shown in Fig. 2.2. In order to mount the three materials a two inch diameter cylindrical plastic mold is used. The plastic molds must be capped at one end and the face of the disk that is going to be used for the metallographic images must be placed on the center of the cap. A 1 to 5 ratio of hardener to epoxy must be used to ensure a structurally stable and sufficiently hardened mold. Each specimen needs approximately 30 grams of epoxy and 6 grams of hardener to fill the specific mold used. Plastic gloves are needed when making the mold so that bare skin does not get exposed to

the epoxy/hardener solution. Small paper cups are used to hold and mix the epoxy and hardener. In order to mix the epoxy and hardener solution a tongue suppressor is used such that the clear epoxy and dark yellow hardener appear to be completely uniform in color with minimal air bubbles.

Fig. 2.2 H13, TSP1, and MP159 Epoxy Base Mounts

The solution is then poured into the molds containing the specimens and left to harden at room temperature for at least two hours before being removed from the plastic mold. It is essential that there are no voids created on the interface between the epoxy mount and specimen because bleeding can occur when etching the alloys creating an unwanted stain on the microstructure. Some of the epoxy mounts can be difficult to remove from the mold so a vice, screw driver, and hammer were used to simplify the removal. A milling machine with a fly cutter tool is then used to shave a flat and level the bottom of the epoxy mount and reduce the height of the mount. The milling machine was set on high with a rotational speed of approximately 1200 rpm.

2.2.2 POLISHING

A very fine polish is required in order to achieve good quality metallographic images that are free from any contaminants, scratches, or uneven surfaces. Each specimen from all of the materials are polished in the same manner. A course grit wet polishing wheel must

be used initially and gradually finer grit wheels or powders are used. A medium rotation speed with a ½" diameter water flow is used. The first wheel used for polishing is a 120 grit wheel followed by 320 grit, 600 grit, 800 grit, and then a 1200 grit polishing wheel. To achieve an even higher quality of polish 5 micron then 3 micron alumina powder is used on the specimens. One scoop of the 5 micron alumina powder mix with one cup of water is used followed by a 3 micro alumina powder with water polish is used per specimen. The powder/water mixture is poured onto a fine round cloth that is rotated using a Crystal Master 8 automatic polishing machine. When polishing is completed the specimens are washed off with water and then washed with ethanol to help evaporate the water. The specimen is then blown air dried to ensure no water remains on the surface that could create oxidation effects, specifically in the H13 and TSP1 ferritic tool material. The specimen should have a mirror like surface in order to obtain good quality metallographic images.

2.2.3 ETCHING

A proper etch is essential to revealing the microstructure of the three tool materials and can be quite challenged due to their corrosive resistance property. The selection of the etch depends on the material composition, manufacturing processes, heat treatments, and desires microstructural artifacts that need to be observed. Etching works by attacking the material surface and removing specific inclusions but revealing grain structures, cold work deformations, and precipitation particles [39]. H13 and TSP1 are both ferritic tool steels and a 2% Nital immersion etch for a minute and a half followed by a ten second immersion in Viella's Reagent was used to reveal the materials microstructure. The 2% Nital is composed of 98 mL ethyl alcohol and 2 ml nitric acid. Viella's Reagent is composed of 5cc hydrochloric acid and 2 grams of picric acid. MP159 is a Ni-Co alloy and a Special #5

immersion etch for one minute was used to reveal its microstructure. Special #5 is composed of 20 mL hydrochloric acid and 4 mL peroxide. Proper safety precautions must performed at all time when handling hazardous materials. Gloves, safety glasses, and a face mask is recommended and the chemicals should be mixed underneath a venting hood at all times. Ensure that all chemicals are properly sealed after use and that they are placed in the designated chemical storage area.

2.2.4 IMAGING

The metallographic imaging was performed using a Keyence VHX-5000 digital microscope, shown in Fig. 2.3. For low magnification analysis a VH-Z20R lens was used for magnification ranges between 20x and 200x. For high magnification and high resolution imaging a VH-Z500R lens was used for magnification ranges between 500x and 5000x. The digital microscope is extremely advanced and can be used for various applications, but for this purpose the process was very simple. After turning on the machine an automatic calibration must be performed. Once the machine is properly calibrated all x, y, and z degrees of freedom can be control from the computer interface. If the specimen is evenly mounted, sufficiently polished, and etched properly then a good quality image is captured to obtain metallographic information about the tool microstructure.

Fig 2.3 Keyence VHX-5000 Digital Microscope

2.3 Hardness Testing

2.3.1 Tool Welding Temperature Exposure

Each of the three materials are again cut using the abrasive cutter into ½" thick disks and a range of welding temperatures and exposure times are used in order to examine the hardness variations throughout the temperature and time ranges. In order to simulate the tool welding temperature an AJAX Metal Pot Furnace salt bath is used to submerge the specimens, as shown in Fig. 2.4. The welding temperatures that have been chosen for experimentation are 400 °C, 450 °C, 500 °C, and 525 °C. At these temperatures welding exposure times are simulated for ½ hour, 1 hour, 5 hours, 20 hours, and 50 hours. These specimens that are exposed to the welding temperature and times are compared to each other and an initial sample that is kept at room temperature. This means that 21 disk must be cut for each material which will total to 63 specimens.

Fig. 2.4 AJAX Metal Pot Furnace Salt Bath

2.3.2 Hardness Testing Procedure

There are various methods of measuring material hardness values but for this experiment micro indentation methods were used. A Bühler MicroMET 1 Micro Hardness Tester, shown in Fig. 2.5, was used to obtain the Vickers hardness values of the specimens.

The Vickers hardness testing method involves the use of diamond indenter that is in the shape of a square pyramid. The indenter is compressed onto the material surface under a prescribed loading value by simply pushing only button on the central interface of the hardness tester. Due to that hard nature of the tool materials a load of 500 grams force is applied. Once the specimen has been secured in the tester and has been properly positioned using the magnifying lens, an indentation can be made. A square indentation will be left on the surface of the tool materials and the two diagonal lengths are measured in micrometers using the measurement tool on the hardness tester. The MP159 and H13 hardness was obtained using 13 indentation in a straight line at equal distance apart across the diameter of the specimen. TSP1 hardness was obtained using 15 indentation in a straight line due to the fact that the diameter of the TSP1 rods were slightly larger than the other two materials.

Fig. 2.5 Bühler MicroMET 1 Micro Hardness Tester

2.3.3 HARDNESS CALCULATIONS & ANALYSIS

The Vickers hardness value (H_v) can then be obtained using Eq. 2.1 [40] where P is the applied force and d is the average diagonal length. The hardness values were calculated in

Excel and graphs of hardness vs. position from the center of the rod were obtained. Once all test were complete for a specific material and temperature graphs of that hardness variations vs temperature exposure could be created with range bars indicating the variation in hardness at a specific temperature and time. Then when all temperatures and times have been analyzed graphs of the hardness variations vs time at each temperature can be created such that trends and discrepancies can be observed for the material. From this data critical information can be obtained for maximum and minimum hardness values that will decide the testing criteria for the Izod fracture energy testing.

$$H_v = \frac{1.8544P}{d^2} \tag{2.1}$$

2.4 Izod Impact Energy Testing

2.4.1 Izod Specimen Design

Izod impact testing is performed to determine how much energy it takes to fracture a material when a dynamic load is applied to specimen. The V-notch Izod impact test was chosen due to the simplification of the specimen fabrication. All of the tool materials have very high hardness values creating difficulty and adding complexity to the machining process. ASTM Standard E3 [41] recommends that for V-notch Izod testing a 11.4 mm diameter rod be used with a notch that is approximately 2 mm in depth. To avoid having to turn down each of the rods they were instead fabricated such that the diameter to notch depth ratio remain constant. The diameter to notch depth ratio is 5.7 meaning that the desired notch depth for H13, MP159, and TSP1 is 2.3 mm, 2.38 mm, and 2.86 mm, respectively. The vice dimensions in the Tinius Olsen impact testing machine required that the notch be located 31 mm from the bottom of the rod such that the notch center is adjacent to the top of the vice. This will maximize the affect of the stress concentration created by

the notch such that minimal plastic deformation occurs during failure. For the hammer of the impact tester to optimally contact the specimen a flat is needed at the top of rod that is approximately 2 mm in depth and 9-12 mm in length. A schematic of the cross section of an Izod specimen can be seen in Fig. 2.6 (a) with the required dimensions for each material shown in Table 2.1. The finished fabricated specimens can be seen in Fig. 2.6 (b) with H13 on the left, TSP1 in the middle, and MP159 on the right.

(a) (b)

Fig. 2.6 Izod Specimen Design

Table 2.1 Izod Specimen Dimensions for Machining

Material	A (mm)	B (mm)	C (mm)	D(mm)	E (mm)	F (mm)	R (mm)
H13	58.00	13.13	31.00	2.30	10.00	2.00	0.40
MP159	58.00	13.59	31.00	2.38	10.00	2.00	0.40
TSP1	58.00	16.28	31.00	2.86	10.00	2.00	0.40

2.4.2 IZOD SPECIMEN FABRICATION

The Izod specimens are initially cut from the stock round rods using the abrasive cutter to approximately 60 mm in length to account for the material loss needed for turning the ends of the rods down to ensure a level face and precisely machined specimen length. The flat of the specimens was fabricated using a manual surface grinder made by Abrasive Machine Tool Co., shown in Fig. 2.7. The surface grinder uses a magnetic feed table that moves the specimen left and right as it is clamped in an appropriate vice. A rotating

abrasive grinding wheel that can be adjusted up and down accurately to the thousandth of an inch can be adjusted in increments downward as the table translates the material. The material can then be accurately removed until the proper flat depth is achieved, This provides a precise and finely machine flat that is used for flush impact from the Izod pendulum striker.

Fig. 2.7 Abrasive Surface Grinder

After the flat is created the specimen needs to be faced on both ends of the rod so that a flat & level top and bottom surface is created and so that the specimen can be machined to the precise length. Due to the hard nature of the tool material high grade ceramic cutting inserts had to be purchased from Kennametal. For the facing a 35 deg Kenloc ceramic insert was used in the Bridgeport Romi EZ Path CNC Lathe, shown in Fig. 2.8, at 700 surface feet per minute, A CNC code is written and modified for each specimen depending on the material diameter and the length of the rough cut specimen. When the rod is completely turn down the required length a small metal point sometimes is still left in the very center of the rod. This excess material can simply be removed with a Drimal tool to create a completely flat rod end surface.

Fig. 2.8 Bridgeport Romi EZ Path CNC Lathe

ASTM E23 [41] recommends that a 45 degree with a 0.25 mm radius notch be fabricated in the specimen but due to complications with purchasing cutting inserts of this specification and required quality a 55 degree with a 0.40 mm radius ceramic cutting insert was used instead. For the fabrication of the Izod specimen notch a Bridgeport CNC Milling Machine is used, as shown in Fig. 2.9. As mentioned in Section 2.4.1 each of the three materials have a unique notch depth that must be altered for each CNC code. Small steps of approximately three thousandths of an inch are used to traverse the specimen and fabricate the notch depth with a rotational speed of 1400 rpm used for the modified fly cutter. The 55 degree Kenloc ceramic insert is attached to a 1.25" Kenloc boring bar that was also purchased from Kennametal. In order to use the fly cutter tool the boring bar diameter had to be turned down to 7/8" diameter so that the tool could be used in the milling machine with the available 7/8" collet. Proper alignment is essential when cutting the notch and can be achieved by ensuring the center of the notch is aligned with the plane of the flat. The alignment will create as best possible a degree of freedom bending moment that is experienced at the notch tip where stress concentrations will be the highest in the specimen.

Fig. 2.9 Bridgeport CNC Milling Machine

Once the specimens are completely fabricated the weld temperature and time exposure can be conducted in the same manner as the disks used in the hardness test. For the H13 and MP159 material five specimens where used per temperature and time and for TSP1 three specimens were used per temperature and time. The exposed specimens were all compared to an initial specimen that never received any additional heat treament. The temperatures and times of exposure were determined based off of the critical values obtained from the hardness results. H13 conducted the welding temperature and time exposure at 400 °C for 1 hour, 400 °C for 50 hours, 525 °C for ½ hour, and 525 °C for 50 hours. MP159 conducted the welding temperature and time exposure at 400 °C for 50 hours, 450 °C for 50 hours, 500 °C for 50 hour, and 525 °C for 50 hour. TSP1 conducted the welding temperature and time exposure at 400 °C for 5 hours, 400 °C for 50 hours, 525 °C for 1 hours, and 525 °C for 20 hours. Upon successful heat exposure at designated temperatures and times the specimens are measured using a digital caliper and Basic Bench Optical Comparator, shown in Fig. 2.10, which was used to accurately measure the difficult

measurement areas on the specimen, such as the notch depth and radius. An accurate measurement of the most highly loaded cross sectional area diameter minus crack length) is needed in order to normalize the impact energy readings for the three different diameter specimens. The stress is maximized at the central crack plane and thus the calculation of the cross sectional area is the measured diameter minus the crack length. The complete measurement table for H13, MP159, and TSP1 can be found in Table A-1, A-2, and A-3 of Appendix A respectively.

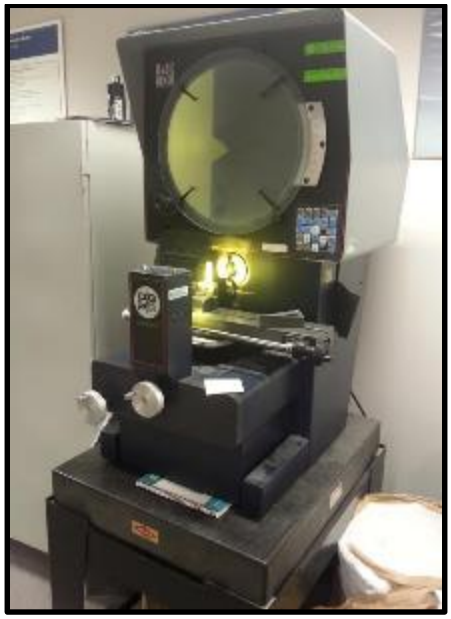

Fig. 2.10 Basic Bench Optical Comparator

In order to normalize the impact energy values the smallest cross sectional area is needed because the this cross sectional plane is the fracture initially occurs in the specimen. Each specimen had slighly varying diameters and crack depths but in order to obtain the most accurate result the impact energy needs to be normalized by that specific specimens fabricated dimensions. The area of the entire rod must be subtracted by the cross-sectional segment that has been removed from the rod to create the notch. in order to calculate the cross-sectional area of the specimen that is most highly exposed to the impact load, as

shown in Eq. 2.2. The segment is the area represented by the vertical line and slanted line patterned areas shown in Fig. 2.11. The rod is assumed perfectly circular and the area of the circle is shown in Eq. 2.3 where *r* is the radius that is measured for each specimen. The area of the segment is the area of the sector (horizontal lined area), minus the area of the two right triangles (slanted lined area) as shown in Eq. 2.4. The area of the sector is shown in Eq. 2.5 where β is calculated using Eq. 2.6 and *d* is the measured crack depth. The area of the triangles can be calculated with known β, *r,* and *d* values, as shown in Eq.2.7. With all known areas the cross sectional area *A* needed for normalization of the impact energy values can be calculated. All calculations were preformed in Excel.

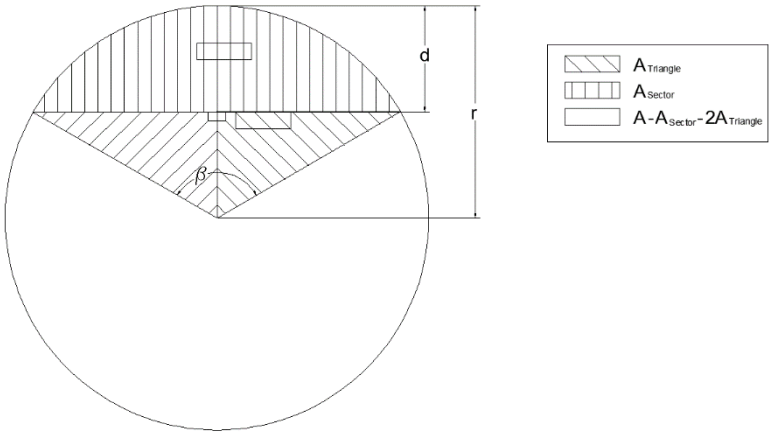

Fig. 2.11 Areas of Circle for Specimen Cross-Section Calculation

$$A = A_{circle} - A_{segment} \tag{2.2}$$

$$A_{circle} = \pi r^2 \tag{2.3}$$

$$A_{segment} = A_{sector} - 2 * A_{triangle} \tag{2.4}$$

$$A_{sector} = \left(\frac{\beta}{360}\right) * \pi r^2 \tag{2.5}$$

$$\beta = \cos^{-1}\frac{(r-d)}{r} \tag{2.6}$$

$$A_{triangle} = \frac{1}{2} * \sin\left(\frac{\beta}{2}\right) * r * (r-d) \tag{2.7}$$

2.4.3 IZOD TESTING PROCEDURE

The notched- bar Izod impact test was conducted using the Tinius Olsen Impact Tester, shown in Fig. 2.12 A heavy pendulum is used that can be locked in place at two different heights on the machine. At these heights there is a known value for the potential energy associated with the mass of the pendulum, the height, and gravitational constant. If properly calibrated a trial swing with no impact specimen can be performed and if the energy reading on the machine returns to zero after a full swing then it can be assumed to be properly calibrated. When then pendulum impacts the specimen there will be some energy absorption that takes place in the specimen before fracture and this magnitude of energy will directly correlate to the maximum height of the pendulum after impact. Since the Izod test is a cantilever beam test it takes less energy to fracture the materials in comparison to the Charpy test and because of this the lowest release point is be used. The ASTM Standard E-23 [41] can be referenced for a detailed description of all of the general requirement for the Izod testing.

Fig. 2.12 Tinius Olsen Impact Tester

Two critical component to the testing procedure is the clamping device used on the specimen and the impact striker attached to the pendulum. Upon impact no slipping can occur between the clamping device and the specimen otherwise false energy reading will be obtained and improper fracture may occur. Specialized clamping devices were made for the three materials out of A572 steel, shown in Fig. 2.13 (a). Using a 1.25" end mill on the milling machine the V-shaped grip was created to be universally used. Using a 17/32" end mill a cylindrical clamping grip was created for the H13 and MP195 materials and a 41/64" end mill was used for the TSP1. The impact striker is the large faced striker and is not to get confused with the U-shaped striker that is used for Charpy Testing. The impact striker was cleaned and briefly ground down to ensure a smooth and level impact with the specimen. The striker used for the Izod impact testing can be seen in Fig. 2.13 (b)

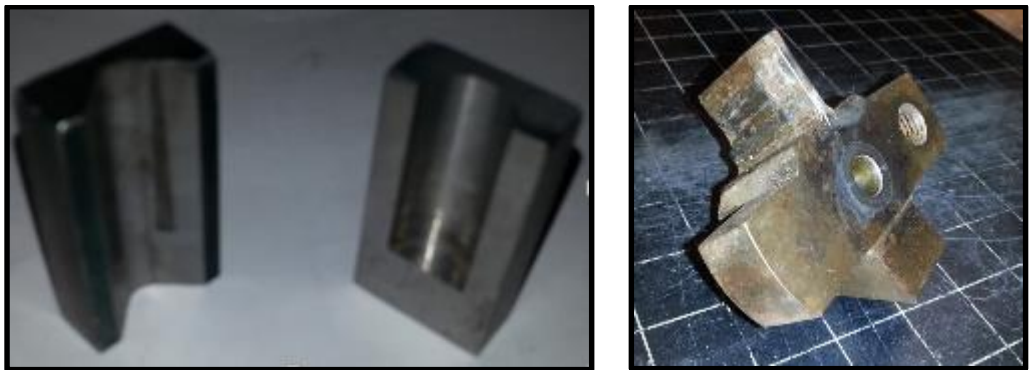

(a) (b)

Fig. 2.13 Izod Specimen Clamping Device (a) and Impact Striker (b)

Once the specimens are prepared, the clamping devices are fabricated, and the Izod apparatus is properly functioning and calibrated the testing can be performed. The Izod test is simply conducted by clamping the specimen such that the flat is parallel to the face of the striker and will be the point of contact between the pendulum and the specimen. If properly machined this should also be the position that aligns the swing direction with the centerline of the notch. The pendulum is locked in place and the energy meter is set at zero

pounds-force. The pendulum is then released without vibration and will impact the specimen. The specimen will absorb some of the energy and fracture will occur which will reduce the final maximum potential energy that can be achieved from the pendulum. After a full swing occurs the pendulum can be stopped using the electric brake and the value of the absorbed energy can be read from the impact tester.

2.4.4 FRACTOGRAPHY ANALYSIS

The fractography analysis is performed using the Carl Zeiss Ultra plus FE-SEM (Field Emission Scanning Electron Microscope), shown in Fig. 2.14, to determine the failure mode of each of the materials. To reduce the vacuum time it is recommended that before analysis the fracture specimen be shortened in length and this was done using the abrasive cutter. In order to begin using the SEM the Smart SEM software must be started and the chamber must initially be vented to release the pressure lock. Once the chamber is vented the specimens can be inserted on a locking stage and then the chamber can be closed and pumped back up to the required operating pressure. For these purposes the only tool bars needed are SEM Control and Stage Navigation.

This analysis required the use of the SE2 (Type II Secondary Electrons) detector and the optimal working distance for this detector is 8-10 mm which can be controlled with the stage navigation. In order for the detector to work the EHT (Extra High Tension) Voltage must be turned on and the voltage should be between 10-20 kV. All range of motion, magnification, focus, stagnation, aperture, brightness, and contrast can be control with the keyboard interface. Once a focused image is obtained the screen can be frozen and an image file can be saved. For this application images were taken at 100x, 1000x, 5000x, 10,000x, 25,000x, and 50,000x. Upon completion turn off EHT and vent the chamber. Remove the

locking stage when vented and always wear gloves so that the SEM chamber is not contaminated. Once the locking stage is removed the chamber can be pumped up and the software can be closed.

Fig. 2.14 Carl Zeiss Ultra plus FE-SEM

2.4.5 Surface Roughness Analysis

Using the Keyence VHX-5000 Digital Microscope a material surface roughness analysis of the fracture surfaces is conducted. An example of what the fracture surface of the initial H13 specimen looked like at 500x is shown in Fig. 2.15(a). Images of the fracture surface for each of the material are taken at the 200x, 500x, and 1000x magnifications. Instead of taking a normal picture the live depth up option is used which will create a 3D map of the area that is being focused upon, as shown in Fig. 2.15 (b). After the image is processed using the live depth up option a visualization of a 3D surface height map is created. As best possible the image is rotated such that the effects of a sloped surface can be neglected and a fairly accurate representation of the roughness can be observed. This process however is imperfect and a plane of best fit is needed to calculate the surface roughness. In order to extract this surface height data the Keyence installation software must be download so that the data can be extracted into an Excel file. The data consist of the pixel position vs the measured height. The pixel size for the 200x images is 1.113 μm,

for the 500x is 0.417 µm, and for 1000x is 0.208 µm. Based on the pixel position and known pixel size the *x* and *y* data can be calculated and the height values is considered the *z* data.

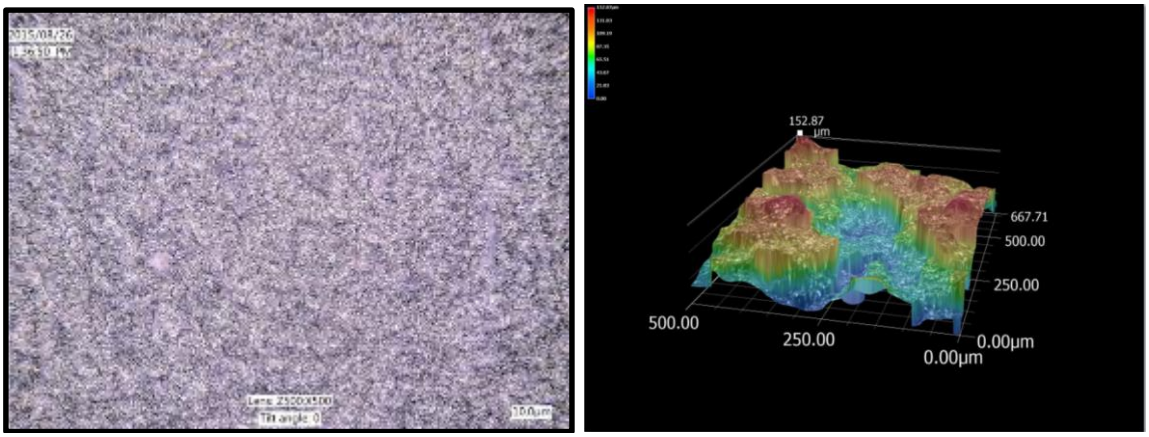

(a) (b)

Fig. 2.15 Image of Initial H13 Fracture Surface (a) w/ 3D Map of Surface Height (b)

In order calculate the surface roughness two different formulas are used. The first is arithmetic mean formula, shown in Eq. 2.8 [42], and is abbreviated *RA.* The second is the root mean square average formula, shown in Eq. 2.9 [42], and is abbreviated RMS. In the equations *L* is the total number of points and *Z* is the difference between the true *z* height at point *(x,y))* and the *z* height of the surface of best fit at point *(x,y)*. Approximately 19,101,609 pixels and thus data point are used in each estimation. The surface of best fit is calculated using a second order polynomial least square fitting function which is calculated in MatLAb.

$$Ra = (1/L)\int_0^L |Z(x)|dx \qquad (2.8)$$

$$RMS = \left[(1/L)\int_0^L Z(x)^2 dx\right]^{1/2} \qquad (2.9)$$

The MatLab code [43], shown in Appendix B-1, is used for the estimation of a second order polynomial surface fitting function of the surface height data in each image. The

second order polynomial function is defined by Eq. 2.10 where a_{pq} is the coefficients of the polynomial function that is defining the surface with p and q equal to 3 such that a second order function is formed. The x, y, and a_{pq} coefficients can then be placed in matrix form, as shown in Eq. 2.11. This means that the $f(x,y)$ is equal to the transpose of x matrix multiplied by the A matrix multiplied by the y matrix, as shown in Eq. 2.12. The least square equation ($s(a_{11},...,a_{pq})$) can then be expressed by Eq. 2.13 where ω_g is the weight function that is equal to 1. Let the partial derivative of s with respect to a ($\delta s/\delta a_{ij}$) equal to 0 with i varying from 0 to p and j varying from 0 to q. The least square equation can then be expressed by Eq. 2.14 given that the partial derivative of $f(x_g, y_g)$ with respect to a_{ij} equals $x_g^{i-1}y_g^{j-1}$. The variable z can then be expressed in terms of a, x, and y, as shown in Eq. 2.15, which can then be simplified to Eq. 2.16. If we let $u_{\alpha\beta}(i,j)$ equal Eq. 2.17 and $v(i,j)$ equal to Eq. 2.18 then this leads to the derivative of the least square function equal to Eq. 2.19. This expression then can be simplified into matrix form as shown by Eq. 2.20 such that the coefficient of the second order polynomial can then be calculated. With the calculated coefficients of the second-order polynomial equation the values of x and y can be substituted into the equation so that a calculated z-value or average height value is obtained. The calculation of RA and RMS is performed in Excel and from the results comparisons in surface roughness of the different materials and fracture energies can be obtained.

$$
\begin{aligned}
f(x,y) = \; & a_{11} && +a_{12}y && +a_{13}y^2 && +\cdots && +a_{1q}y^{q-1} \\
& +a_{21}x && +a_{22}xy && +a_{23}xy^2 && +\cdots && +a_{2q}xy^{q-1} \\
& \vdots \\
& +a_{i1}x^{i-1} && +a_{i2}x^{i-1}y && +a_{i3}x^{i-1}y^2 && +\cdots && +a_{iq}x^{i-1}y^{q-1} \\
& \vdots \\
& +a_{p1}x^{p-1} && +a_{p2}x^{p-1}y && +a_{p3}x^{p-1}y^2 && +\cdots && +a_{pq}x^{p-1}y^{q-1}
\end{aligned}
\tag{2.10}
$$

$$\mathbf{x}=\begin{bmatrix}1\\x\\x^2\\\vdots\\x^p\end{bmatrix},\mathbf{y}=\begin{bmatrix}1\\y\\y^2\\\vdots\\y^q\end{bmatrix},\mathbf{A}=\begin{bmatrix}a_{11}&a_{12}&\cdots&a_{1q}\\a_{21}&a_{22}&\cdots&a_{2q}\\\vdots&\vdots&\ddots&\vdots\\a_{p1}&a_{p2}&\cdots&a_{pq}\end{bmatrix} \tag{2.11}$$

$$f(\mathbf{x},\mathbf{y})=\mathbf{x}^T\mathbf{A}\mathbf{y} \tag{2.12}$$

$$s(a_{11},\cdots,a_{pq})=\sum_{g=1}^{n}\omega_g[f(x_g,y_g)-z_g]^2=\sum_{g=1}^{n}\omega_g(\sum_{i=1}^{p}\sum_{j=1}^{q}a_{ij}x^{i-1}y^{j-1}-z_g)^2 \tag{2.13}$$

$$\frac{\partial s}{\partial a_{ij}}=\frac{\partial}{\partial a_{ij}}\sum_{g=1}^{n}[f(x_g,y_g)-z_g]^2=2\sum_{g=1}^{n}\left[x_g^{i-1}y_g^{j-1}f(x_g,y_g)-x_g^{i-1}y_g^{j-1}z_g\right] \tag{2.14}$$

$$\sum_{g=1}^{n}x_g^{i-1}y_g^{j-1}\sum_{\alpha=1}^{p}\sum_{\beta=1}^{q}a_{\alpha\beta}x_g^{\alpha-1}y_g^{\beta-1}=\sum_{g=1}^{n}x_g^{i-1}y_g^{j-1}z_g \tag{2.15}$$

$$\sum_{\alpha\beta=1,1}^{p,q}\left[a_{\alpha\beta}\sum_{g=1}^{n}(x_g^{\alpha-1}y_g^{\beta-1}x_g^{i-1}y_g^{j-1})\right]=\sum_{g=1}^{n}x_g^{i-1}y_g^{j-1}z_g \tag{2.16}$$

$$u_{\alpha\beta}(i,j)=\sum_{g=1}^{n}(x_g^{\alpha-1}y_g^{\beta-1}x_g^{i-1}y_g^{j-1}) \tag{2.17}$$

$$v(i,j)=\sum_{g=1}^{n}x_g^{i-1}y_g^{j-1}z_g \tag{2.18}$$

$$\sum_{\alpha\beta=1,1}^{p,q}a_{\alpha\beta}u_{\alpha\beta}(i,j)=v(i,j) \tag{2.19}$$

$$\begin{bmatrix}u_{11}(1,1)&\cdots&u_{pq}(1,1)\\\vdots&\ddots&\vdots\\u_{11}(p,q)&\cdots&u_{pq}(p,q)\end{bmatrix}\begin{bmatrix}a_{11}\\\vdots\\a_{pq}\end{bmatrix}=\begin{bmatrix}v(1,1)\\\vdots\\v(p,q)\end{bmatrix} \tag{2.20}$$

2.5 Aluminum Diffusion Testing

2.5.1 Experiment 1: Testing Procedure

The first aluminum diffusion test is performed using the MTS Friction Stir Welding Machine, shown in Fig. 2.16. A rod of each of the materials is cut using the abrasive saw to 15” in length and is used as a cylindrical FSW tool without any special modifications. Essentially it is used as a tool pin that is rotated and plunge in the base material at a

prescribed *z*-force and rotational speed. The MP159 rod is turned down to ½" diameter so that it can secured fastened in the available ½" collet and the H13 rod stock is able to be secured with the ½" collet as well. The TSP1 rod had to have a special ordered 41/64" collet to avoid excessive machining time by turning down the approximately 5/8" rod to ½" diameter. Once the rod is secured in the FSW machine and the base plate is properly clamped down the plunging process can be performed. Each rod is rotated at 500 rpm with a plunge force or *z*-force of 3,000 lbf for thirty seconds such that a sufficient amount of aluminum is attached to the rod tip. Once one end of the rod is tipped with aluminum it is removed from the vice and the opposite end of the rod is then tipped with aluminum using the same procure. This is so that an initial specimen can be compared to a heat exposed specimen.

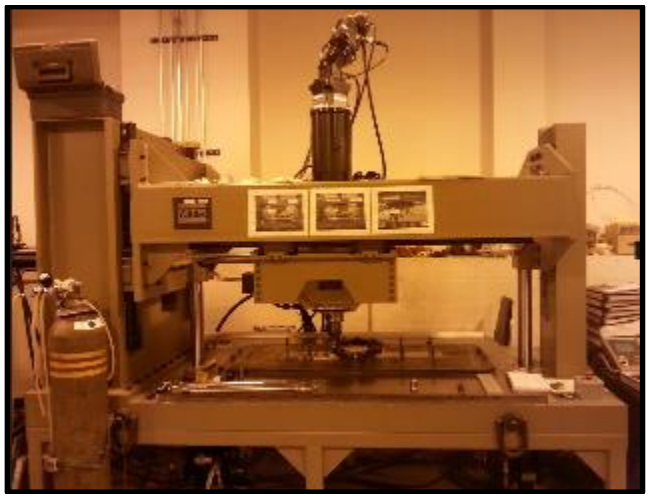

Fig. 2.16 MTS Friction Stir Welding Machine

2.5.2 EXPERIMENT 1: SPECIMEN PREPARATION

Once the rods were plunged into the aluminum using the FSW machine the tips of the rod were cut off using the abrasive cutter such that disks that are approximately ½" thick are created. For each material there is one disk that is going to stay at room temperature and the second disk is exposed to the welding temperature of 525 °C for 50 hours in the

salt bath. Diffusion is created by atomic motion that transport material from one medium to another. At elevated temperature atomic motion and vibration increases which enables atomic energy barriers to be broken and thus atomic mixing and material transport is created. For this reason the highest welding temperature and longest exposure duration is chosen.

Once the aluminum tip disks were exposed to the temperature they are cut into halves again using the abrasive cutter and one of the halves is placed in an epoxy mold to simplify the polishing procedure. The same procedure as shown in Section 2.2.1 for the mounting and Section 2.2.2 for polishing is performed on these specimens. To ensure the highest level and quality of polishing each of the specimens is also polished in the automatic polishing machine for 12 hours in colloidal silica. Once polishing is complete the specimens must be removed from the mold because the epoxy will create charging issues in the SEM machine. The removal is performed using a hand saw, a vice, and a small hammer. Extreme care is taken to ensure the surface is not damage or contaminated. Once the specimens are removed from the mount a flat is created on the back using the surface grinder so that the specimen can be securely and even mounted in the SEM. Post temperature simulated H13 (a), TSP1 (b), and MP159 (c) specimens are shown in Fig. 2.17.

Fig. 2.17 H13 (a), TSP1 (b), & MP159 (c) Al-Diffusion Specimens: Experiment 1

2.5.3 EXPERIMENT 2: SPECIMEN PREPARATION

To further analyze the effects of aluminum diffusion a second experiment is conducted using tool shoulders and pins that have previously been in operation. For the analysis of aluminum diffusion on H13 a tool shoulder with a failed MP159 pin is used, for TSP1 a failed tool pin is used, and for MP159 three tool pins are used that all have various levels of aluminum exposure and adhesion. MP159 is hypothesized to be the most volunerable to aluminum diffusion and for that reason three specimens are being observed. The H13 tool shoulder (a), the TSP1 failed pin (b), and the three MP159 tool pins (c) all with various levels of aluminum expsure are shown in Fig. 2.18.

Fig. 2.18 H13 (a), TSP1 (b), & MP159 (c) Aluminum Exposed Tools: Experiment 2

The tools are cut in half using the abbraive cutter such that a reasonable sized cross section can be analyzed. The goal is to see how much aluminum difffusion has already occured in the tool due to previous operation and compare an intial specimen to a specimen that has been exposed to a welding temperature in the salt bath. For this experiment a temperature of 525 °C is again used but this time the specimens are exposed to the temperature for 200 hours. The specimens again follows the same procedure as Section 2.2.1 for the mounting and Section 2.2.2 for the polishing with the added colloidal silica polishing. They are again removed from the mount and a flat is created on the unpolished

side parallel to the polished plane of the tool segment. The interface between the aluminum and the tool material is the area of interest for the analysis. The cross section of the completed specimens for the H13 tool shoulder (a), TSP1 tool pin (b), and three MP159 tool pins (c) is shown in Fig. 2.19.

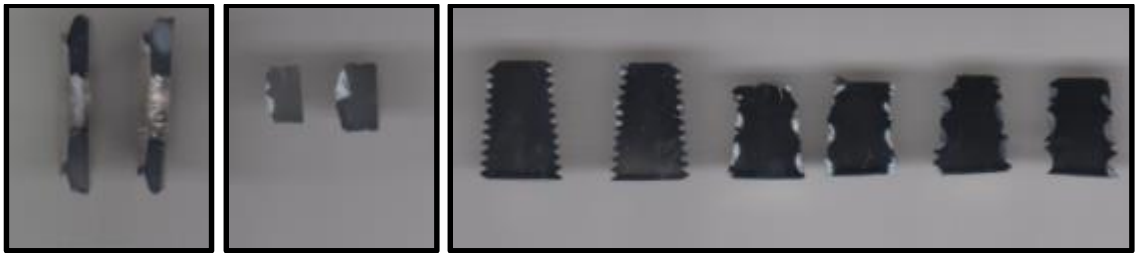

(a) (b) (c)

Fig. 2.19 H13 (a), TSP1 (b), & MP159 (c) Al-Diffusion Specimens: Experiment 2

2.5.4 Aluminum Diffusion Analysis

Once the specimens are prepared for the SEM the same set up procedure is used as shown in Section 2.4.4. Again the first detector used will be the SE2 detector at a working distance of about 8.5 mm. For experiment 1 the only interface between the tool material and aluminum alloy is observed. For experiment 2 the interface that appears to be visually most highly affected by aluminum diffusion is chosen. An SE2 image at a magnification of 1000x for experiment 1 and 250x for experiment 2 is used for compositional analysis using the EDAX software for EDS (Energy Dispersive X-ray Spectroscopy) analysis. With the image loaded in the EDAX software the compositional analysis of the entire image can be obtained with some degree of accuracy using the Expert ID option. However, some elements will need to be removed and occasionally some elements may need to be added depending on the known elements in that particular materials composition. With all elements accounted for the compositional analysis across a given line option is used to get an idea as to what happen to material composition at the interface between the tool material

and aluminum alloy. After the compositional line data is collected it is exported to Excel where results can be created and conclusions can be drawn.

A secondary method was also performed using an EsB (Energy selective Backscatter) Detector for BSE (Backscattered Electron) imaging. The EsB detector uses a filtering grid to repel secondary electrons that pass through the aperture so that BSE images with variable electron energy contributions can be created. With this detector narrow bands of energy can be displayed so that surface information, voltage contrast, and material contrast differences can be observed [49]. The proper working distance for the EsB detector is 3mm but it can be difficult to focus the BSE image and for this reason the focusing is done using the SE2 detector. The SEM can be switched to the EsB detector for BSE imaging once the image is focus at a working distance of 3mm and at a magnification of 1000x with the SE2 detector. The BSE image can also be very noisy and require a high value of contrast. A scanning speed of 10 provided low noise and high quality images. The EsB detector shows particles with heavy density to be a light color and particles with a lighter density are a darker color. Evidence of aluminum diffusion can be seen when a region around the interface appears to gradually transform from light to dark. If there is a presence of a color gradient this means that there is a mixed composition of aluminum and tool material particles created by aluminum diffusion.

CHAPTER 3

RESULTS & DISCUSSION

The following is experimental results and discussion of the metallographic imaging, hardness testing, Izod impact energy testing, Izod fracture surface SEM analysis, Izod fracture surface roughness calculation, and aluminum diffusion test 1 and test 2 of the H13, MP159, and TSP1 tool materials.

3.1 METALLOGRAPHIC IMAGING

3.1.1 H13 METALLOGRAPHIC IMAGES

After the 2% Nital immersion followed by the Viella's Reagent immersion the microstructure of H13 was visible using the VHX-5000 digital microscope. The most valuable metallographic images were taken at 500x, 1000x, 2000x, and 3000x, shown in Fig. 3.1 and Fig 3.2. In the 500x and 1000x images larger precipitates can be seen in the microstructure but at 2000x and 3000x magnification smaller blue precipitates can be seen that appear less than a micron in diameter. These precipitates are believed to be chromium carbides that help strengthen the material matrix. The grain boundaries in the material were not observable after etching with the 2% Nital and Veilla's Reagent etch but the etch is capable of revealing the carbides which gives valuable information about H13's strengthening mechanism.

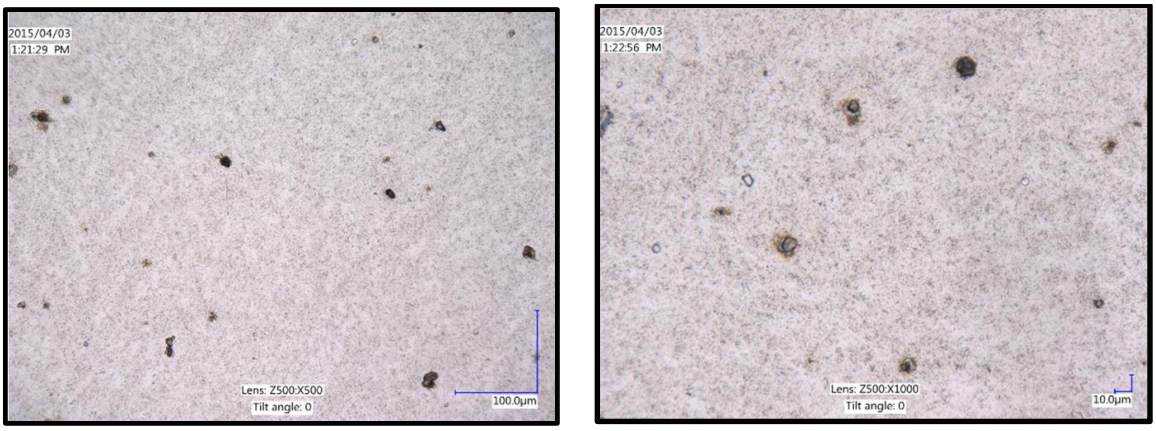

(a) (b)

Fig. 3.1 H13 Metallographic Images at 500x (a) and 1000x (b) Magnifications

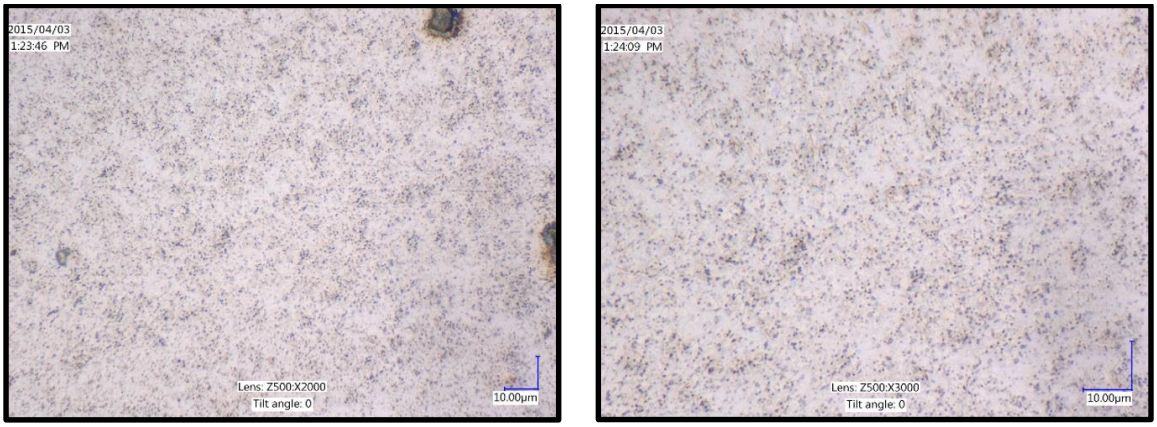

(a) (b)

Fig. 3.2 H13 Metallographic Images at 2000x (a) and 3000x (b) Magnifications

3.1.2 MP159 METALLOGRAPHIC IMAGES

After the Special #5 immersion the microstructure of MP159 was visible using the VHX-5000 digital microscope. The most valuable metallographic images were taken at 500x and 1000x magnifications. A central location of the specimen is shown in Fig. 3.3 and an edge boundary is shown in Fig 3.4. Both sets of images show grain boundaries of the MP159 material along with evidence of twinning. A larger average grain size could be observed on the edge of the rod, approximately 55 µm, in comparison to the central location with an average grain size of approximately 35 µm. Large gold colored particles are noticed

throughout the material matrix along with some small blue precipitates but unlike H13 it is unlikely that these are carbides due to the lack of carbon present in the MP159 material. The darker regions in the microstructure are evidence of the martensite present in the material matrix. The combination of the martensite with the participation hardening highly contribute to MP159's excellent tool material properties.

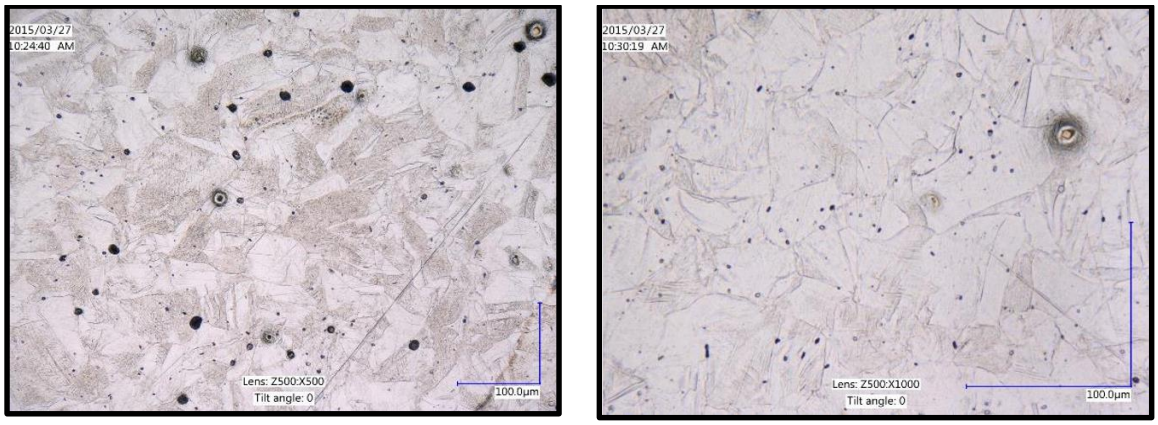

(a) (b)

Fig. 3.3 MP159 Central Metallographic Images at 500x (a) and 1000x (b) Magnifications

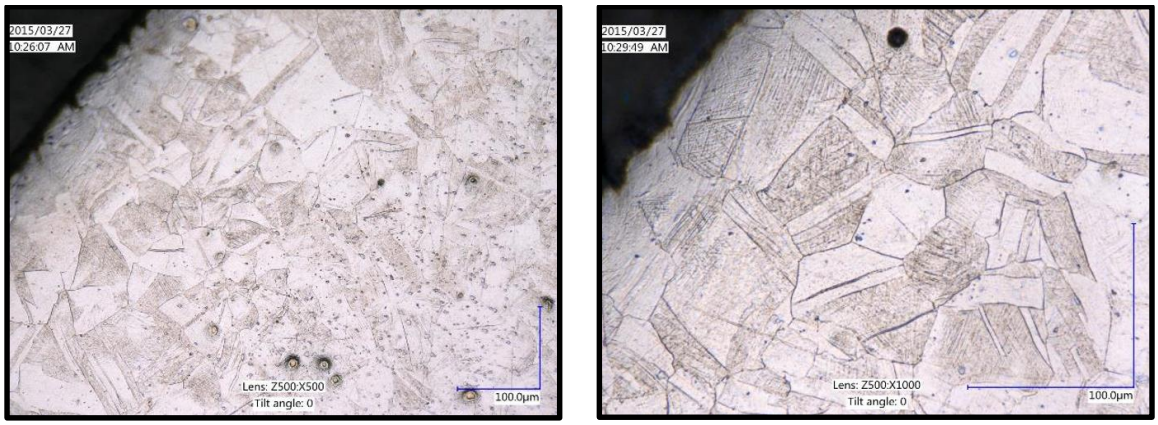

(a) (b)

Fig. 3.4 MP159 Edge Metallographic Images at 500x (a) and 1000x (b) Magnifications

3.1.3 TSP1

After the 2% Nital immersion followed by the Viella's Reagent immersion the microstructure of TSP1 was visible using the VHX-5000 digital microscope. The most

valuable metallographic images were taken at 500x, 1000x , 2000x, and 3000x, shown in Fig. 3.5 and Fig 3.6. In the 500x and 1000x images larger precipitates can be seen in the microstructure similar to H13. Also at 2000x and 3000x magnification very similar smaller blue precipitates can be seen that appear less than a micron in diameter. The main difference observed in the microstructure of TSP1 is a finer dispersion of carbide precipitates in comparison to H13. The grain boundaries in the material were able to be obtained by the 2% Nital and Veilla's Reagent etch but they could not be observed in detail until the 2000x and 3000x magnification was used.

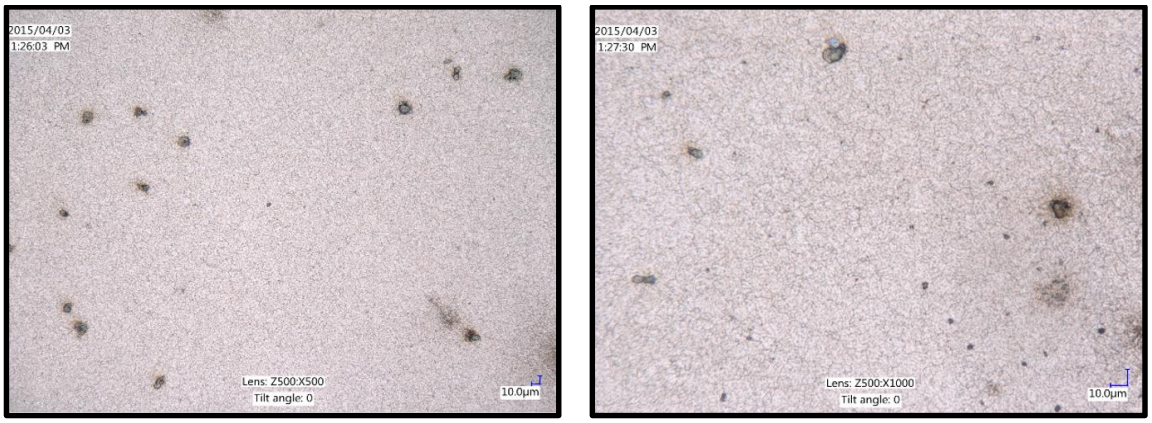

(a) (b)

Fig. 3.5 TSP1 Metallographic Images at 500x (a) and 1000x (b) Magnifications

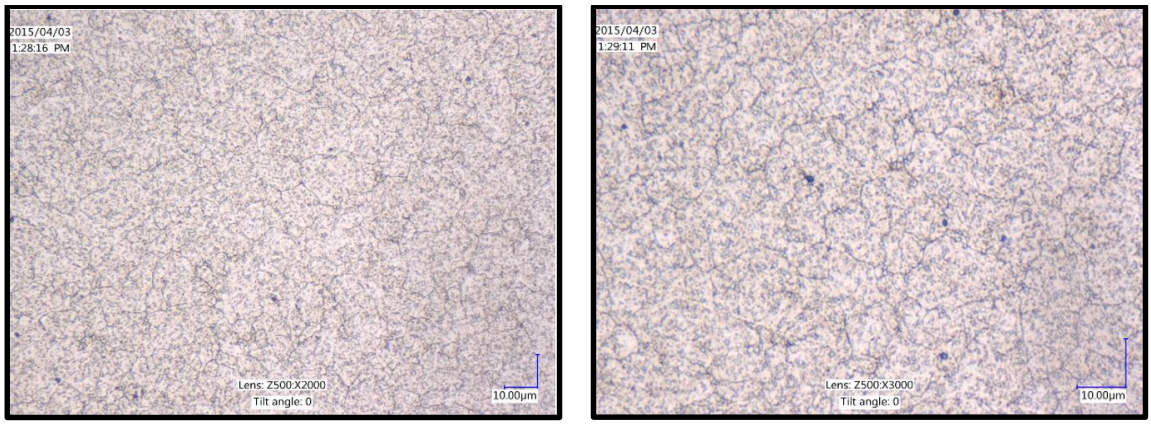

(a) (b)

Fig. 3.6 TSP1 Metallographic Images at 2000x (a) and 3000x (b) Magnifications

The TSP1 grain size is approximately 8 μm which is much smaller that the grain size observed in the MP159 material. TSP1 appears to have a very similar microstructure in comparison to H13 due to the similar material compositions of the ferritic tool steel but there appears to be a higher quantity and finer dispersion of particles in the TSP1. The small grain size and higher quantity with finer dispersion of carbide particles is the reason that the TSP1 material is the hardest of the tool material.

3.2 Hardness Testing

3.2.1 H13 Hardness Testing

For the H13 hardness testing 13 indentations were made in a straight line across the diameter of the rod in 0.025" increments near the edge of the rod and the center but 0.05" increments at all points in between. The initial heat treated H13 rod showed evidence of large decrease in hardness at points approaching the quenched surface, shown in Fig. 3.7 (a). This may be due to decarburization created when the rods are austenitized at 980 °C for twenty minutes in an air atmosphere. At high temperatures carbon atoms on the tool materials surface are susceptible to interact with the furnace atmosphere and are removed as a gas from the steel by bonding with oxygen molecules in the air [44]. At points between 0 and 5.7 mm the hardness varied between 525 HV to 541 HV however, at the furthest point measurable the hardness was measured as low as 367 HV. Once the metal is exposed to the welding exposure conditions the effect of the decarburization decreased and hardness fluctuation are minimized as temperature and time exposure increase. The reason for this hardness recovery is unknown. At low temperatures and time hardness fluctuations and edge hardness are observed, shown in Fig. 3.7 (b) & (c). At high temperatures and times little hardness variation and edge hardness decrease is observed, shown in Fig. 3.7 (d).

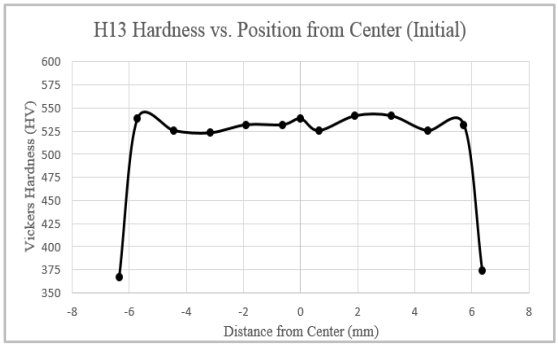

(a)

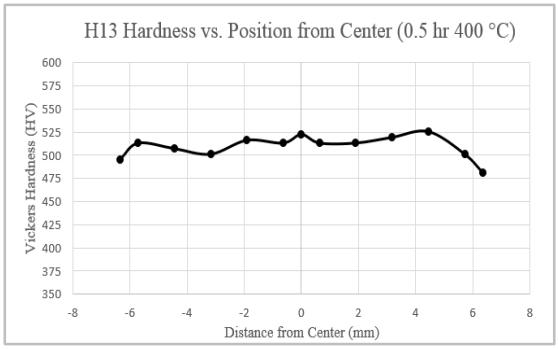

(b)

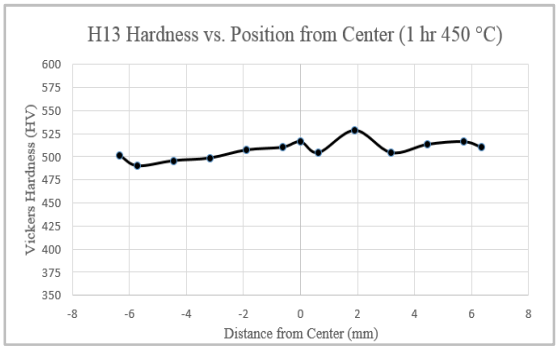

(c)

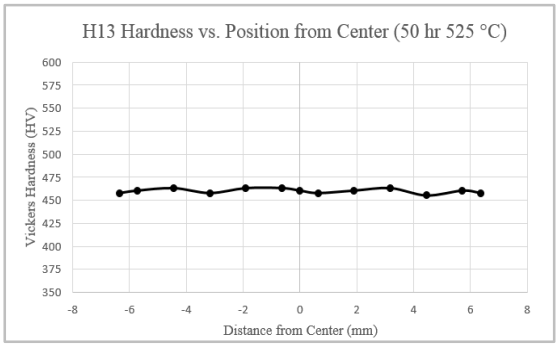

(d)

Fig. 3.7 H13 HV vs Position from Rod Center at Various Temperatures & Times

Average values of the hardness are used, while neglecting low edge hardness values, to determine how the hardness of H13 changes at specific temperatures as the welding time increases from 0.5 hour to 50 hours. Also at every temperature and time there was a range of hardness values measured and the range at each temperature and time is shown by the error bars at each point in Fig. 3.8. For the first hour of temperature exposure at 400 °C the hardness drops sharply from 532 HV to 504 HV. Then at 5 hours the initial hardness is restored and from 5 hours to 50 hours gradual increase in hardness is observed up to 550 HV, as shown in Fig. 3.8 (a). The 450 °C exposure showed a similar initial drop in hardness for the first hour and then hardness is restored up to 525 HV where the hardness then does not vary significantly up to 50 hours, as shown in Fig. 3.8 (b). The 500 °C exposure showed the same initial drop in hardness for the first hour and then hardness is restored up to 512 HV where the hardness then linearly decreases to 480 HV at 50 hours, as shown in Fig. 3.8

(c). The 525°C exposure showed the largest initial drop in hardness, from 532 HV to 488 HV, followed by a small spike in hardness to 496 HV. After first increase is observed the value of the hardness decreases to 486 HV at 5 hours and then declines relatively linearly down to 460 HV at 50 hours, as shown in Fig. 3.8 (d).

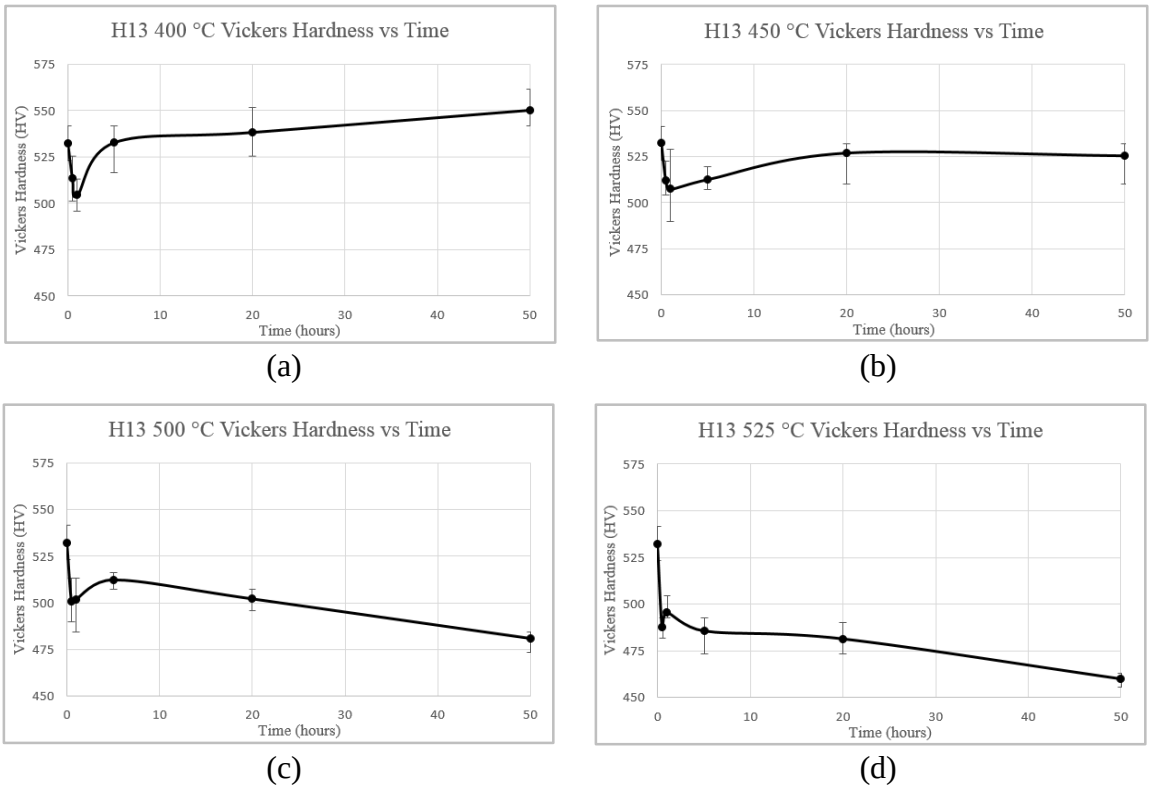

Fig. 3.8 H13 400°C (a), 450°C (b), 500°C (c), 525°C (d) Vickers Hardness vs Time

An overlay of all of the H13 hardness vs. times at specific temperatures is shown in Fig. 3.9. The 400 °C specimens ended up hardening in the range of times used while all other temperatures resulted in a lower hardness value at the end of the 50 hours in comparison to the initial hardness obtained. The difference in the maximum and minimum hardness for the H13 was 550 HV at 50 hours simulated at 400 °C and 460 HV at 50 hours simulated at 525 °C. In Rockwell C that is a range of 46 HRC to 52 HRC and thus a lower than desired tool hardness can be obtained during the welding process. All temperatures showed an initial drop in temperature from the initial hardness of 532 HV to range of

hardness from 507 HV to 486 HV with the larger differences being seen at higher temperatures. After the drop an initial increase is observed in all specimens but the duration of the hardness increases drastically decreases with temperature. At 400 °C the hardness steadily increases, at 450 °C the hardness essentially levels out, and at 500°C & 525°C the hardness steadily decreases with time after the initial spike in hardness.

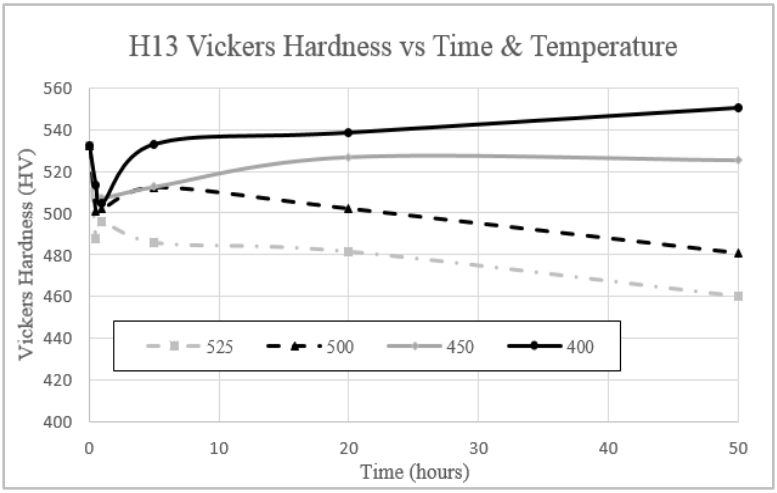

Fig. 3.9 H13 Vickers Hardness vs Time & Temperature

3.2.2 MP159 HARDNESS TESTING

For the MP159 hardness testing 13 indentations were made in a straight line across the diameter of the rod in 0.025” increments near the edge of the rod and the center but 0.05” increments at all points in between. In all scenarios at points approaching the center the rod the hardness of MP159 significantly decreases, as shown in Fig. 3.10, with a maximum deviation of 496 HV to 610 HV (49 HRC to 56 HRC) at 50 hours and 525°C. This could be due to the cold drawing of the rod where a higher level of cold working is experienced by the rod at the surface in comparison to the center of the rod. Higher level of cold working will result in higher hardness. Also, as shown in Fig. 3.10, at lower temperatures and times there is a higher level of hardness oscillation experienced in the rod but at high temperatures and times a smoother relationship is observed.

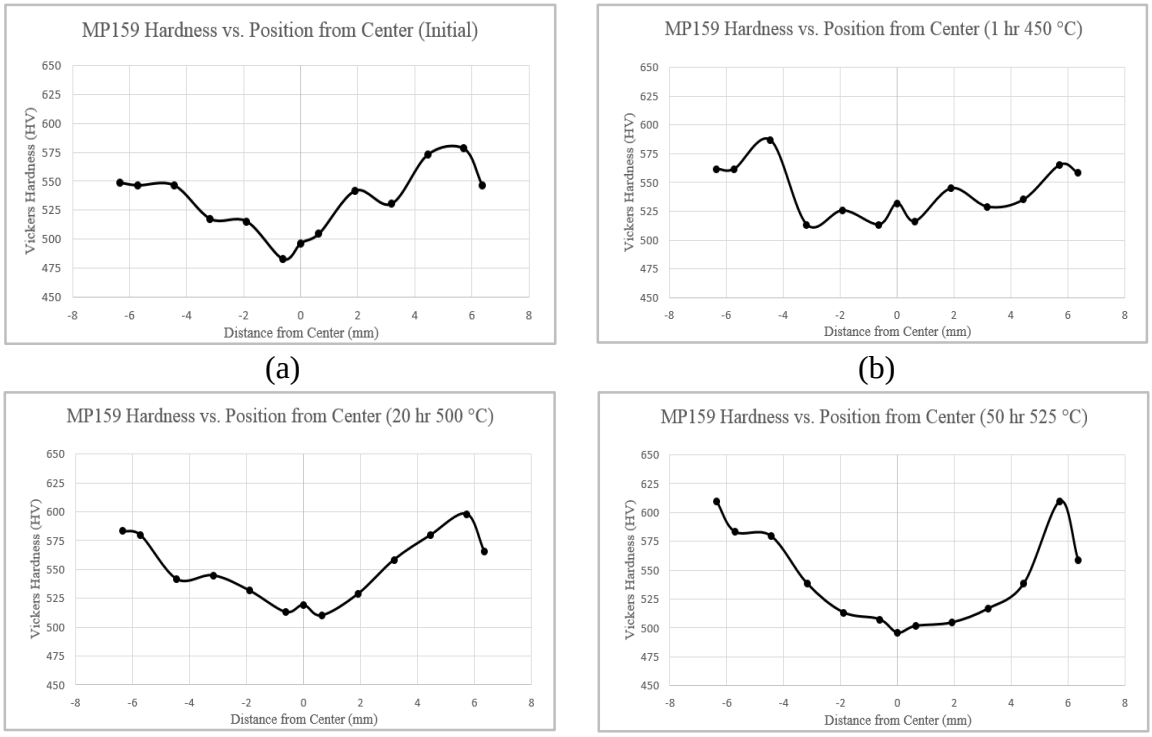

Fig. 3.10 MP159 HV vs Position from Rod Center at Various Temperatures & Times

Average values of the hardness are used to determine how the hardness of MP159 changes at specific temperatures as the welding time increases from 0.5 hour to 50 hours. Also at every temperature and time there was a range of hardness values measured and the range at each temperature and time is shown by the error bars at each point in Fig. 3.11. For the first hour of temperature exposure at 400 °C the hardness increases slightly from 533 HV to 540 HV. Then the hardness steadily decreased from 5 hours to 50 hours to a hardness of 526 HV, as shown in Fig. 3.11 (a). The 450 °C exposure showed a similar initial increase in hardness for the first half hour up to 547 HV and then hardness decreased to 542 HV where the hardness then does not vary significantly up to 50 hours, as shown in Fig. 3.11 (b). The 500 °C exposure showed the same initial increase in hardness for the first hour up to a hardness of 543 HV and then the hardness stays constant up to 5 hours. After five hours the hardness increases to 550 HV at 20 hours where it then stays constant

up to 50 hours, as shown in Fig. 3.11 (c). The 525°C exposure showed an increase in hardness, from 533 HV to 543HV, between the initial and half our specimens followed by a small drop to 541 HV at 1 hour. The hardness then increase to 549 HV at 20 hours where it then decreases to 543 HV at 50 hours, as shown in Fig. 3.11 (d).

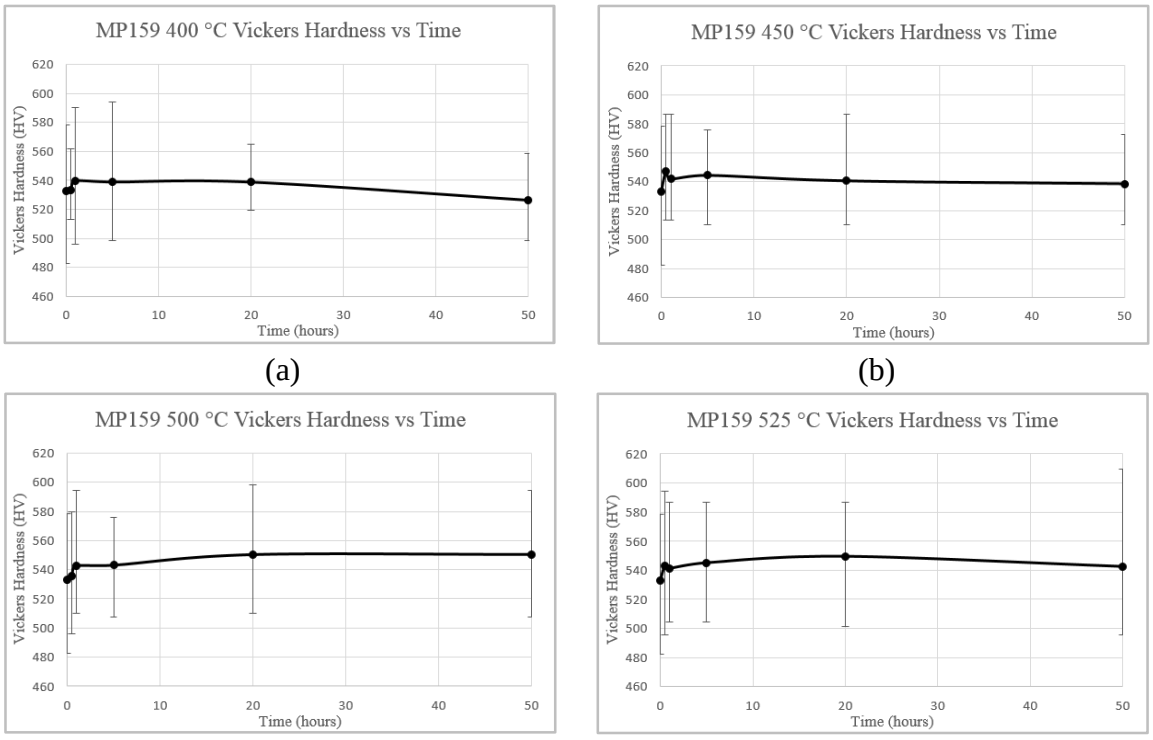

(a) (b)

(c) (d)

Fig. 3.11 MP159 400°C (a), 450°C (b), 500°C (c), 525°C (d) Vickers Hardness vs Time

An overlay of all of the MP159 hardness vs. times at specific welding temperatures is shown in Fig. 3.12. All temperatures showed a small increase in hardness from the initial hardness is observed where after the initial hardness increase the 400°C specimens decreases up to 50 hours, the 450°C specimens appear to stay at a constant hardness up to 50 hours, the 500°C specimens appear to increase in hardness up to 50 hours, and the 525°C specimens appear to increase in hardness up to 20 hours but then decrease in hardness up to 50 hours. The difference in the maximum and minimum hardness for the MP159 was 550 HV at 50 hours simulated at 500 °C and 526 HV at 50 hours simulated at 400 °C. In

Rockwell C that is a range of 50.8 HRC to 52.3 HRC and thus the average tool hardness will be near the desired hardness throughout all of the welding temperature and times. However, as previously mentioned there are very large deviation in hardness across the diameter of the rod with the lowest hardness observed in the center and highest hardness observed furthest away from the center. This is critical to tool design with MP159 rod because if the tool is machined to a specific geometry then the hardness at surface areas closer to the center of the tool will have lower hardness values than areas furthest away from the center and thus higher tool material degradation may be observed in area of the tool that have lower hardness.

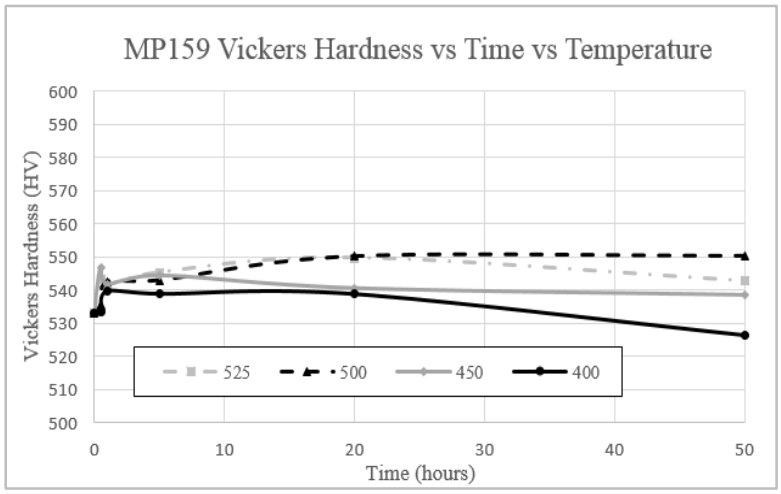

Fig. 3.12 MP159 Vickers Hardness vs Time & Temperature

3.2.3 TSP1 HARDNESS TESTING

For the TSP1 hardness testing 15 indentations were made in a straight line across the diameter of the rod in 0.025” increments near the edge of the rod and the center but 0.05” increments at all points in between. The initial heat treated TSP1 rod showed evidence of a slight decrease in hardness at the point closest rod surface, shown in Fig. 3.13 (a). This may also be due to decarburization when the rods were heat treated although, an inert gas furnace was used. In the initial specimen there appears to be a lot of fluctuation and

deviation in the hardness ranging from 677 HV to 768 HV. This fluctuation and deviation appear to quickly diminish with temperature and time, as seen in Fig. 3.13 (b), where the hardness at ½ hour and 400 °C only varies between 725 HV and 757 HV. This trend can continue to be seen in Fig. 3.13 (c) where at 20 hours and 500 °C the hardness varies between 757 HV and 779 HV and in Fig. 3.13 (d) where at 50 hours and 525 °C the hardness only varies between 730 HV and 715 HV with very small fluctuation in the values.

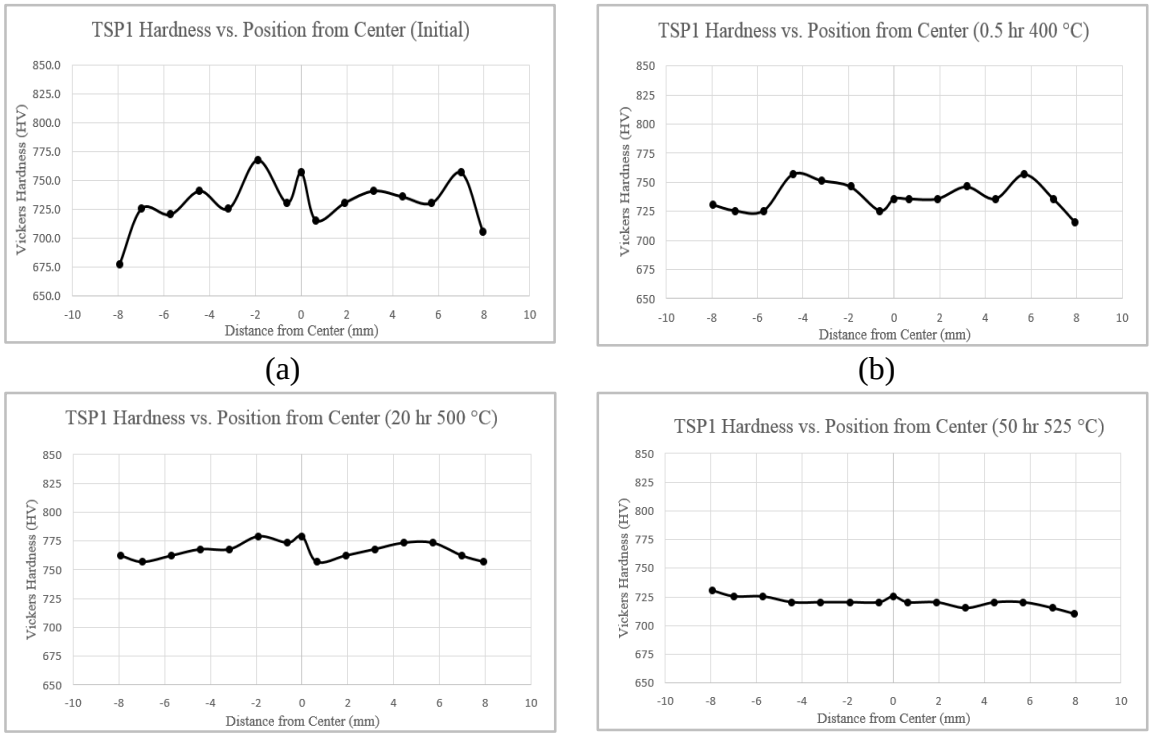

Fig. 3.13 TSP1 HV vs Position from Rod Center at Various Temperatures & Times

Average values of the hardness are used to determine how the hardness of TSP1 changes at specific temperatures as the welding time increases from 0.5 hour to 50 hours. Also at every temperature and time there was a range of hardness values measured and the range at each temperature and time is shown by the error bars at each point in Fig. 3.14. For the five hours of temperature exposure at 400 °C the hardness increases from 730 HV to 813 HV. Then at 20 hours the hardness drops to 787 HV followed by a slight decrease

in hardness from 20 hours to 50 hours to 578 HV, as shown in Fig. 3.14 (a). The 450 °C exposure showed a similar initial increase in hardness for the first hour to 794 HV and then hardness is decreased to 778 HV at 5 hours. After 5 hours there is a slight increase in hardness to 791 HV at 20 hours followed by a gradual decrease in hardness to 773 HV at 50 hours, as shown in Fig. 3.14 (b). The 500 °C exposure showed the same initial increase in hardness for the first hour to 794 HV and then the hardness is again decreased to a value of 773 HV. The hardness then linearly decreases to a value of 747 HV at 50 hours, as shown in Fig. 3.14 (c). The 525 °C exposure showed again the initial sharp increase in hardness, from 731 HV to 797 HV, followed by a parabolic decrease in hardness from 1 hour to 20 hours resulting in a hardness of 704 HV. After the decrease in hardness there is then an increase in hardness to 721 HV at 50 hours, as shown in Fig. 3.14 (d).

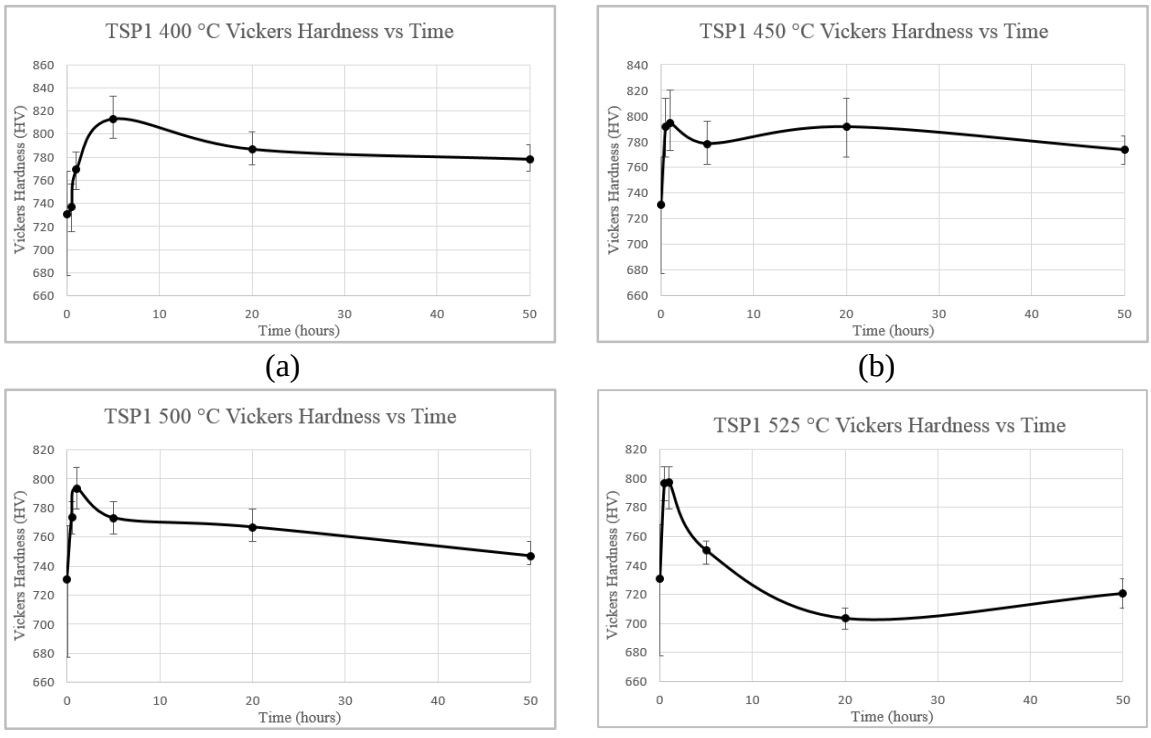

Fig. 3.14 TSP1 400°C (a), 450°C (b), 500°C (c), 525°C (d) Vickers Hardness vs Time

An overlay of all of the TSP1 hardness vs. times at specific welding temperatures is shown in Fig. 3.15. All temperatures showed a large increase in hardness from the initial hardness with the greatest increase being shown in 400 °C specimen where the hardness increases from 731 HV 813 HV, or 60 HRC to 63 HRC, in the first 5 hours. After the increase every temperature then experiences a decrease in hardness with the greatest decrease seen in the 525°C specimens where a hardness drop of 797 HV to 704 HV, or 62.5 HRC to 58.7 HRC, is seen between 1 hour and 20 hours. All temperature, with the exception of 525°C specimens, experience a hardness increase at the end of the 50 hours in comparison to the initial hardness obtained. At the end of the 50 hours the relationship between hardness and temperature is one such that as temperature increases, at long time periods, the hardness will decrease.

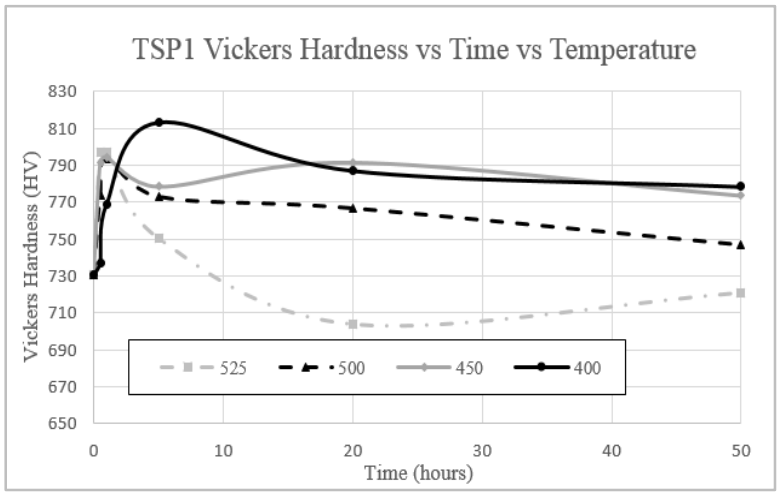

Fig. 3.15 TSP1 Vickers Hardness vs Time & Temperature

3.3 Izod Impact Energy Testing

3.3.1 H13

For the Izod testing the impact energy normalized about the area of specimens exposed to critical welding temperatures and times is analyzed. The critical temperatures and times used is based around the hardness results obtained in which for H13 an initial specimen, a

400 °C for 1 hour specimen, a 400 °C for 50 hour specimen, a 525 °C for a 1/2 hour specimen, and a 525 °C for 50 hours specimen is analyzed. The reason these values are chosen is because the highest hardness values are seen at 400 °C and the lowest hardness values are seen at 525 °C. At each of these temperatures the local minimum and local maximum hardness is chosen for Izod testing. At each temperature and time 5 specimens are used such that a statistical average can be obtained to determine how much nominal energy it takes for the H13 specimens to fracture and completely fail. The nominal impact energy for each trial along with the average, median, and standard deviation can be seen in Table 3.1.

Table 3.1 H13 Nominal Impact Energy Trials, Avg., Median, & Std. Deviation

H13 Nominal Impact Energy Testing (J/m^2)								
Trial #	**1**	**2**	**3**	**4**	**5**	**Average**	**Median**	**Std. Dev.**
Initial	230,262	241,576	228,511	275,622	352,445	265,683	241,576	52,067
1 hr 400° C	263,013	319,649	343,631	287,344	275,151	297,757	287,344	33,205
50 hr 400° C	161,468	195,409	185,169	205,685	206,881	190,922	195,409	18,664
0.5 hr 525° C	138,629	126,215	91,871	114,551	148,159	123,885	126,215	21,932
50 hr 525° C	331,926	400,600	377,367	366,276	385,562	372,346	377,367	25,830

The initial H13 specimens resulted in an average nominal impact energy value of 265,683 J/m^2. At 400 °C the hardness initially drops at times up to 1 hour where the hardness then increases at times up to 50 hours. The inverse relationship is observed with the nominal impact energy values that are obtained. When the hardness drops at 1 hour the nominal impact energy increases to 297,757 J/m^2 but when the hardness increases at 50 hours the nominal impact energy drops significantly to 190,922 J/m^2. At 525 °C the hardness initially drops at times at a 1/2 hour where the hardness then increases at 1 hour but then continues to decrease at times up to 50 hours. A direct relationship cannot be obtained when comparing nominal impact energy values to hardness. When the hardness drops at 1/2 hour the nominal impact energy decreases to 123,885 J/m^2 and when the hardness again decreases at 50 hours the nominal impact energy increases to 372,346 J/m^2.

A graph with the time vs hardness and nominal impact energy can be seen in Fig. 3.16 for 400 °C and Fig. 3.17 for 525 °C.

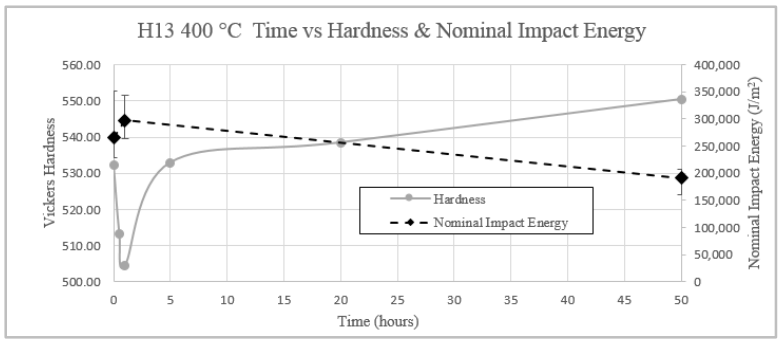

Fig. 3.16 H13 400 °C Time vs Hardness & Nominal Impact Energy

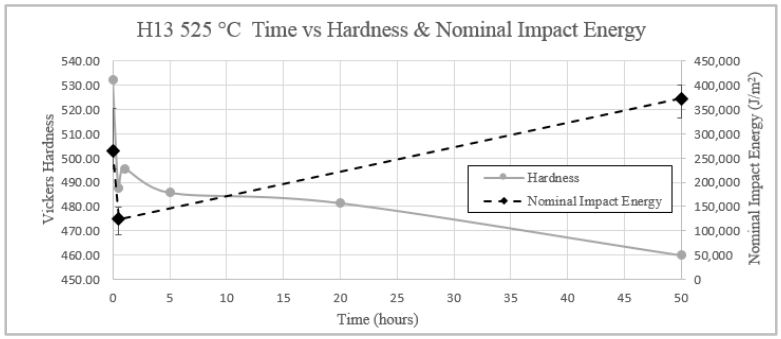

Fig. 3.17 H13 525 °C Time vs Hardness & Nominal Impact Energy

3.3.2 MP159

The critical temperatures and times used for the MP159 specimens is based around the hardness results obtained however, unlike H13 and TSP1 there was little variation in the average hardness of MP159 for all exposure conditions. For this reason an initial specimen and the 400 °C, 450 °C, 500 °C, and 525 °C for 50 hours specimens are used for the Izod impact energy testing. The reason these values are chosen is the maximum and minimum hardness values at all temperatures and times does no vary more than 24 HV. Since a definite hardness relationship cannot be obtained the critical scenarios are assumed to occur at the longest welding temperature and time exposure. At each temperature and time 5 specimens are used such that a statistical average can be obtained to determine how much

energy it takes for the MP159 specimens to fracture and completely fail. The nominal impact energy values for each trial along with the average, median, and standard deviation can be seen in Table 3.2.

Table 3.2 MP159 Nominal Impact Energy Trials, Avg., Median, and Std. Deviation

MP159 Nominal Impact Energy Testing (J/m^2)								
Trial #	**1**	**2**	**3**	**4**	**5**	**Average**	**Median**	**Std. Dev.**
Initial	384,157	395,526	337,665	488,555	464,579	414,096	395,526	61,594
50 hr 400° C	313,010	336,009	303,964	326,237	261,432	308,130	313,010	28,840
50 hr 450° C	294,146	288,823	289,283	326,513	312,284	302,210	294,146	16,609
50 hr 500° C	265,776	230,523	263,001	303,989	327,625	278,183	265,776	37,968
50 hr 525° C	293,133	445,880	330,797	449,996	370,090	377,979	370,090	69,434

The initial MP159 specimens resulted in an average nominal impact energy of 414,096 J/m^2 is obtained. At 400 °C the hardness decreases by 6 HV but at 450 °C, 500 °C, and 525 °C the hardness increases by 6 HV, 18 HV, and 10 HV respectively in comparison to the initial hardness of 532 HV. For all simulated temperatures the nominal impact energy decreases from the initial value. This means that the nominal impact energy value has an inverse response to hardness with the exception of the 400 °C exposure where the nominal impact energy reduces to 308,130 J/m^2. At 450 °C the hardness increase is the smallest and the nominal impact energy drop to 302,210 J/m^2. The next highest hardness increase was at 525 °C where the smallest decrease in nominal impact energy is observed resulting in a value of 377,979 J/m^2. The largest increase in hardness is seen at 500 °C where the largest drop in nominal impact energy is observed resulting in a value of 278,183 J/m^2. A graph with the time vs hardness and nominal impact energy values can be seen in Fig. 3.18 for 400 °C, 450 °C, 500 °C, and 525 °C exposure temperatures.

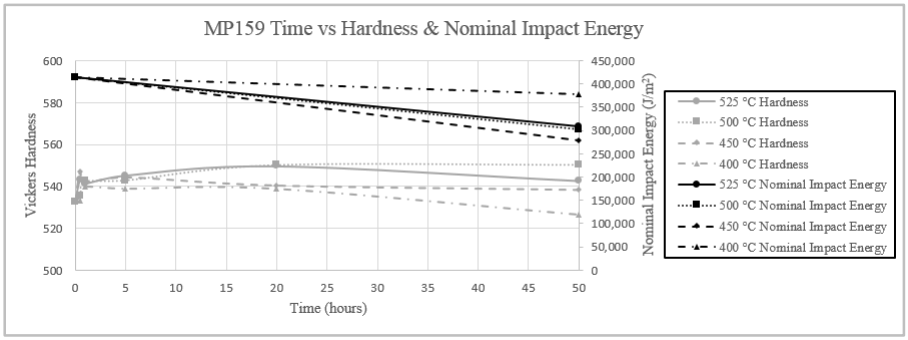

Fig. 3.18 MP159 Time vs Hardness & Nominal Impact Energy

3.3.3 TSP1

The critical temperatures and times used is based around the hardness results obtained in which for TSP1 an initial specimen, a 400 °C for 5 hour specimen, a 400 °C for 50 hour specimen, a 525 °C for a 1 hour specimen, and a 525 °C for 20 hours specimen is analyzed. The reason these values are chosen is because like H13 the highest hardness values are seen at 400 °C and the lowest hardness values are seen at 525 °C. At each of these temperature the local minimum and local maximum hardness is chosen for Izod testing. At each temperature and time 3 specimens are used such that a statistical average can be obtained to determine how much energy it takes for the TSP1 specimens to fracture and completely fail. The nominal impact energy values for each trial along with the average, median, and standard deviation can be seen in Table 3.3.

Table 3.3 TSP1 Nominal Impact Energy Trials, Avg., Median, and Std. Deviation

TSP1 Nominal Impact Energy Testing (J/m²)						
Trial #	**1**	**2**	**3**	**Average**	**Median**	**Std. Dev.**
Initial	51,809	44,348	52,058	49,405	51,809	4,381
5 hr 400° C	37,950	45,758	45,601	43,103	45,601	4,463
50 hr 400° C	37,106	29,526	29,706	32,113	29,706	4,326
1 hr 525° C	37,715	30,359	30,192	32,756	30,359	4,296
20 hr 525° C	22,675	22,553	22,507	22,578	22,553	87

The initial TSP1 specimens resulted in an average nominal impact energy value of 49,405 J/m^2. At 400 °C the hardness initially increases at times up to 5 hour where the hardness then decreases at times up to 50 hours. No direct relationship is observed in the

nominal impact energy values in comparison to the hardness. When the hardness increases at times up to 5 hours the nominal impact energy decreases to 43,103 J/m^2 but when the hardness decreases at times up to 50 hours the nominal impact energy instead continues to drop to 32,113 J/m^2. At 525 °C the hardness initially increases as well at times up to 1 hour where the hardness then decrease at 20 hours but then increases at times up to 50 hours. This means that the 20 hour exposure time is used due to the local minimum obtained at this point. The 525 °C testing showed the same trend as the 400 °C exposure where a trend is not observed with hardness but instead the nominal impact energy appears to simply decrease with time. When the hardness increases at 5 hours the nominal impact energy decreases to 32,756 J/m^2 and when the hardness again decreases at 20 hours the nominal impact energy decreases to 22,578 J/m^2. A graph with the time vs hardness and nominal impact energy can be seen in Fig. 3.19 for 400 °C and Fig. 3.20 for 525 °C.

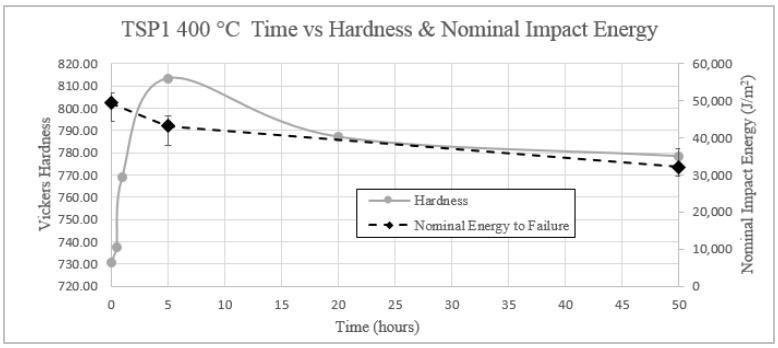

Fig. 3.19 TSP1 400 °C Time vs Hardness & Nominal Impact Energy

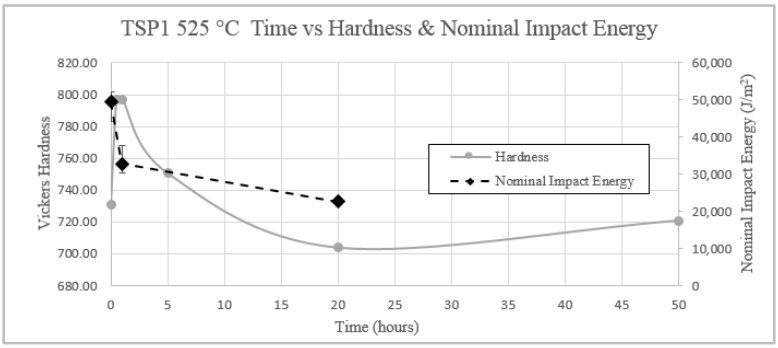

Fig. 3.20 TSP1 525 °C Time vs Hardness & Nominal Impact Energy

3.3.4 H13, TSP1, and MP159 Comparison of Hardness vs Nominal Impact Energy

The hardness values obtained are plotted against the nominal impact energy values at that specific hardness in order to find a general relationship based off of the data for all three tool materials. These values are plotted independent of the specific welding temperature and time exposure condition that corresponds to each of the hardness and nominal impact energy values. The graph of H13, TSP1, and MP159 hardness vs. nominal impact energy can be seen in Fig. 3.21. By plotting a linear line of best fit between all of the hardness vs nominal impact energy data point an inverse relationship is observed such that as the hardness increase in the tool materials the nominal impact energy will decrease.

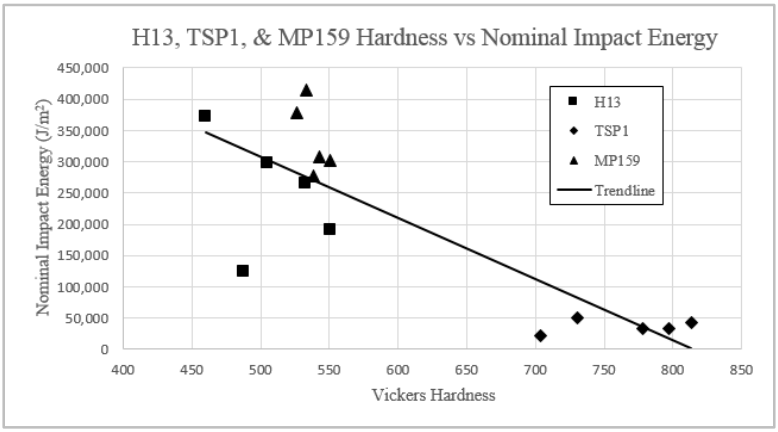

Fig. 3.21 H13, TSP1, and MP159 Hardness vs Nominal Impact Energy

3.4 Izod Fracture Surface SEM Analysis

3.4.1 H13 Izod Fracture Surface SEM Analysis

The nominal impact energy values for the H13 Izod testing specimens, shown prior to fracture in Fig. 3.22 (a), ranged from 123 kJ/m^2 to 372 kJ/m^2. The high nominal impact energy, low nominal impact energy,, and the initial room temperature specimen is used for analysis of the fracture surface since the initial specimens obtained a nominal impact energy to fracture value of 266 kJ/m^2. The Izod impact testing concluded that the 50 hour 525 °C specimens had the highest nominal impact energy while the lowest nominal impact

energy was seen in the ½ hour 500 °C specimens. All specimens failed in a similar manner where a large shear lip was formed upon fracture where approximately a 45 degree slope is gradually formed behind the notch on the lower surface of the specimen, as shown in Fig. 3.22 (b). All of the 3D fracture surface images are created using the VHX-5000 Digital Microscope live-depth up application.

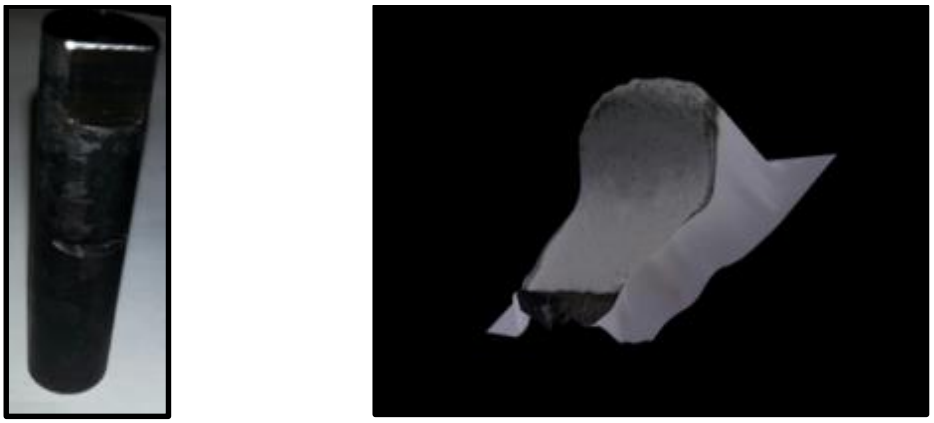

(a) (b)

Fig. 3.22 H13 Izod Specimen (a) and 3D Representation of Fracture Surface (b)

For every scenario the specimens failed by a microvoid coalescence process. This is evidence of uniaxial tensile overload being the principle cause of fracture and is a ductile failure mechanism [45]. This is also known as dimple rupture where dimples in the surface are nucleated around second-phase particles, grain boundaries, inclusions, and dislocation pile-ups. Images are taken in the Zeiss Ultra plus FE-SEM at 100x, 1000x, 5000x, 10,000x, 25,000x, and 50,000x magnifications and all of these images for the initial, high energy, and low energy specimens can be seen in in Appendix C Fig. C-1, Fig. C-2, and Fig. C-3, respectively. The evidence of microvoid coalescence can be clearly seen in the initial H13 specimens at the 5,000x magnification, shown in Fig. 3.23 (a), and 25,000x magnification, shown in Fig. 3.23 (b). Very little variation can be seen when comparing the initial

specimen images to the high impact energy specimens, shown in Fig. 3.24, and the low impact energy specimens, shown in Fig. 3.25.

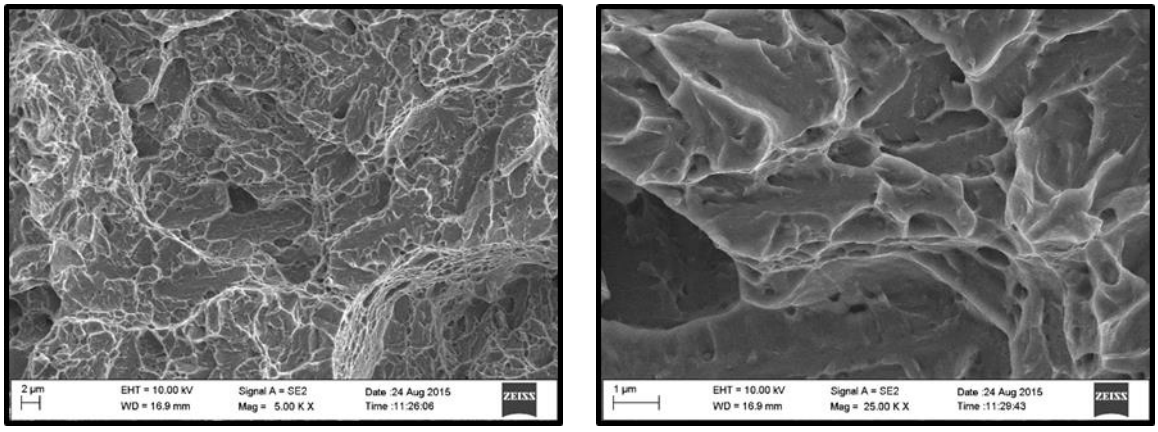

(a) (b)

Fig. 3.23 Initial H13 Impact Energy SEM Fracture Surface

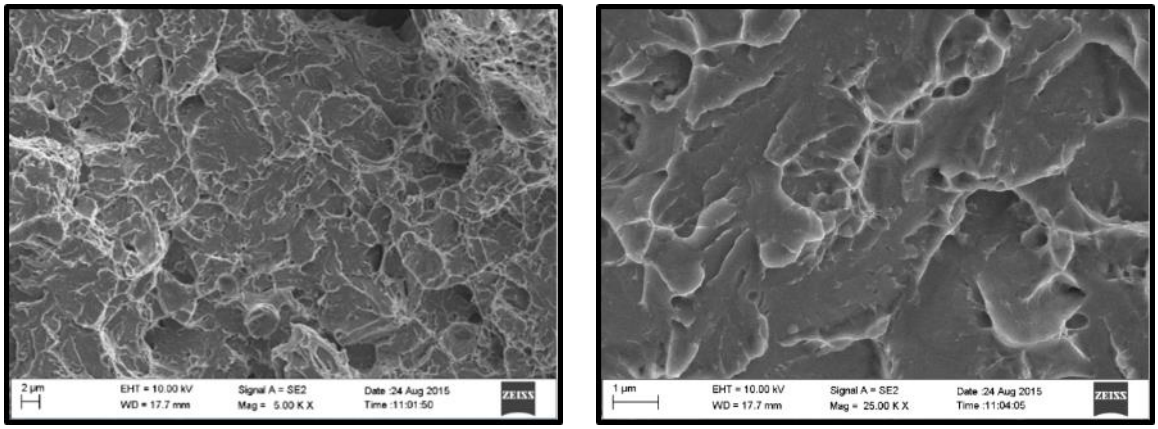

(a) (b)

Fig. 3.24 High H13 Impact Energy SEM Fracture Surface

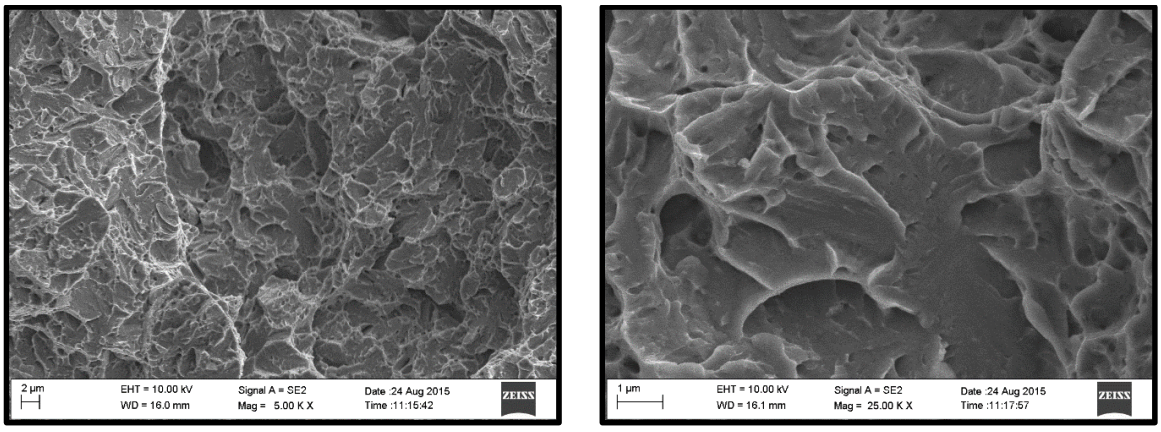

(a) (b)

Fig. 3.25 Low H13 Impact Energy SEM Fracture Surface

3.4.2 MP159 IZOD FRACTURE SURFACE SEM ANALYSIS

The nominal impact energy values for the MP159 Izod testing specimens, shown prior to fracture in Fig. 3.26(a), ranged from 278 kJ/m^2 to 414 kJ/m^2. The high nominal impact energy and the low nominal impact energy specimen is used for analysis of the fracture surface at an area in the center of the crack surface and at an area on the sharp shear lip. The Izod impact testing concluded that the initial specimens had the highest nominal impact energy while the lowest nominal impact energy was seen in the 50 hour 500 °C specimens. All specimens failed in a similar manner where a sharp shear lip was formed on the outer diameter, as shown in Fig. 3.26 (b).

(a) (b)

Fig. 3.26 MP159 Izod Specimen (a) and 3D Representation of Fracture Surface (b)

Similar to H13 the MP159 specimens failed by a microvoid coalescence process. However, in the central area of the MP159 facture surface there appears to be a variation in dimple sizes. This can be due to a non-uniform distribution of nucleating particles creating voids of various sizes [45]. Little variation is observed in the central area between the initial and low nominal impact energy specimens, shown in Fig. 3.27 and Fig. 3.28 respectively. The shear lip analysis though showed very uniform and essentially shallow equiaxed dimples. Not very much variation is observed in the shear lip area between the

initial and low nominal impact energy specimens, shown in Fig. 3.29 and Fig. 3.30 respectively. All other images taken for the central area and the shear lip at magnifications 100x – 50Kx can be seen in Appendix C Fig. C-4 through Fig. C-7.

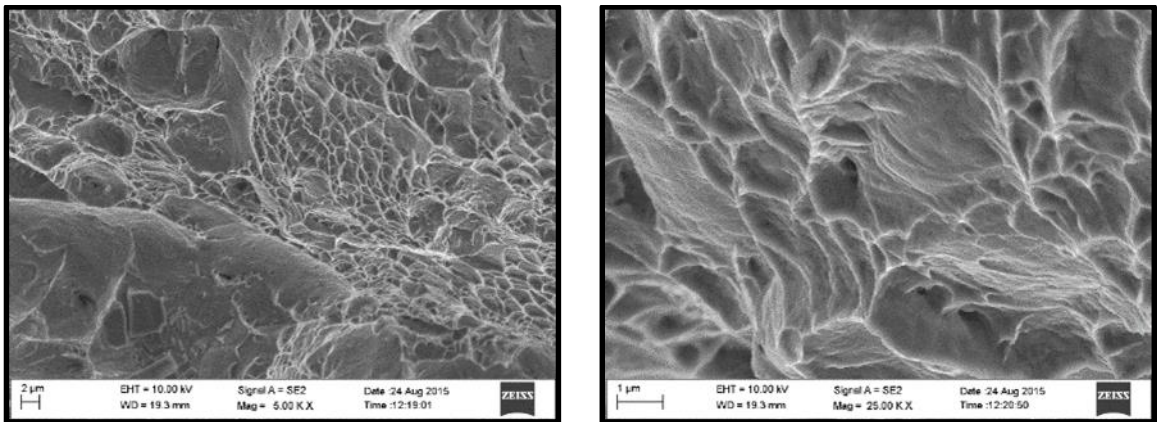

(a) (b)

Fig. 3.27 Initial MP159 Impact Energy SEM Fracture Surface

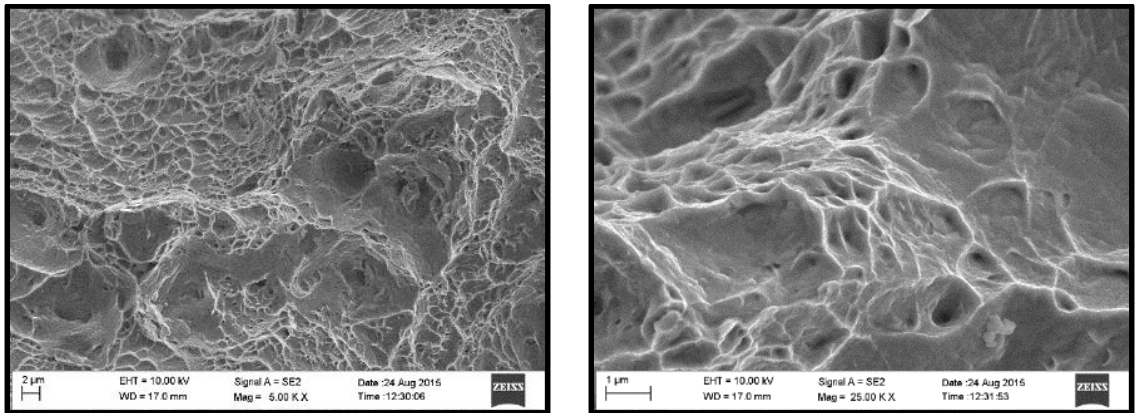

(a) (b)

Fig. 3.28 Low MP159 Impact Energy SEM Fracture Surface

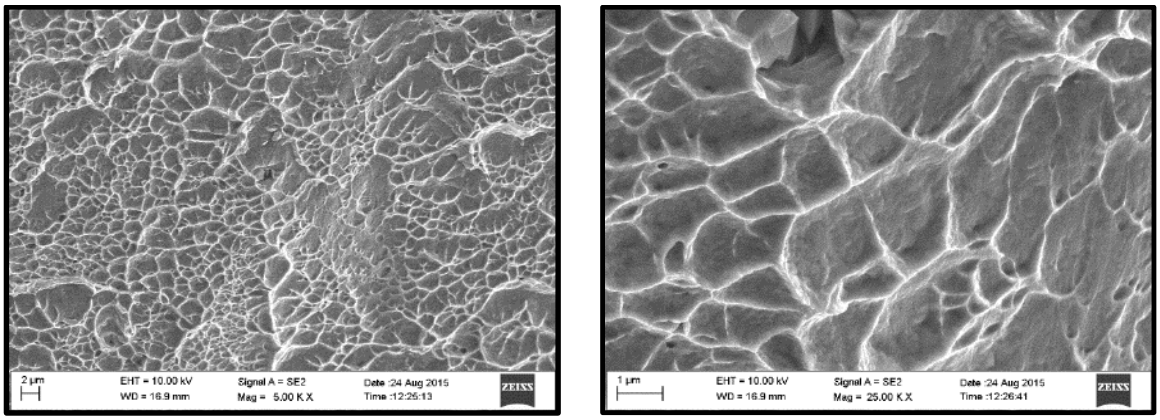

(a) (b)

Fig. 3.29 Initial MP159 Impact Energy Shear Lip SEM Fracture Surface

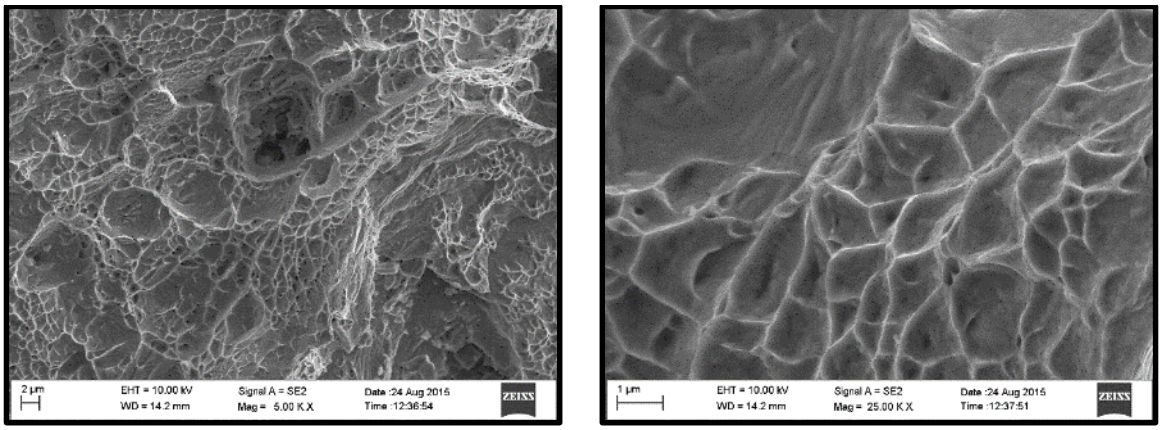

(a) (b)

Fig. 3.30 Low MP159 Impact Energy Shear Lip SEM Fracture Surface

3.4.3 TSP1 IZOD FRACTURE SURFACE SEM ANALYSIS

The nominal impact energy values for the TSP1 Izod testing specimens, shown prior to fracture in Fig. 3.31(a), ranged from 49.4 kJ/m^2 to 22.6 kJ/m^2. The high nominal impact energy and the low nominal impact energy specimen is used for analysis of the fracture. The Izod impact testing concluded that the initial specimens had the highest nominal impact energy while the lowest nominal impact energy was seen in the 20 hour 525 °C specimens. All specimens failed where a very small shear lip was formed behind the notch but essential the fracture is smooth and flat, as shown in Fig. 3.31 (b).

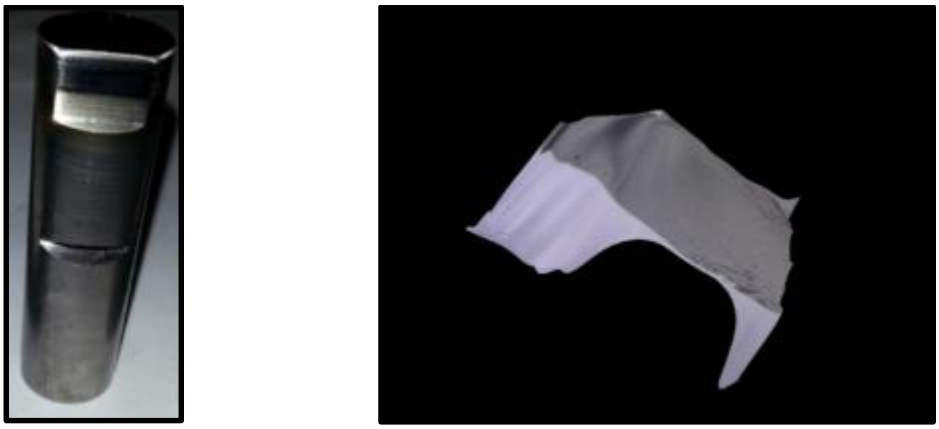

(a) (b)

Fig. 3.31 MP159 Izod Specimen (a) and 3D Representation of Fracture Surface (b)

The TSP1 specimens all failed at a significantly lower nominal impact energy value than the H13 and MP159 resulting in a much smoother fracture surface than the other material. However, SEM analysis revealed that the TSP1 specimens also failed by a microvoid coalescence process. The dimples present in the TSP1 fracture surface are significantly smaller than the ones observed in the H13 and MP159 specimens at the same 5000x and 25,000x magnifications. The reason for the smaller voids present is due to numerous nucleation sites forming and joining together before there is time for a larger void to grow [45]. A large reason for these nucleation size is the various particles that can be seen in the middle of many of the dimples present in the material matrix. The particles create a strain discontinuity in the structure under stress thus being more prone to plastic deformation. The plastic deformation then creates voids that with continual increase in stress will eventually coalesce into present fracture surface [45]. Little variation is seen in the fracture surface between the initial specimens, shown in Fig. 3.32, and the low impact energy specimens, shown in Fig. 3.33. All other images taken for the central area and the shear lip at magnifications 100x – 50Kx can be seen in Appendix C Fig. C-4 through Fig. C-7.

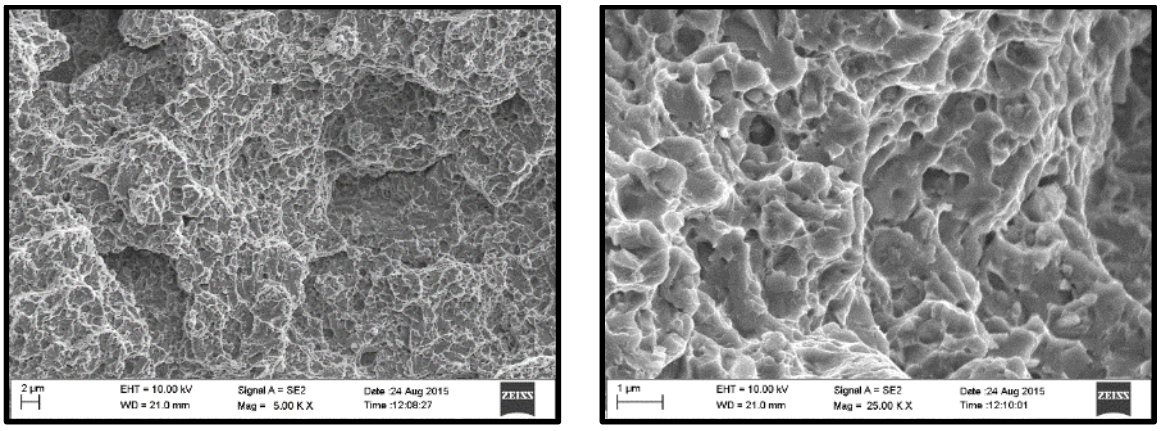

(a) (b)

Fig. 3.32 Initial TSP1 Impact Energy SEM Fracture Surface

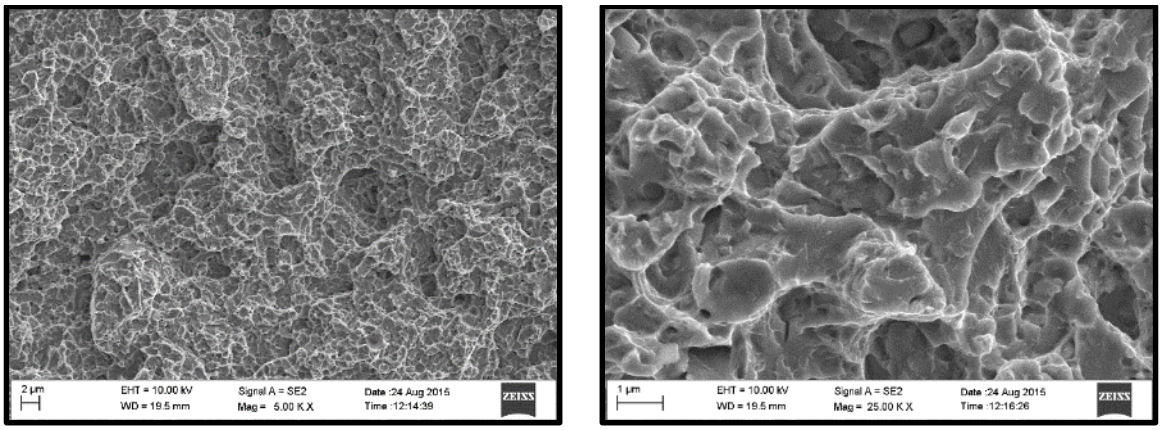

(a) (b)

Fig. 3.33 Low TSP1 Impact Energy SEM Fracture Surface

3.5 IZOD FRACTURE SURFACE ROUGHNESS CALCULATION

3.5.1 H13, MP159, & TSP1 SURFACE ROUGHNESS

The surface roughness of the fracture surfaces is obtained using a second order polynomial least square fitting function to calculate an average plane of best fit for the height data obtained using the live-depth up imaging application in the VHX-5000 digital microscope. The difference between the average plane height and the recorded height is the key component needed to calculate the surface roughness in terms of the arithmetic mean (*Ra*) and the root mean square average (*RMS*). To obtain a good statistical average the surface roughness is calculated based off of images taken at 200x, 500x, and 1000x magnifications. The accuracy of the microscopic height reading increases with magnification but the surface roughness value obtained is fairly localized. The surface roughness results of each of the materials along with each of the exposure scenarios and magnifications is shown in Fig. 3.34.

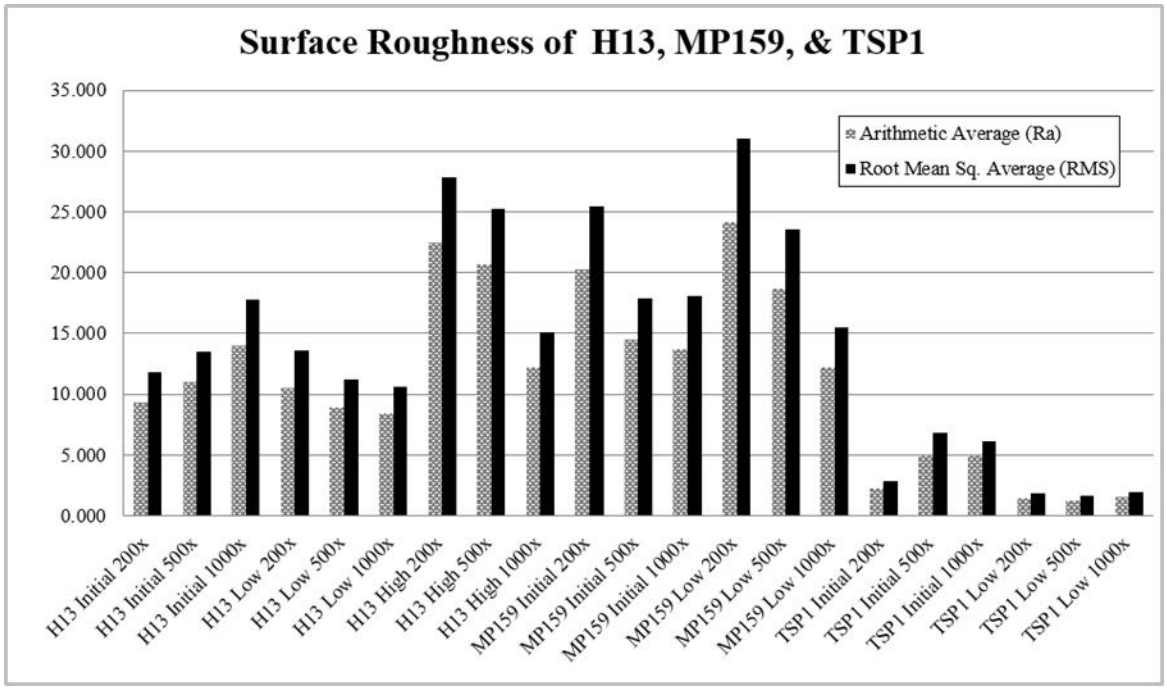

Fig. 3.34 Surface Roughness of H13, MP159, and TSP1

The MP159 specimens showed the highest value of surface roughness. This is as expected considering the MP159 specimens broke at the highest nominal impact energy values. Little deviation is seen in the surface roughness of MP159 between the initial and low energy specimens and similarly little deviation is seen in the nominal impact energy values of the MP159 specimens. The initial and low energy specimens of the H13 have a smoother fracture surface in comparison to the MP159 but the higher energy specimens formed fracture surfaces of similar roughness to MP159. The TSP1 specimens showed the lowest nominal impact energy strength being the reason for the small surface roughness values calculated with the lowest values present in the low energy specimens.

The nominal impact energy values obtained are plotted against the surface roughness values calculated at that specific nominal impact energy value in order to find a general relationship based off of the data for all three tool materials. These values are plotted independent of the specific welding temperature and time exposure condition that

corresponds to each of the nominal impact energy and surface roughness values. The graph of H13, TSP1, and MP159 nominal impact energy vs. surface roughness can be seen in Fig. 3.35. By plotting a linear line of best fit between all of the nominal impact energy vs surface roughness data point a direct relationship is observed such that as the nominal impact energy increases the surface roughness as well increase.

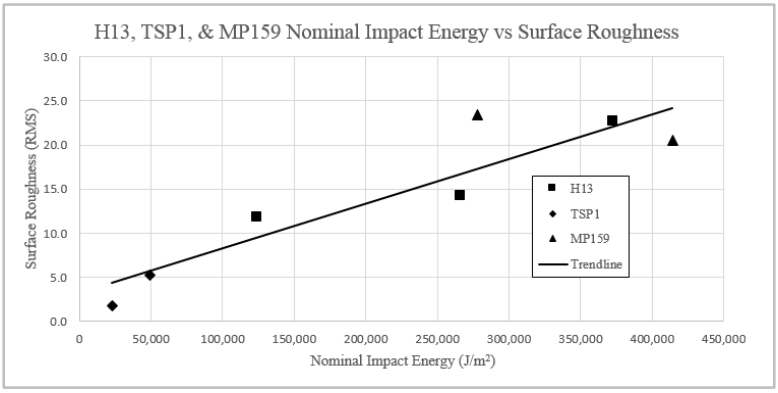

Fig. 3.35 H13, TSP1, & MP159 Nominal Impact Energy vs. Surface Roughness

Similarly the hardness is also plotted on a separate graph against the surface roughness values in order to find a relationship between two variables. These values are plotted independent of the specific welding temperature and time exposure condition that corresponds to each of hardness and surface roughness values. The graph of H13, TSP1, and MP159 hardness vs. surface roughness can be seen in Fig. 3.36. By plotting a linear line of best fit between all of the nominal impact energy vs surface roughness data point an indirect relationship is observed such that as the hardness increase in the tool materials the surface roughness will decrease.

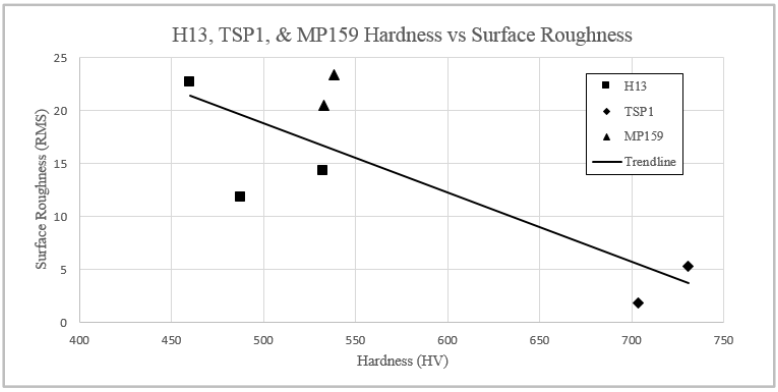

Fig. 3.36 H13, TSP1, & MP159 Hardness vs. Surface Roughness

3.6 Aluminum Diffusion: Experiment 1

3.6.1 H13

The H13 specimens used in the first aluminum diffusion experiment are analyzed using the Zeiss Ultra plus FE-SEM. The BSE images using the EsB detector are taken to get qualitative data about any presence of aluminum diffusion on the interface of the adhered aluminum alloy and the tool material boundary. The BSE image for the 50 hour 525°C specimens plunged into Al-5083 are shown in Fig. 3.37 (a) and the image for the specimens plunged into the Al-6061 are shown in Fig. 3.38 (a). A sharp transition from white to black is seen in both specimens meaning there is no evidence of aluminum diffusion. EDS compositional analysis was also performed to obtain quantitative data to determine if there is any effect of aluminum diffusion on the interface. An image is taken with the SE2 detector and is analyzed using the EDAX compositional analysis software. The compositional analysis showed a sharp increase in aluminum and sharp decrease in iron at the interface thus signifying no apparent aluminum diffusion, as shown in Fig. 3.37 (b) for the Al-5083 and Fig. 3.38 (b) for Al-6061. Since no aluminum diffusion is seen at the high temperature and time exposure conditions it was not necessary to analyze the room temperature specimen.

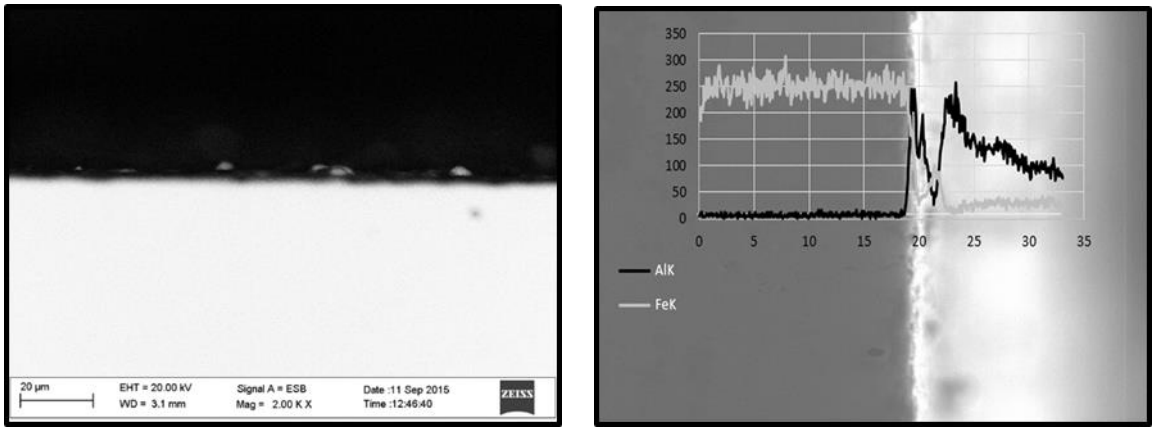

(a) (b)

Fig. 3.37 H13 w/ Al-5083 50 hr 525 °C Specimen: BSE (a) and EDS (b) Analysis

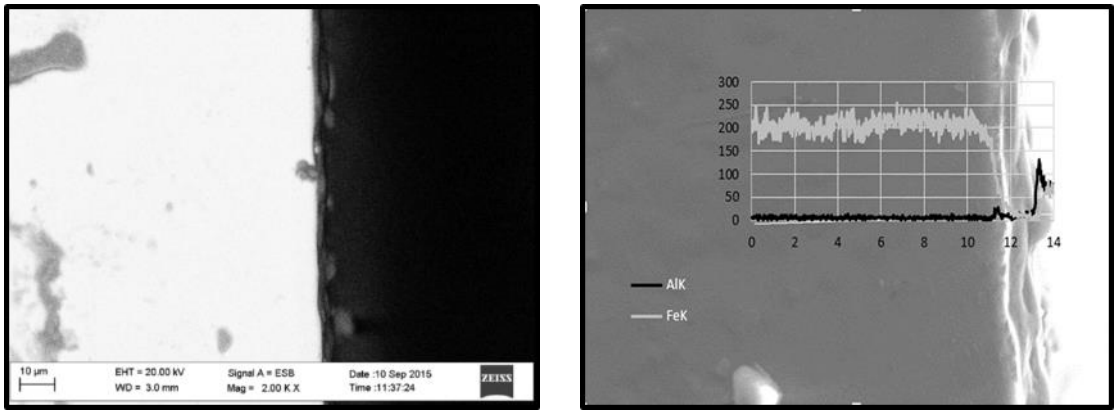

(a) (b)

Fig. 3.38 H13 w/ Al-6061 50 hr 525 °C Specimen: BSE (a) and EDS (b) Analysis

3.6.2 MP159

The MP159 specimens are analyzed in the same manner as the H13. The BSE image using the EsB detector for the 50 hour 525°C specimens plunged into Al-5083 are shown in Fig. 3.39 (a) and the image for the specimens plunged into the Al-6061 are shown in Fig. 3.40 (a). An aluminum diffusion surface reaction is apparent in the Al-6061specimen but the gray area at the interface is not conclusive evidence of aluminum penetration along grain boundaries. The EDS compositional analysis showed a sharp increase in aluminum and sharp decrease in cobalt at the interface thus aluminum diffusion could not be verified at this magnification, as shown in Fig. 3.39 (b) for the Al-5083 and Fig. 3.40 (b) for

Al-6061. Since only a small area of aluminum diffusion is seen in the high temperature and time exposure conditions it was not necessary to analyze the room temperature specimen.

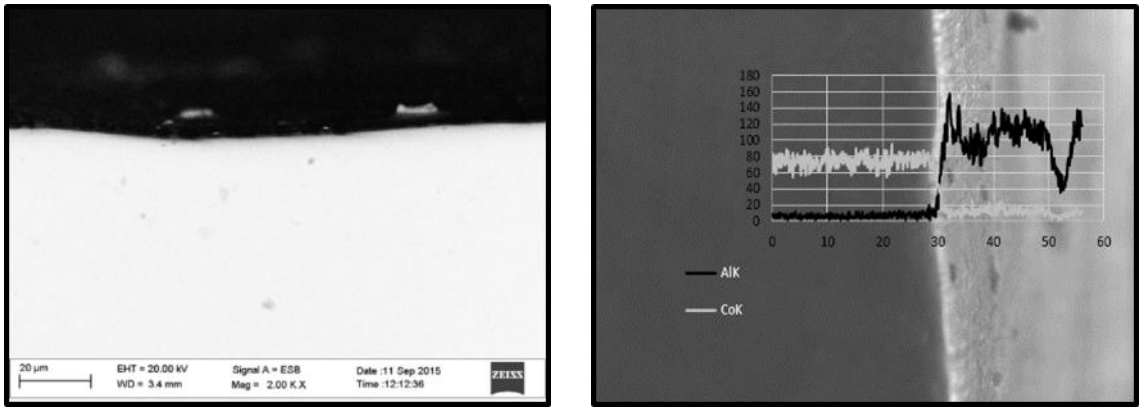

(a) (b)

Fig. 3.39 MP159 w/ Al-5083 50 hr 525 °C Specimen: BSE (a) and EDS (b) Analysis

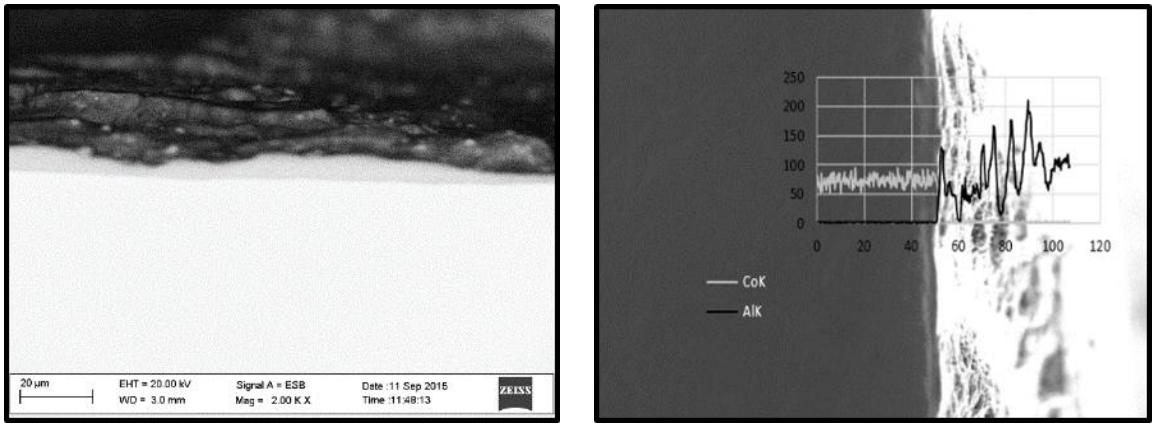

(a) (b)

Fig. 3.40 MP159 w/ Al-6061 50 hr 525 °C Specimen: BSE (a) and EDS (b) Analysis

3.6.3 TSP1

The TSP1 specimens are analyzed in the same manner as the H13 and MP159 specimens. The BSE image for the 50 hour 525°C specimens plunged into Al-5083 are shown in Fig. 3.41 (a) and the image for the specimens plunged into the Al-6061 are shown in Fig. 3.42 (a). A sharp transition from white to black is seen in both specimens meaning there is no evidence of aluminum diffusion. The EDS compositional analysis showed a sharp increase in aluminum and sharp decrease in iron at the interface thus signifying no

apparent aluminum diffusion as shown in Fig. 3.41 (b) for the Al-5083. The specimen that is plunged into the Al-6061 does appear to have some form of fluctuation in the compositional count at the interface between the aluminum alloy and the tool steel. While under proper conditions this would be signifying evidence of aluminum diffusion but this is not believe to be that case. Since only a small amount of aluminum is adhered the surface and the edge boundary could not be easily focused on it is believed that this fluctuation is merely due to edge effects and improper condition for analysis. Since no aluminum diffusion is seen in the high temperature and time exposure conditions it was not necessary to analyze the room temperature specimen.

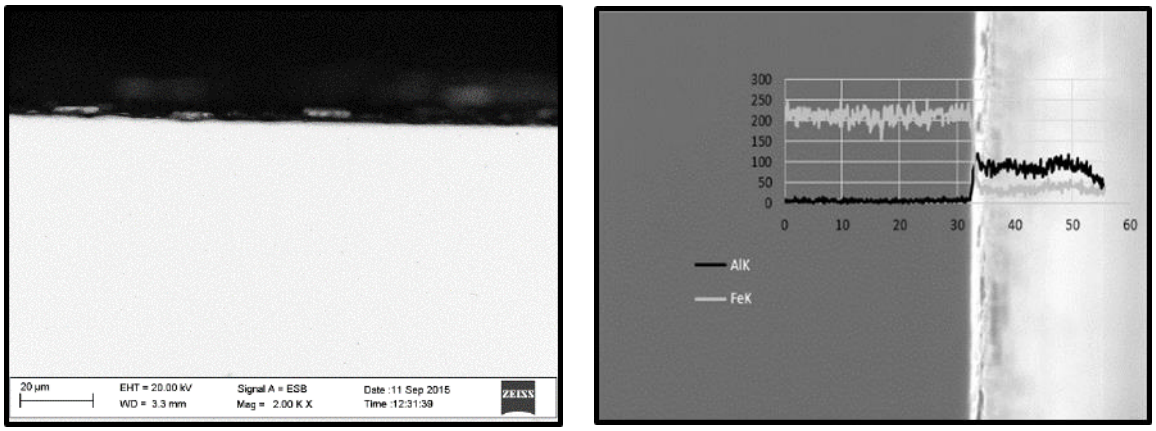

(a) (b)

Fig. 3.41 TSP1 w/ Al-5083 50 hr 525 °C Specimen: BSE (a) and EDS (b) Analysis

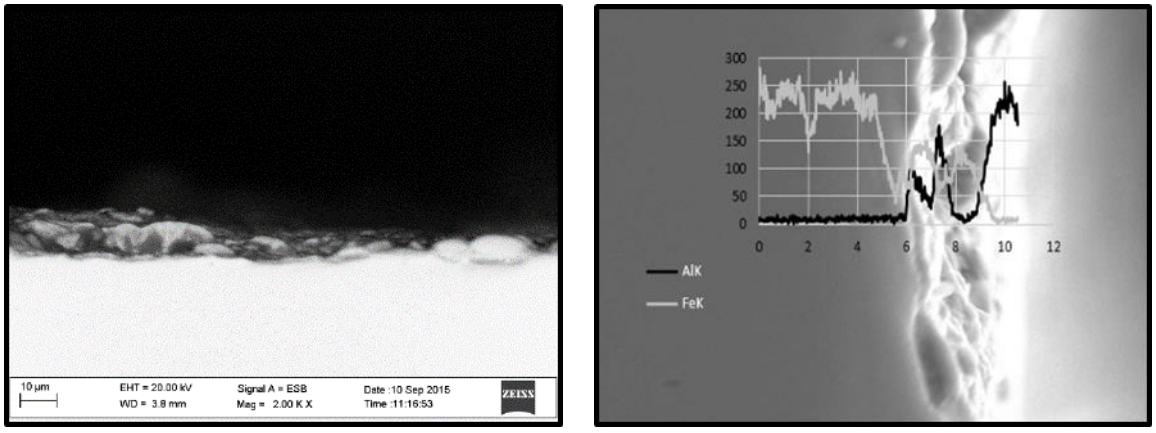

(a) (b)

Fig. 3.42 TSP1 w/ Al-6061 50 hr 525 °C Specimen: BSE (a) and EDS (b) Analysis

3.7 Aluminum Diffusion: Experiment 2

3.7.1 H13 Tool Shoulder Aluminum Diffusion Results: Experiment 2

The H13 tool shoulder specimens used in the second aluminum diffusion experiment are analyzed using the Zeiss Ultra plus FE-SEM. SE2 images of the interface between the aluminum alloy and tool material are taken at 100x and 250x magnifications of the initial and 525 °C for 200 hour specimens, as shown in Appendix D Fig. D-1 and Fig. D-2 respectively. The 250x SE2 images are then used for EDS compositional analysis where the compositional spectrums of the image for the initial and 525 °C for 200 hour specimens are shown in Fig. D-3 (a) and Fig. D-3 (b) respectively.

Iron and aluminum compositional analysis across the interface is also performed to test for the presence of aluminum diffusion in the initial and 525 °C for 200 hour specimens, as shown in Fig. 3.43 (a) and Fig. 3.43 (b) respectively. The initial specimen does show a slight transition from iron to aluminum but a high level of noise is apparent in values recorded and the analysis shows a lack of element composition after approximately the 210 µm position, meaning that the results are inaccurate and unreliable. The 525 °C for 200 hour specimen shows a sharp decrease in iron at the interface but instead of aluminum spiking at this point where the iron drops there is spike in silicon. This can explain the odd appearance of the aluminum surface and may be due to excessive colloidal silica polishing. Conclusively no evidence of aluminum diffusion is present in the specimens based off of the EDS compositional analysis.

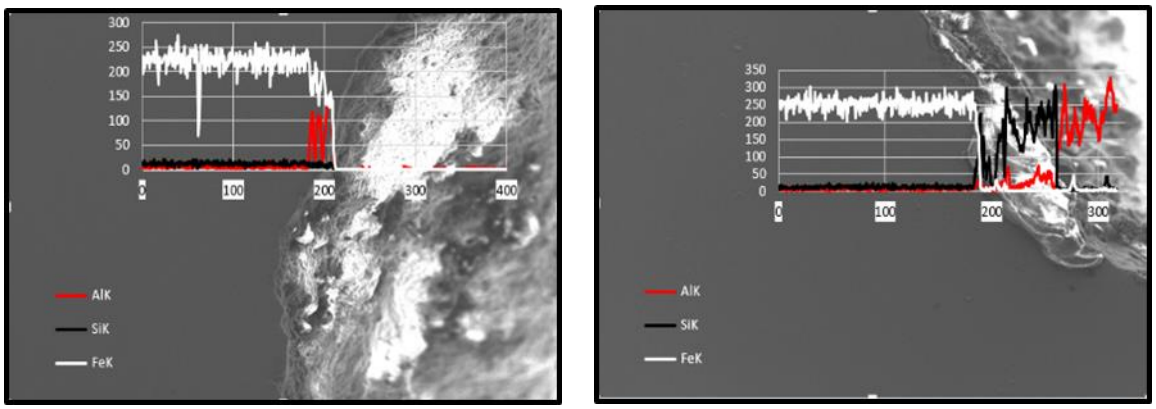

(a) (b)

Fig. 3.43 H13 Tool Shoulder Initial (a) & 525 °C 200 hour Specimen (b) EDS Analysis

BSE analysis is also performed using the EsB detector to obtain the qualitative data about possible presence of aluminum diffusion and the images for the initial and 525 °C for 200 hour specimen at 1000x magnification are shown in Fig. 3.44 (a) and Fig. 3.44 (b) respectively. The light colored region represent the H13 tool steel and the darker areas represent the aluminum and silicon materials. There is some evidence of darker particle being present in the tool material in the initial specimen showing evidence of a surface reaction at the interface. The 525 °C for 200 hour specimen appears to have darker particles as well in the tool material and these may be referred to as mechanically mixed layers (MML) [27] where high amount of heat, stress, and sliding can created a swirled mixture of material at the boundary of the tool material and aluminum. These layers can cause stress concentrations and contribute to the failure if excessive amount of tool material are degraded by the weaker aluminum material. The locations analyzed are not in the exact same positions for the initial vs exposed specimen and this may be the reason that the MML are not observed in the initial specimen but they are likely present along the interface in positions that have not been examined.

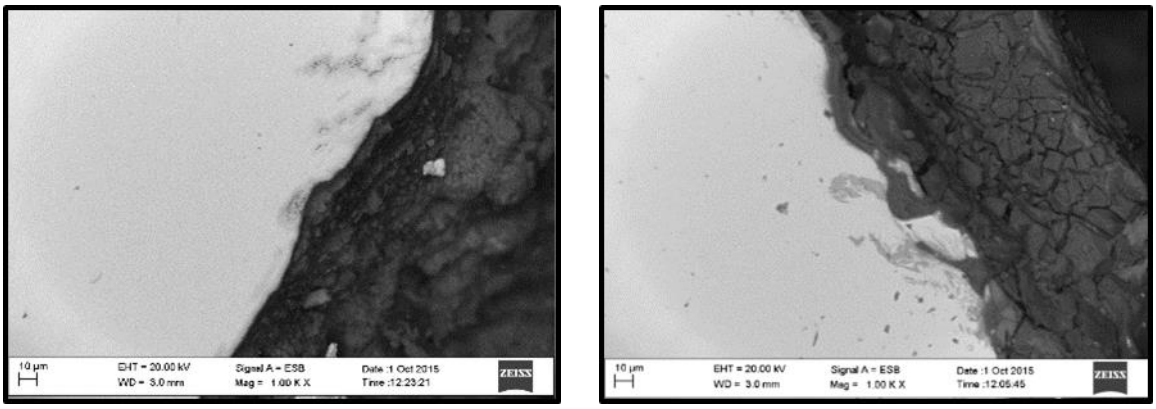

(a) (b)

Fig. 3.44 H13 Tool Shoulder Initial (a) & 525 °C 200 hour Specimen (b) BSE Analysis

3.7.2 TSP1 Tool Pin Specimen Aluminum Diffusion Results: Experiment 2

The TSP1 tool pin specimens used in the second aluminum diffusion experiment are analyzed using the Zeiss Ultra plus FE-SEM. SE2 images of the interface between the aluminum alloy and tool material are taken at 100x and 250x magnifications of the initial and 525 °C for 200 hour specimens, as shown in Appendix D Fig. D-4 and Fig. D-5 respectively. The 250x SE2 images are then used for EDS compositional analysis where the compositional spectrums of the image for the initial and 525 °C for 200 hour specimens are shown in Fig. D-6 (a) and Fig. D-6 (b) respectively.

Iron and aluminum compositional analysis across the interface is also performed to test for the presence of aluminum diffusion in the initial and 525 °C for 200 hour specimens, as shown in Fig. 3.45 (a) and Fig. 3.45 (b) respectively. The initial specimen shows a sharp transition between the TSP1 tool material and the aluminum region that appear to be heavily reacting on the surface with silicon. The 525 °C for 200 hour specimen shows an interesting trend where at approximately the 220 µm position there is an increase in iron and the aluminum composition remains constant and this region is not present in the initial specimen. This is evidence of aluminum diffusion and there is a non-uniform intermixture

of materials present in the 525 °C 200 hour specimen that is not present in the initial specimen but aluminum penetration along the grain boundaries is not observed.

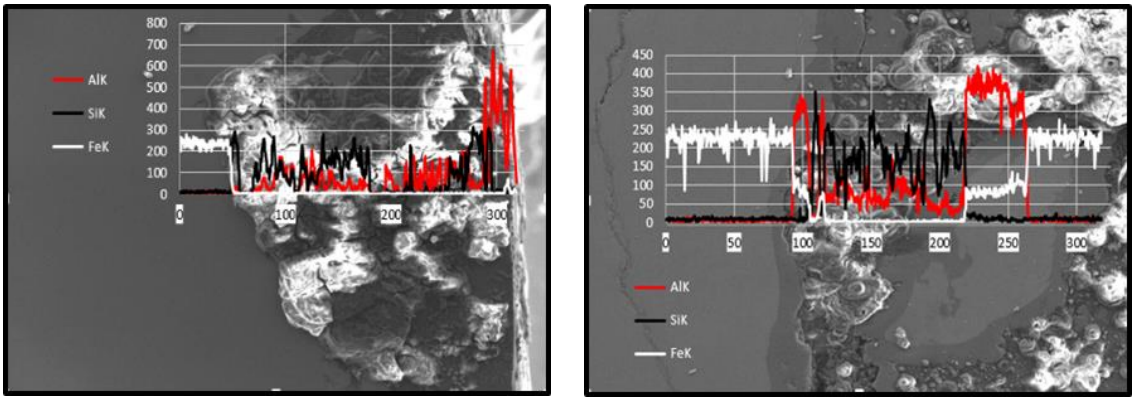

(a) (b)

Fig. 3.45 TSP1 Tool Pin Initial (a) & 525 °C 200 hour Specimen (b) EDS Analysis

BSE images using the EsB detector for the initial and 525 °C for 200 hour specimen at 1000x magnification are shown in Fig. 3.46 (a) and Fig. 3.46 (b) respectively. The light colored region represent the TSP1 tool steel and the darker areas represent the aluminum and silicon materials. There is some evidence a lighter region being present in the aluminum/silicon region in the initial specimen and this could be evidence of MML [27]. The 525 °C for 200 hour specimen shows where that iron is present on both the left and right of an aluminum/silicon region and thus an intermixture of materials is present which can degrade the quality of the TSP1 tool pin.

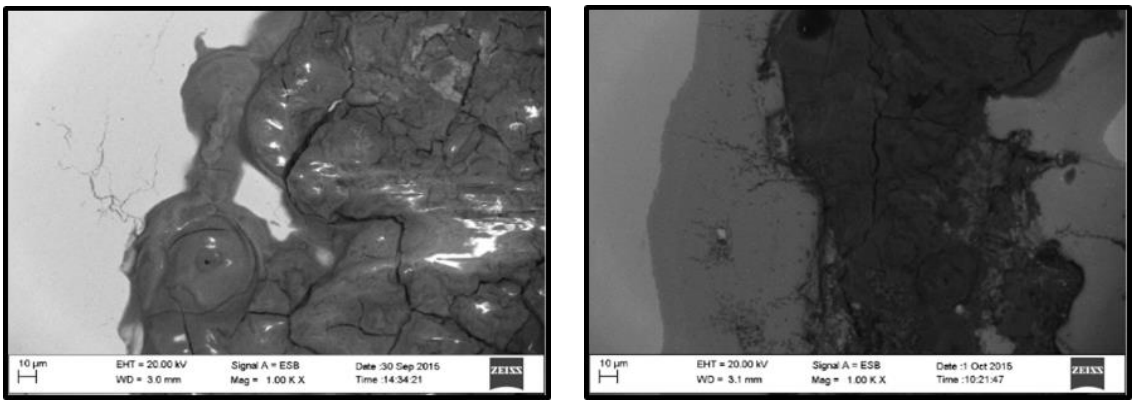

(a) (b)

Fig. 3.46 TSP1 Tool Pin Initial (a) & 525 °C 200 hour Specimen (b) BSE Analysis

3.7.3 MP159 Tool Pin Specimen #1 Aluminum Diffusion Results: Experiment 2

The first MP159 tool pin specimen (MP159-1) used in the second aluminum diffusion experiment are analyzed using the Zeiss Ultra plus FE-SEM. SE2 images of the interface between the aluminum alloy and tool material are taken at 100x and 250x magnifications of the initial and 525 °C for 200 hour specimens, as shown in Appendix D Fig. D-7 and Fig. D-8 respectively. The 250x SE2 images are then used for EDS compositional analysis where the compositional spectrums of the image for the initial and 525 °C for 200 hour specimens are shown in Fig. D-9 (a) and Fig. D-9 (b) respectively.

Cobalt and aluminum compositional analysis across the interface is also performed to test for the presence of aluminum diffusion in the initial and 525 °C for 200 hour specimens, as shown in Fig. 3.47 (a) and Fig. 3.47 (b) respectively. The initial specimen shows a heavy infiltration of silicon and no presence of aluminum diffusion. The 525 °C for 200 hour specimen shows the same relationship as the initial specimen and no evidence of aluminum diffusion is present.

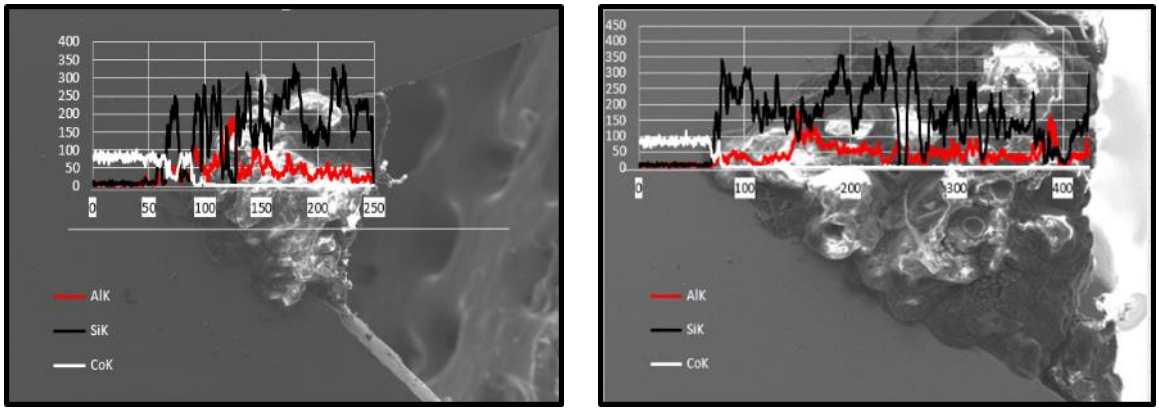

(a) (b)

Fig. 3.47 MP159-1 Tool Pin Initial (a) & 525 °C 200 hour Specimen (b) EDS Analysis

BSE images using the EsB detector for the initial and 525 °C for 200 hour specimen at 1000x magnification are shown in Fig. 3.48 (a) and Fig. 3.48 (b) respectively. The light

colored region represent the MP159 tool material and the darker areas represent the aluminum and silicon materials. The initial specimen appears to have a heavy intermixture of materials at the interface between the MP159 tool material and the aluminum alloy which may again be evidence of MML [27] creating stress concentrations and degradation issues in the tool. The 525 °C for 200 hour specimen shows a similar surface reaction where darker particles are present in the lighter region and swirling pattern of heavy and dark particles at the MP159 tool pin and aluminum alloy interface.

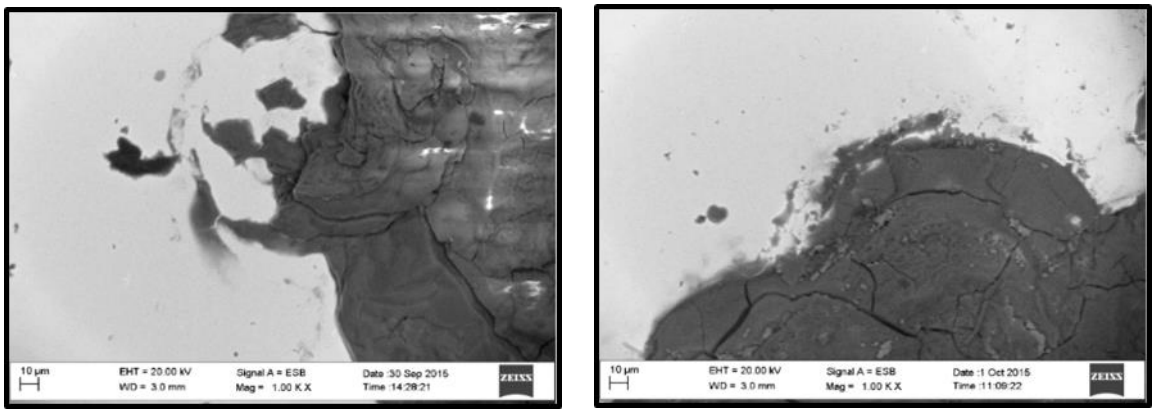

(a) (b)

Fig. 3.48 MP159-1 Tool Pin Initial (a) & 525 °C 200 hour Specimen (b) BSE Analysis

3.7.4 MP159 Tool Pin Specimen #2 Aluminum Diffusion Results: Experiment 2

The second MP159 tool pin specimen (MP159-2) used in the second aluminum diffusion experiment are analyzed using the Zeiss Ultra plus FE-SEM. SE2 images of the interface between the aluminum alloy and tool material are taken at 100x and 250x magnifications of the initial and 525 °C for 200 hour specimens, as shown in Appendix D Fig. D-10 and Fig. D-11 respectively. The 250x SE2 images are then used for EDS compositional analysis where the compositional spectrums of the image for the initial and 525 °C for 200 hour specimens are shown in Fig. D-12 (a) and Fig. D-12 (b) respectively.

Cobalt and aluminum compositional analysis across the interface is also performed to test for the presence of aluminum diffusion in the initial and 525 °C for 200 hour specimens, as shown in Fig. 3.49 (a) and Fig. 3.49 (b) respectively. The initial specimen shows a heavy infiltration of silicon and no presence of aluminum diffusion. The 525 °C for 200 hour specimen shows the same relationship as the initial specimen and no evidence of aluminum diffusion is present.

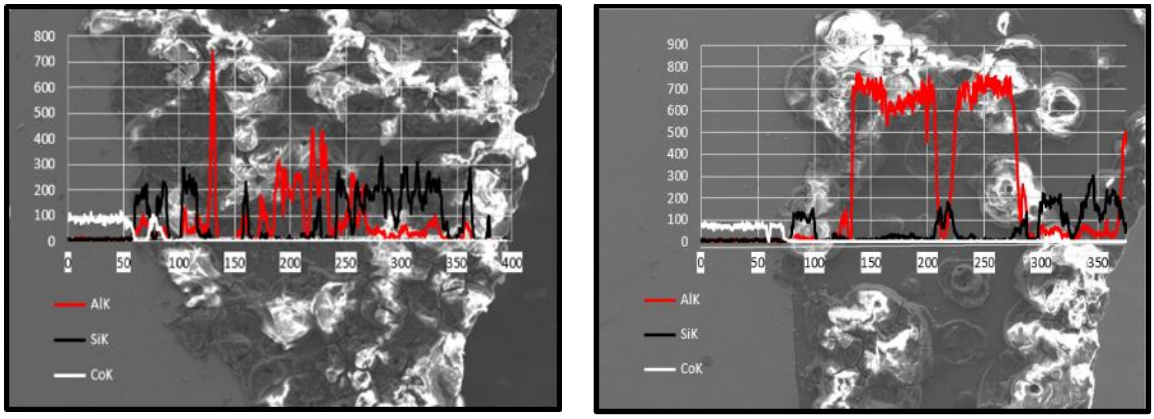

(a) (b)

Fig. 3.49 MP159-2 Tool Pin Initial (a) & 525 °C 200 hour Specimen (b) EDS Analysis

BSE images using the EsB detector for the initial and 525 °C for 200 hour specimen at 1000x magnification are shown in Fig. 3.50 (a) and Fig. 3.50 (b) respectively. The light colored region represent the MP159 tool material and the darker areas represent the aluminum and silicon materials. The initial specimen has a region of dense particles present in in aluminum/silicon region which may again be evidence of MML [27]. The 525 °C for 200 hour specimen shows an interesting reaction that can be seen by the light colored region on the left, a darker region on the right, and an intermediate region that appears to contain a mixture of light and dark particles. This inhomogeneous region is likely due to aluminum diffusion but further analysis is needed for this to be definitively concluded.

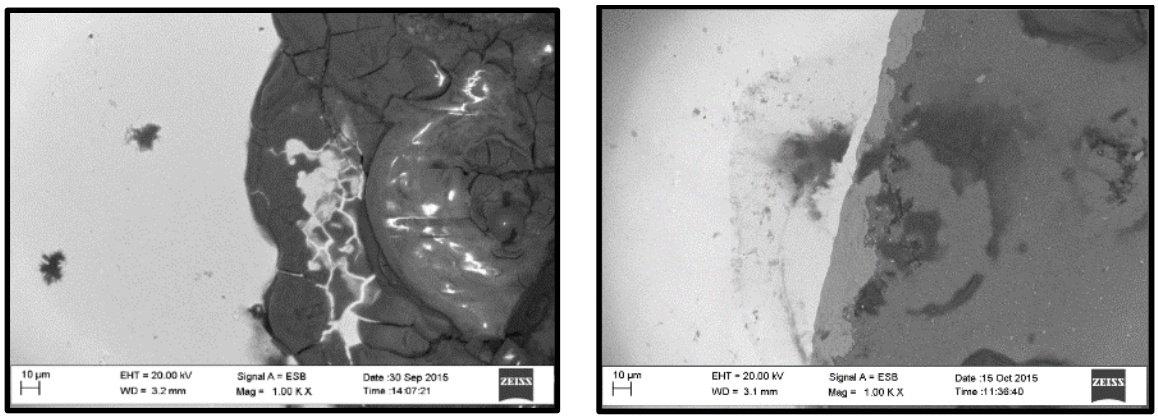

(a) (b)

Fig. 3.50 MP159-2 Tool Pin Initial (a) & 525 °C 200 hour Specimen (b) BSE Analysis

3.7.5 MP159 Tool Pin Specimen #3 Aluminum Diffusion Results: Experiment 2

The third MP159 tool pin specimen (MP159-3) used in the second aluminum diffusion experiment are analyzed using the Zeiss Ultra plus FE-SEM. SE2 images of the interface between the aluminum alloy and tool material are taken at 100x and 250x magnifications of the initial and 525 °C for 200 hour specimens, as shown in Appendix D Fig. D-13 and Fig. D-14 respectively. The 250x SE2 images are then used for EDS compositional analysis where the compositional spectrums of the image for the initial and 525 °C for 200 hour specimens are shown in Fig. D-15 (a) and Fig. D-15 (b) respectively.

Cobalt and aluminum compositional analysis across the interface is also performed to test for the presence of aluminum diffusion in the initial and 525 °C for 200 hour specimens, as shown in Fig. 3.51 (a) and Fig. 3.51 (b) respectively. There is a sharp transition between cobalt and aluminum compositions at the interface between the two materials and thus no evidence of aluminum diffusion can conclusively be determined based off of the EDS compositional analysis. Interestingly though there is no evidence of silicon infiltration in this specimen and this may be contributed the compositional

differences in the aluminum alloys that were being welded using this MP159 tool in comparison to the other tool pins.

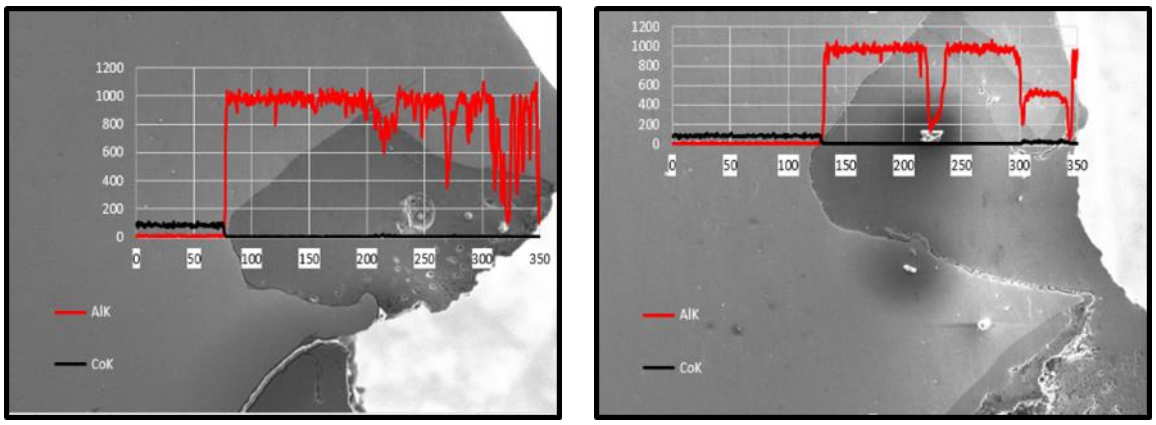

(a) (b)

Fig. 3.51 MP159-3 Tool Pin Initial (a) & 525 °C 200 hour Specimen (b) EDS Analysis

BSE images using the EsB detector for the initial and 525 °C for 200 hour specimen at 1000x magnification are shown in Fig. 3.52 (a) and Fig. 3.52 (b) respectively. The light colored region represent the MP159 tool material and the darker areas represent the aluminum material. The initial specimen showed no evidence of material intermixture of aluminum diffusion but the 525 °C for 200 hour specimen shows a reaction that has not been seen in the previous specimens where at the aluminum/tool material boundary there is a dark region that is approximately 2 µm thick that is not present in the initial specimen.

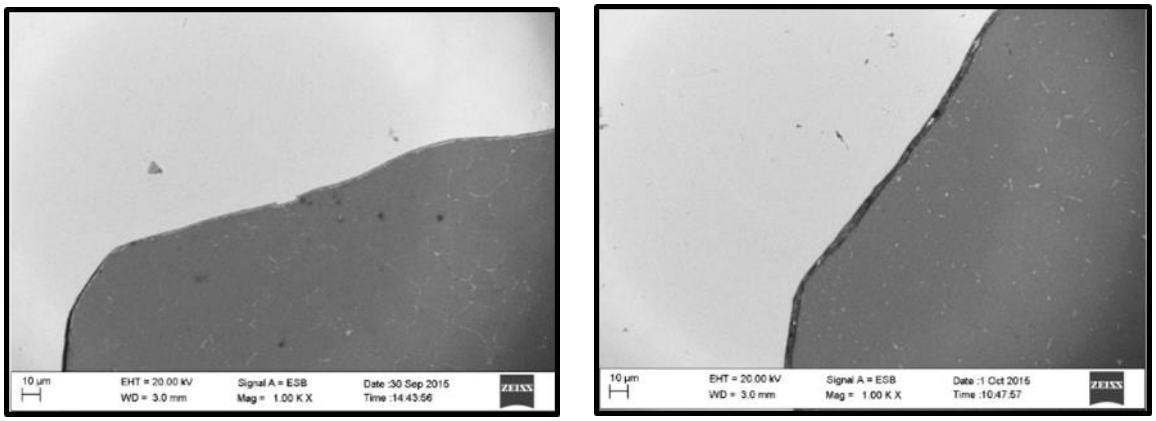

(a) (b)

Fig. 3.52 MP159-3 Tool Pin Initial (a) & 525 °C 200 hour Specimen (b) BSE Analysis

Further investigation into the composition of the boundary reaction is conducted using the cobalt and aluminum EDS compositional analysis across the interface along with the EsB analysis of the interface, as shown in Fig. 3.53 (a) and (b) respectively. There is a region where the EDS analysis shown a gradual decrease in the iron composition at the same location where there is a gradual increase in aluminum composition. Evidence of this inhomogeneous region can also be seen in the EsB analysis where there is an intermediate lightly shaded area between the heavy tool particles and the lighter aluminum particles. The 2 µm thick region at this interface is an aluminum diffusion surface reaction that has created a void where compositional analysis could not be conducted.

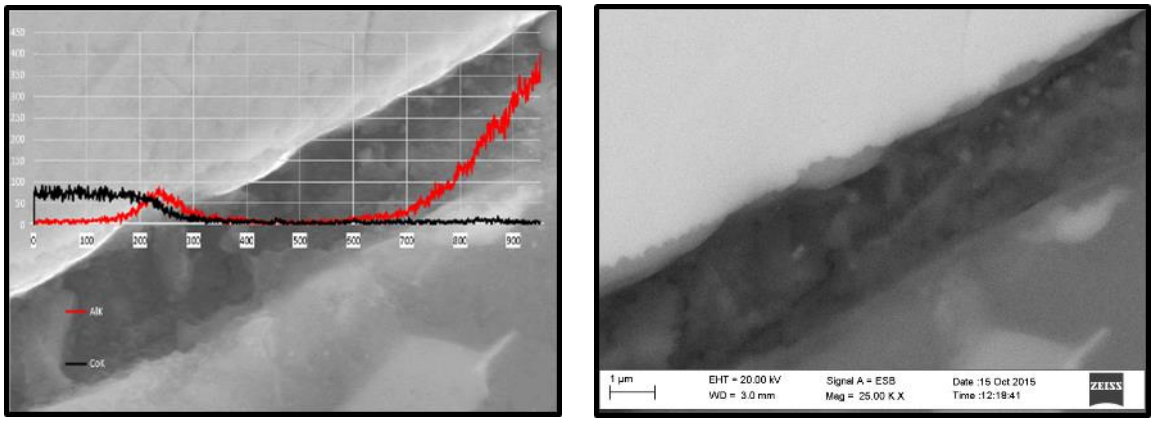

(a) (b)

Fig. 3.53 MP159-3 Tool Pin 525 °C 200 hour Specimen EDS (a) & BSE (b) Analysis

CHAPTER 4

CONCLUSIONS

H13, MP159, and TSP1 FSW tool materials have been exposed to various welding temperatures and time conditions to mimic the thermal environment created during FSW of aluminum alloys. The purpose of this study is to investigate friction stir welding tool material degradation factors due variation in tool material properties and the effect of an aluminum diffusion wear mechanism on H13, TSP1, and MP159 when exposed to various welding temperatures and times. Conclusion about degradation factors have been made based off of the experimental results from the metallographic images, hardness testing, Izod impact energy, fracture surface analysis of Izod specimens, surface roughness analysis of Izod specimens, and aluminum diffusion experiments.

4.1 METALLOGRAPHIC IMAGING

The metallographic images are taken of the tool materials in their initial heat-treated state to observe the variation in microstructural properties. After each of the tool materials are properly heat treated they are cut into ¼" disk and mounted in an epoxy based for polishing. The specimens are finely polished up to a 3μm finish to obtain quality metallographic images. From the metallographic images obtained it has been concluded that:

- For H13 a 2% Nital immersion followed by the Viella's Reagent immersion etch can be used to observe chromium carbide precipitates that help strengthen the material matrix.
- For MP159 a Special #5 immersion etch can be used to observe the grain size and precipitates along with the presence of martensite and twinning in the material matrix.
- For TSP1 2% Nital immersion followed by the Viella's Reagent immersion etch can be used to observe the fine dispersion of carbide precipitates and the grain boundaries present in the material matrix.

4.2 Hardness Testing

The hardness of the initial post-heat treated materials is compared to specimens that are exposed to 400 °C, 450 °C, 500 °C, and 525 °C welding temperature in time increments of ½ hour, 1 hour, 5 hour, 20 hour, and 50 hours using a pot furnace salt bath for welding temperature and time exposure. From the hardness test conducted it can be concluded that:

- Decarburization is observed on the H13 tool surface due to the effect of the oxygen rich atmosphere present in the convection oven used for initial heat treatment. The weaker decarburized surface area will have insufficient material properties for FSW and must be removed when fabricating FSW tools from H13 so that tool failure does not occur.
- The maximum and minimum hardness for the H13 was 550 HV at 50 hours simulated at 400 °C and 460 HV at 50 hours simulated at 525 °C. Due to the decrease in hardness at higher temperatures it is recommended that H13 tool materials be used to weld softer alloys that have high thermal conductivity and high

specific heat properties so that elevated welding temperature will not be needed to plasticize the base material.

- All MP159 specimens revealed a significant decrease in hardness at points approaching the center of specimen and this is believed to be due to the cold drawing of the MP159. It is recommended that all MP159 tools be fabricated from round rods that are similar in diameter to the final tool so that minimal material will have to be removed and the material with the highest possible hardness is located at the exterior surface of the tool.
- No detrimental hardness change is observed in any of the MP159 400 °C, 450 °C, 500 °C, 525 °C specimens. The maximum and minimum hardness for the MP159 was 550 HV at 50 hours simulated at 500 °C and 526 HV at 50 hours simulated at 400 °C. MP159 can be used as a primary FSW tool material for base materials that require a welding temperature in the range of 400 °C to 525 °C. However, age hardening is conducted at 660 °C and thus MP159 material properties will begin to destabilize if the welding temperatures approaches this critical value but this is not an issue for the welding of aluminum alloys since the welding temperature will never reach this critical point.
- The maximum and minimum hardness for the TSP1 was 813 HV at 5 hours simulated at 400 °C and 704 HV at 20 hours simulated at 525 °C. Although there is reduction in hardness at higher welding temperatures and times, the hardness of TSP1 is still significantly higher than H13 and MP159. For this reason TSP1 is least likely of all three tool materials to experience tool wear when welding aluminum alloys.

4.3 IZOD IMPACT ENERGY TESTING

Based off of the maximum and minimum hardness values obtained specimens for the Izod impact energy testing are chosen. From the Izod impact energy tests conducted it can be concluded that:

- H13 Izod specimens failed between the nominal impact energy value of 123.7 kJ/m^2 with a 525 °C for 1/2 hours specimen and 372.4 kJ/m^2 with a 525 °C for 50 hours specimen.
- MP159 Izod specimens failed between the nominal impact energy value of 302.2 kJ/m^2 with a 450 °C for 50 hours specimen and 414.1 kJ/m^2 with an initial room temperature specimen. MP159 requires the greatest amount of energy to create failure and thus MP159 should be chosen over the other two materials if high fracture toughness is needed.
- TSP1 Izod specimens failed between the nominal impact energy value of 22.6 kJ/m^2 with a 525 °C for 20 hours specimen and 49.4 kJ/m^2 with an initial room temperature specimen. TSP1 needs the least amount of energy to create failure and thus is most likely to fail due to spikes in loading conditions where high fracture toughness is needed.
- When comparing hardness to nominal impact energy an inverse relationship is observed whereas hardness increases the nominal impact energy will decrease. Thus lower hardness materials such as H13 and MP159 should be chosen over TSP1 if fracture toughness is a concern for the specific welding process needed. If TSP1 has to be used due to its superior hardness property then the processing parameters should be adjusted to minimize mechanical loading conditions.

4.4 Izod Fracture Surface and Surface Roughness Analysis

Based off of the high and low nominal impact energy values obtained from the Izod impact testing the specimens for the fractography analysis. From the Izod specimen fractography and surface roughness experiments it has been concluded that:

- All three materials failed by the microvoid coalescence process which is evidence of a ductile failure mode.
- MP159 showed the greatest non-uniformity in the dimples sizes due to a non-uniform particulate dispersion.
- TSP1 revealed significantly smaller dimples in comparison to the MP159 and H13 and this is due to a large number of nucleation site being formed in close proximity to each other forcing voids to insufficiently grow to a larger size.
- Variations were not observed in fractography surface when comparing the high and low energy specimens to one another.
- As nominal impact energy increase the surface roughness of the three materials also increases showing a direct relationship between the two. This is the reason the highest surface roughness is observed in the MP159 material that also required the highest nominal impact energy in order to fail.
- Conversely as hardness increase the surface roughness of the three materials will decrease showing an inverse relationship between the two. This is the reason that TSP1 has a much smoother fracture surface that can be macroscopically observed, resembling a brittle failure mode. However, the SEM analysis showed that TSP1 does in fact have a ductile fracture surface and cannot be considered a brittle material.

4.5 Aluminum Diffusion Testing

Two different aluminum diffusion experiment are conducted. The first test is performed by using a FSW machine to plunge the three different tool material into two different base material, Al-5083 and Al-6061, such that a layer of aluminum can adhere to the tool material surface. The second experiment is conducted using a previously operational H13 tool shoulder, a failed TSP1 pin, and three different MP159 pins that have various levels of aluminum alloy welding exposure. Each of the experiments are analyzed with a scanning electron microscope (SEM) using an energy selective backscatter (EsB) detector for backscattered electron images (BSE) to obtain qualitative data and energy dispersive spectroscopy (EDS) is used for compositional analysis to obtain quantitative data about the presence of aluminum diffusion at the interface of the aluminum and tool material. From aluminum diffusion experiment it has been concluded that:

- From the aluminum diffusion experiment 1 there was no conclusive evidence of aluminum diffusion created in the 50 hour 525°C specimens for H13 and TSP1 thus an analysis of the initial specimens was not pertinent.
- The MP159 specimen coated with Al-6061 did show evidence of an aluminum diffusion surface reaction at the interface between the tool material and aluminum alloy but penetration of aluminum along the grain boundaries is not observed. This shows that MP159 has a higher surface reactivity to aluminum alloys in comparison to H13 and TSP1 since this reaction was not observed in the other two materials.
- From the aluminum diffusion experiment 2 there was conclusive evidence of aluminum diffusion and/or MML created in the initial and the 200 hour 525°C specimens.

- Evidence of possible mechanically mix layers (MML) is seen in the H13 200 hour 525°C specimen and these MML can result in tool material erosion and premature tool failure.
- TSP1 200 hour 525°C specimens did show a region that had a substantial reaction with the aluminum that was not present in the initial specimen but that is believed to be due to aluminum diffusion.
- MP159 also show evidence of mechanically mixed layers in the first and second pins analyzed. In the second MP159 tool pin there was also a region at the interface between the tool material and the aluminum alloy that appears to have a composition that is more dense than aluminum but less dense than the tool material. This region is believed to be created by aluminum diffusion.
- In the third MP159 specimen there is also an aluminum diffusion surface reaction that is formed at the interface between the tool material and aluminum alloy. A void is created at the interface in the 200 hour 525°C specimen that is not present in the initial specimen. Compositional analysis shows a slight transition between the aluminum and cobalt compositions which is quantitative evidence of aluminum diffusion.
- The second aluminum diffusion experiment showed that all three materials are affected by the welding of aluminum alloys, but MP159 shows the greatest level of reactivity. Aluminum diffusion surface reactions and/or MML is observed in each of the materials but aluminum penetration along grain boundaries is not observed. These surface reactions and MML can lead to tool material embrittlement that will induce tool material degradation and in extreme situations could lead to tool failure.

CHAPTER 5

RECOMMENDATIONS FOR FUTURE WORK

The following is recommendations for future work involving the investigation of tool material degradation due FSW of aluminum alloys. Possible experiments that can be conducted to further this research are automated ball indentation testing, high temperature Izod testing, H13 hardness evolution after tempering testing, high temperature rotating-beam reverse-bending testing, and controlled aluminum diffusion testing.

5.1 AUTOMATED BALL INDENTATION TESTING

Automated Ball Indentation (ABI) testing can be used to calculate a materials true stress/strain curve, yield strength, elastic modulus, local fracture toughness, and strain-hardening exponent [46]. The experiment is conducted using a spherical indenter that is use to penetrate the surface of a polished material in multiple locations and the indentations are all strain-controlled. The materials needed for the testing method are "an electromechanically driven indenter, high-resolution penetration transducer and load cell, a personal computer, 16-bit data acquisition/control unit, and copyrighted ABI software" [46]. The ABI testing is a non-destructive alternative to common destructive tensile testing methods and this is especially valuable for the testing of these materials due to the high level of difficulty in the fabrication of tensile specimens out of the high hardness tool materials. The testing method is a quick, reliable, cheap, and simple procedure that can be conducted to calculate valuable mechanical properties of H13, TSP1, and MP159.

5.2 High Temperature Izod Testing

All Izod testing conducted for the tool material degradation study was performed at room temperature after the tool materials were exposed to specific temperature and time conditions. However, the tool materials experience the FSW loads at elevated temperatures and because of this material properties, such as impact energy, will vary in comparison to room temperature values. The high temperature Izod testing can be conducted using a Tinius Olsen Impact Tester, an induction heater, and tongs for safe material handling. The induction heater and the impact tester need to be situated in close vicinity of one another so that the tool materials are not cooled and the experiment is capable of being conducted at the desire temperature. Once the specimen is transferred from the induction heater into the testing apparatus and securely fastened, the swinging hammer arm can be release so that the impact energy at the desire temperature can be determined.

5.3 H13 Hardness Evolution after Tempering Testing

Further hardness experimentation can be conducted to better understand the hardness evolution of H13 tool steel after tempering. Tempering operations are conducted by Thyssen-Krupp for the TSP1 and since MP159 is not a martensite former it cannot be tempered. However, tempering is sometimes performed on the H13 material for FSW applications and because of this the hardness evolution after tempering needs to be experimentally investigated. Tempering is typically conducted after quenching and is performed by heating the material, to a relatively low temperature, and holding that material at that temperature for a specific time followed by a slow air cooling. Tempering is used to increase ductility and toughness but these improved properties come at the cost of a reduction in tensile strength, and yield strength [47]. An increase in hardness has been

observed after tempering H13 at 400 °C and that means that the hardness evolution that has been experimentally determine in this tool material degradation study is only accurate for H13 after it has been quenched and not tempered. The same hardness testing procedure and exposure conditions used in this experimental study can be used to determine the hardness evolution of H13 after tempering.

5.4 High Temperature Rotating-Beam Reverse-Bending Testing

Rotating-beam reverse-bending testing is a fatigue testing procedure that is use to determine fatigue properties, such as material endurance limit and cyclic fatigue strength, so that an estimation of when fatigue failure will occur can be known [48]. This testing procedure is performed by applying a pure bending moment to a specimen while simultaneously rotating the specimen. The applied bending moment will create an alternating compressive and tensile stress state at different points in the material. For high temperature testing a rotating-beam reverse-bending machine that is contained inside of an electric furnace is needed. Before any testing begins the specimen must be stabilized at the target test temperature such that there are no temperature gradients present throughout the structure. The alternating reverse loading can be performed at different cyclic rates to analyze the variations in fatigue failure, or the lack there of, and fatigue properties at these specific rates.

5.5 Controlled Aluminum Diffusion Testing

Due to the lack of definitive result there is a need for further aluminum diffusion testing. Investigations similar to Tarasov's and Rubtsov's [27] experimental study can be conducted so that a more controlled procedure can be used to formulate a conclusive study. Tool pins for each of the three materials need to be identically fabricated and used to weld

an aluminum alloy of known composition. Each tool pin will be used to weld a set length of material at a constant rotational speed, plunge force, and feed rate. Tarasov and Rubtov welded 2000 m of the aluminum alloy at 560 rpm, using 2600 kg of plunge force, a feed rate of 500mm/min and were able to observe the presence of aluminum diffusion in the 1.2344X40CrMoV5-1 FSW tool [27]. A similar weld length and welding parameters could be used for the additional aluminum diffusion testing. After welding the specimens can be analyzed using a Carl Zeiss Ultra plus FE-SEM with EDS capabilities. EsB analysis can be conducted to obtain qualitative results at various magnifications and the EDAX software can be used for EDS compositional analysis to obtain quantitative results regarding the presence of aluminum diffusion at the interface between the tool material and the aluminum alloy.

REFERENCES

[1] Thomas, WM; Nicholas, ED; Needham, JC; Murch, MG;Temple-Smith, P;Dawes, CJ.*Friction-stir butt welding*, GB Patent No. 9125978.8, International patent application No. PCT/GB92/02203, (1991)

[2] R. Rai, A. De, H. K. D. H. Bhadeshia, T. DebRoy: 'Review: friction stir welding tools', *Science and Technology of Welding and Joining*,16-4 (2011), 325-342

[3] R. S. Mishra and Z. Y. Ma: 'Friction stir welding and processing', *Mat. Sci. Eng. A*, 2005, 50, (1-2), 1-78

[4] K. Kumar and S. C. Kailas: 'The role of friction stir welding tool on material flow and weld formation', *Mater. Sci. Eng. A*, 2008, A485, (1-2), 367-374

[5] H. Aharifar, D.C. Lin, and R. Kovacevic: 'Numerical and experimental investigation on the loads carried by the tool during friction stir welding'. *J. Mater. Eng. Perform.*, 2009, 18, (4), 339-350

[6] G. Mishuris and A. Plakhov: 'Magnus effect and dynamics of a spinning disc in a rarefied medium', *Arch. Mech.*, 2009, 61, (5), 391-406

[7] C. Chen and R. Kovacevic: 'Thermomechanical Modelling and Force Analysis of Friction Stir Welding by the Finite Element Method', *Proc. ME C.J. Mech. Eng. Sci.*, 2004, 218(5), 509-519

[8] P.A. Colegrove and H. R. Shercliff: '3-Dimensional CFD Modelling of Flow Round a Threaded Friction Stir Welding Tool Profile', *J. Mater. Process. Technol.*, 2005, 169, 320-327

[9] A. Arora, M. Mehta, A. De, and T. DebRoy: 'Load bearing capacity of tool pin during friction stir welding', Unpublished Document, The Pennsylvania State University, PA, USA, 2011

[10] A. Arora, A. De, and T. DebRoy: 'Toward optimum friction stir welding tool shoulder diameter', *Ser Mater*, 2011. 64, 9-12

[11] M. Mehta, A. Arora, A. De, and T. DebRoy: 'Tool geometry for friction stir welding –optimum shoulder diameter', *Metall. Mater. Trans.* A., 2011, 42A, 2716-2722

[12] Q. Li, M. Lovell: 'On the critical interfacial friction of a two-roll CWR process', *J. Mater. Proc. Tech.*, 2005, 160, 245-256

[13] Shi Q: 'Prediction of thermal distortion and thermal fatigue in shot sleeves', *Dissertation*, Ohio State University, Columbus, 2002

[14] E.P. Popov: 'Engineering Mechanics of Solids', 2nd Ed. *Pearson Education*, New Delhi, 2011, Sections 10.9, 11.4, and 13.10

[15] C.D. Sorensen, A.L. Stahl: 'Experimental measurement of load distributions on friction stir weld pin tools', *Metall. Mater. Trans. B*, 2007, 38B, 451-459

[16] P. Biswas, D. A. Kumar, and N. R. Mandal: 'Friction stir welding of aluminum alloy with varying tool geometry and process parameters', *Proc. Insti. Mech. Eng.*, 2011, 641-648

[17] K. Elangovan, V. Balasubramanian, and M. Valiappan: 'Influences of tool pin profile and axial force on the formation of friction stir processing zone in AA6061 aluminum alloy', *Int. J. Adv. Manuf. Technol.*, 2008, 38, 285-295

[18] W.M. Thomas and R.E. Dolby: 'Friction stir welding developments', *Proc. of 6th Inter. Trend in Weld. Res. Conf.*, 2002, 203-211

[19] S. M. Chowdhury, D. L. Chen, S. D. Bhole, and X. Cao: 'Tensile properties of a friction stir welded magnesium alloy: Effect of pin tool thread orientation and weld pitch', *Mater. Sci. Eng. A*, 2010, A527, 6064-6075

[20] G. Buffa, J. Hau, R. Shivpuri, and L. Prantini: 'Design of the friction stir welding tool using the continuum based FEM model', *Mat. Sci. and Eng. A*, 2006, 419, 381-388

[21] K. Elangovan and V. Balasubramanian: 'Influences of tool pin profile and tool shoulder diameter on the formation of friction stir processing zone in AA6061 aluminum alloy', *Mater. Des.*, 2008, 29,362-373

[22] I. Galvao, R. M. Leal, D. M. Rodriues, and A. Loureriro: 'Influence of tool shoulder geometry on properties of friction stir welds in think copper sheets', *Jour. of Mat. Proc. Tech.*, 2012, 213, 129-135

[23] L. Cederqvist, C. D. Sorensen, A. P. Reynolds, and T. ObergL 'Improved process stability during friction stir welding of 5 cm thick copper canisters through shoulder geometry and parameter studies', *Sci. Tech. weld. Join.*, 2009, 14, 178-184

[24] J.E. Gould and Z. Feng: 'Heat flow model for friction stir welding of aluminum alloys', *Jour. of Mat. Proc. And Man. Sci,* 1998

[25] M. Z. Ahmed et al: 'Through thickness crystallographic texture of stationary shoulder friction stir welded aluminum', *Scripta Mat.,* 2011*, 64 , 45-48*

[26] R. A. Prado, L. E. Murr, D. J. Shindo, K. F. Soto: 'Tool wear in the friction-stir welding of aluminum alloy 6061+20% Al_2O_3: a preliminary study', *Scripta Mat.,* 2001, 45, 75-80

[27] S. Yu. Tarasov, V. E. Rubtsov, E. A. Kolubaev: 'A proposed diffusion-controlled wear mechanism of alloy steel friction stir welding (FSW) tools used on an aluminum alloy', *Wear*, 2014, 318, 130-134

[28] D. A. Rigney: 'Transfer, mixing and associated chemical and mechanical processes during the sliding of ductile materials', *Wear*, 2000, 245, 1-9

[29] Alro, ' Tool Steels', *Alro, Tool Steel H13*

[30] G. F. Voort, S. R. Lampman, B. R. Sanders, 'ASM Handbook Volume 9: Metallography and Microstructures', *American Society of Metals,* New York, 2004, 258-259

[31] Matweb, 'AISI Type H13 Hot Work Tool Steel', *Matweb*

[32] T. Lyman, H. E. Boyer, W. J. Carnes, and P. M. Unterweiser, 'Metals Handbook: Atlas of Microstructues of Industrial Alloys', *American Society of Metals,* Ohio, 1972, 8,7, 116

[33] Thyssen Krupp: 'TSP1: Acier semi-rapide élaboré par métallurgie des poudres', *Thyssen Krupp,* Germany

[34] Thyssen Krupp Austria: 'Werkstoffblatt: TSP1', *Thyssen Krupp,* Germany

[35] Carrs Tool Steel Technologies: ' Extreme High Performance Powder Metallury Tool Steels', *Carrs Tool Steel Technologies*, UK

[36] Latrobe Steel: ' MP159 Alloy', *Latrobe Specialty Steel Company,* Pennsylvania, 2007

[37] J. R. Davis: 'Nickel, Cobalt, and Their Alloys', *ASM International*, 2000, 369

[38] R. S. Mishra and M. W. Mohoney: 'Friction Stir Welding and Processing', *ASM International,* 2007, 9-10

[39] K. B. Small, D. A. Englehart, and T. A Christman, 'Guide to Etching Specialty Alloys', *Adv. Mat. & Proc.,* 2008, 32-37

[40] ASTM, "E384-99: A Standard Test Method for Microindentation Hardness of Materials", ASTM, Philadelphia, 1984.

[41] S. P. Canning, 'Annual Book of ASTM Standards: Section 3: Metals Test Methods and Analytical Procedures', *ASTM International,* 2007,3.01, 199-225

[42] Harrison Electropolishing, 'Ra & RMS: Calculating Surface Roughness', *Harrison Electopolishing,* Houston, 2012

[43] L. Xiao, 'MatLAB Code: Linear Least Square Surface Fitting', *Univ. South Carolina,* 2015

[44] G. F. Vander Voort, 'Understanding and Measuring Decarburization', *Adv. Mat. & Proc,* 2015, Feb. 22-27

[45] K. Mills, 'ASM Handbook: Fractography', *ASM International,* 1987, 12, 12-13

[46] F. M. Haggaag, 'Small Specimen Test Techniques Applied to Nuclear Reactor Vessel', *ASTM,* 1993, 1204, 27-30

[47] J. D. Verhoeven, 'Steel Metallurgy for the Non-Metallurgist', *ASM International,* 2007, 99-106

[48] J. G. Kaufman, 'Properties of Aluminum Alloys: Fatigue Data and the Effects of Temerature, Product From, and Processing', *ASM International,* 2008, 5-8

[49] D. C. Bell and N. Erdman, 'Low Voltage Electron Microscopy: Principles and Applications', *John Wiley & Son,* 2013

APPENDIX A: IZOD SPECIMEN DIMENSIONS

Table A.1: H13 Izod Specimen Dimensions

H13 Specimen Dimensions							
Specimen #	**A**	**B**	**C**	**D**	**E**	**F**	**R**
1	57.95	13.09	31.06	2.39	9.23	2.09	0.45
2	58.00	13.10	30.87	2.40	9.52	2.09	0.41
3	57.92	13.10	30.99	2.32	9.61	2.08	0.47
4	58.12	13.11	30.86	2.40	9.51	2.06	0.50
5	58.07	13.17	30.89	2.40	9.55	2.02	0.50
6	58.06	13.08	30.88	2.41	10.08	2.16	0.50
7	58.02	13.10	30.89	2.37	10.86	2.33	0.40
8	58.06	13.10	30.86	2.38	9.91	2.06	0.47
9	58.07	13.12	30.90	2.39	9.58	2.17	0.46
10	58.07	13.11	30.89	2.31	9.25	2.13	0.42
11	58.08	13.10	30.86	2.43	10.05	2.00	0.43
12	57.98	13.12	30.93	2.43	8.98	2.03	0.43
13	58.00	13.09	30.95	2.45	9.55	2.10	0.43
14	58.10	13.15	30.88	2.42	9.78	2.07	0.45
15	58.02	13.09	30.83	2.37	9.63	2.04	0.43
16	57.89	13.11	30.93	2.35	9.82	2.05	0.51
17	58.04	13.11	30.88	2.33	9.53	2.08	0.47
18	58.13	13.09	30.85	2.33	9.13	2.17	0.46
19	57.90	13.10	30.97	2.39	8.98	2.02	0.46
20	57.93	13.11	30.94	2.38	9.53	2.09	0.50
21	58.03	13.13	31.10	2.40	9.68	2.08	0.45
22	58.15	13.13	30.86	2.40	9.13	2.10	0.48
23	57.95	13.11	30.95	2.35	9.54	2.05	0.45
24	57.92	13.14	30.92	2.42	8.92	2.09	0.48
25	58.09	13.16	30.87	2.35	9.95	2.03	0.49
Mean	58.02	13.11	30.91	2.38	9.57	2.09	0.46
Median	58.03	13.11	30.89	2.39	9.55	2.08	0.46
Std. Dev. P	0.0739	0.0224	0.0635	0.0361	0.4134	0.0664	0.0300
Std. Dev S	0.0754	0.0228	0.0648	0.0368	0.4220	0.0678	0.0306

Table A.2: MP159 Izod Specimen Dimensions

MP159 Specimen Dimensions							
Specimen #	**A**	**B**	**C**	**D**	**E**	**F**	**R**
1	57.90	13.51	30.79	2.31	8.73	2.01	0.54
2	57.94	13.50	30.82	2.64	8.78	2.12	0.50
3	58.00	13.49	30.78	2.52	8.08	2.15	0.56
4	58.00	13.51	30.80	2.52	8.71	2.15	0.46
5	58.02	13.55	30.80	2.54	8.69	1.94	0.58
6	57.82	13.51	30.80	2.45	8.80	2.09	0.47
7	57.99	13.52	30.78	2.52	8.78	2.00	0.44
8	57.90	13.49	30.82	2.48	8.80	2.05	0.47
9	58.04	13.50	30.78	2.52	8.07	2.01	0.48
10	57.84	13.50	30.78	2.54	8.80	2.00	0.43
11	57.93	13.52	30.82	2.58	8.78	2.00	0.48
12	57.97	13.56	30.81	2.44	7.97	2.11	0.47
13	57.94	13.53	30.80	2.40	8.79	2.23	0.52
14	57.95	13.50	30.71	2.53	8.03	2.01	0.52
15	58.01	13.56	30.77	2.52	8.57	2.00	0.45
16	57.90	13.40	30.81	2.54	7.95	2.01	0.43
17	57.95	13.50	30.76	2.63	8.65	2.09	0.45
18	57.96	13.50	30.81	2.61	8.04	2.12	0.40
19	57.98	13.51	30.77	2.52	8.88	2.06	0.48
20	57.97	13.50	30.82	2.57	8.77	2.08	0.43
21	58.02	13.51	30.83	2.52	8.73	2.06	0.54
22	58.05	13.51	30.81	2.54	8.66	2.01	0.51
23	58.02	13.52	30.83	2.33	8.75	2.20	0.49
24	58.01	13.53	30.83	2.40	7.99	2.22	0.55
25	58.06	13.52	30.80	2.57	8.40	2.07	0.51
Mean	57.97	13.51	30.80	2.51	8.53	2.07	0.48
Median	57.97	13.51	30.80	2.52	8.71	2.06	0.48
Std. Dev. P	0.0602	0.0293	0.0266	0.0810	0.3308	0.0749	0.0453
Std. Dev S	0.0614	0.0299	0.0272	0.0827	0.3376	0.0765	0.0462

Table A.3: TSP1 Izod Specimen Dimensions

TSP1 Specimen Dimensions							
Specimen #	**A**	**B**	**C**	**D**	**E**	**F**	**R**
1	57.98	16.25	31.22	2.83	8.67	1.93	0.53
2	57.92	16.26	31.19	2.83	8.86	2.13	0.52
3	57.91	16.28	31.21	2.96	8.43	2.00	0.46
4	57.94	16.23	31.18	2.83	8.68	2.04	0.54
5	57.96	16.26	31.16	2.81	8.51	1.99	0.52
6	57.90	16.26	31.19	2.90	8.55	2.03	0.51
7	58.03	16.12	30.93	2.94	9.55	2.04	0.45
8	58.01	16.08	30.96	2.93	9.62	2.03	0.50
9	57.97	16.09	30.95	2.90	9.69	2.02	0.52
10	58.00	16.13	30.89	2.87	9.67	2.04	0.51
11	58.05	16.10	30.97	2.90	9.50	2.00	0.52
12	58.07	16.10	30.96	2.82	9.60	2.06	0.45
13	58.03	16.10	31.01	2.84	9.49	2.06	0.47
14	58.07	16.10	30.96	2.76	9.68	2.06	0.56
15	58.09	16.11	30.98	2.75	9.74	2.08	0.46
Mean	58.00	16.16	31.05	2.86	9.22	2.03	0.50
Median	58.00	16.12	30.98	2.84	9.50	2.04	0.51
Std. Dev. P	0.0594	0.0765	0.1183	0.0608	0.5014	0.0438	0.0336
Std. Dev S	0.0615	0.0792	0.1224	0.0629	0.5190	0.0453	0.0348

APPENDIX B: MATHLAB CODE FOR SURFACE FITTING

B-1: Mathlab Code for Surface Fitting of Roughness Data

QIUHE CODE

```
function he=qiuhe(x,p,y,q,z)

m=length(x);
if (nargin<4 )&(m~=length(y))
    error('error check check!');
end
if nargin==4
    z=ones(m,1);
end

he=0;
for i=1:m
    he=he+x(i)^p * y(i)^q*z(i);
end
```

QUOTIENT CODE

```
function sh=quotient(x,y)

sh=(x-mod(x,y))/y;

end
```

LEFT MATRIX CODE

```
function U=leftmatrix(x,p,y,q)

m=length(x);
if (nargin~=4) & (m~=length(y))
    error('error check check!');
end

U_length=p*q;
U=zeros(U_length,U_length);
for i=1 : p*q
    for j= 1 : p*q
        x_z=quotient(j-1,q)+quotient(i-1,q);
        y_z=mod(j-1,q)+mod(i-1,q);
        U(i,j)=qiuhe(x,x_z,y,y_z);
    end
end
```

RIGHT MATRIX CODE

```
function V=rightmatrix(x,p,y,q,z)

if nargin~=5
    error('error check check! rightmatrix')
end

V=zeros(p*q,1);
for i=1 : p*q
    x_z=quotient(i-1,q);
    y_z=mod(i-1,q);
    V(i,1)=qiuhe(x,x_z,y,y_z,z);
end
```

SECOND ORDER FIT CODE

```
function
[Leastq,A,bp,bq,XI,YI,ZI]=secondorderfit(x,z,f,x1,x2,y1,y2,z1,z2)
% Leastq is the least R^2 among p q from 3 to 3
% A is the matrix of fitting parameter
% bp is best p from 3 to 3
% bq is best q from 3 to 3
% XI YI are coordinates of fit position
% ZI is value in fit position
%
% x z are input coordinates
% f are value at input coordinate
% x1 x2 are up bottom range of x
% y1 y2 are up bottom range of z
% z1 z2 are up bottom range of fit value when plot surface

Leastq=inf;
for p=3: 3
   for q =3 : 3
    clear aa;
    U=leftmatrix(x,p,z,q);
    V=rightmatrix(x,p,z,q,f);
    a_n=U\V;
    for i=1 : length(a_n)
        ii=quotient(i-1,q)+1;
        jj=mod(i-1,q)+1;
        aa(ii,jj)=a_n(i,1);
    end
    Rsq=0;
    for i= 1:length(f)
        clear xl yr;
        xl(1)=1;yr(1)=1;
        for kk=0:p-1
            xl(kk+1)=x(i)^kk;
        end
        for kk=0:q-1
            yr(kk+1)=z(i)^kk;
        end
        Rsq=Rsq+(xl*aa*yr'-f(i))^2;
```

```
    end
    Lq(p,q)=Rsq;
    if Rsq<Leastq
        Leastq=Rsq;
        A=aa;bp=p;bq=q;
    end
   end
end
Leastq;
A;
order(1)=bp;order(2)=bq;
order;


m=300;n=800; % got 100*100 points in fitting area
[XI,YI]=meshgrid(linspace(x1,x2,m),linspace(y1,y2,n));
xx=reshape(XI,m*n,1);
yy=reshape(YI,m*n,1);

tt=zeros(m*n,1);
xy=zeros(m*n,1);
xt=zeros(m*n,1);
yt=zeros(m*n,1);
%tt=0;
[p,q]=size(A);
for i=1 :
    for j=1 :
    xt=xx.^(i-1);
        yt=yy.^(j-1);
        xy=xt.*yt;
        tt=tt+A(i,j).*xy;
    end
end

ZI=reshape(tt,n,m);
surf(XI,YI,ZI),axis([x1 x2 y1 y2 z1 z2])
```

SURFACE FIT CODE

```
clear

%%%%%%%% Step 1 input fitting coordinate value [Xi Zi] %%%%%%%%

Xi=0:0.417:665.532;
Yi=0:0.417:498.732;


%%%%%%%% Step 2 input value to be fit [t rad radius] %%%%%%%%
filename = 'FILENAME.csv';
sheet = 1;
x1Range = 'A1:BIK1197';
Z = xlsread(filename,sheet,x1Range);
[X,Y]=meshgrid(Xi,Yi);
% surf(X,Y,Z);         %Draw input figures for entire original t, rad
and radius.
```

```
% % colormap(jet);
% % surfc(X,Y,Z);
% % color hsv
% % colorbar

%%%%%%%% Step 3 Reshape matrix to N*1 %%%%%%%%

N=numel(X);
Xr=reshape(X,N,1);
Yr=reshape(Y,N,1);
Zr=reshape(Z,N,1);

%%%%%%%% Step 4        surface fitting            %%%%%%%%
%%%%%%%% try from 0 to p-1 order function for X Z %%%%%%%%

x1=min(Xr);x2=max(Xr);
y1=min(Yr);y2=max(Yr);
z1=min(Zr);z2=max(Zr);
[Rsqa,aa,bpa,bqa,XI1,YI1,ZI1]=secondorderfit(Xr,Yr,Zr,x1,x2,y1,y2,z1,z2
);
QA=[Rsqa,bpa-1,bqa-1]; %R, order of x, order of y
```

APPENDIX C: SEM IZOD FRACTURE SURFACE IMAGES

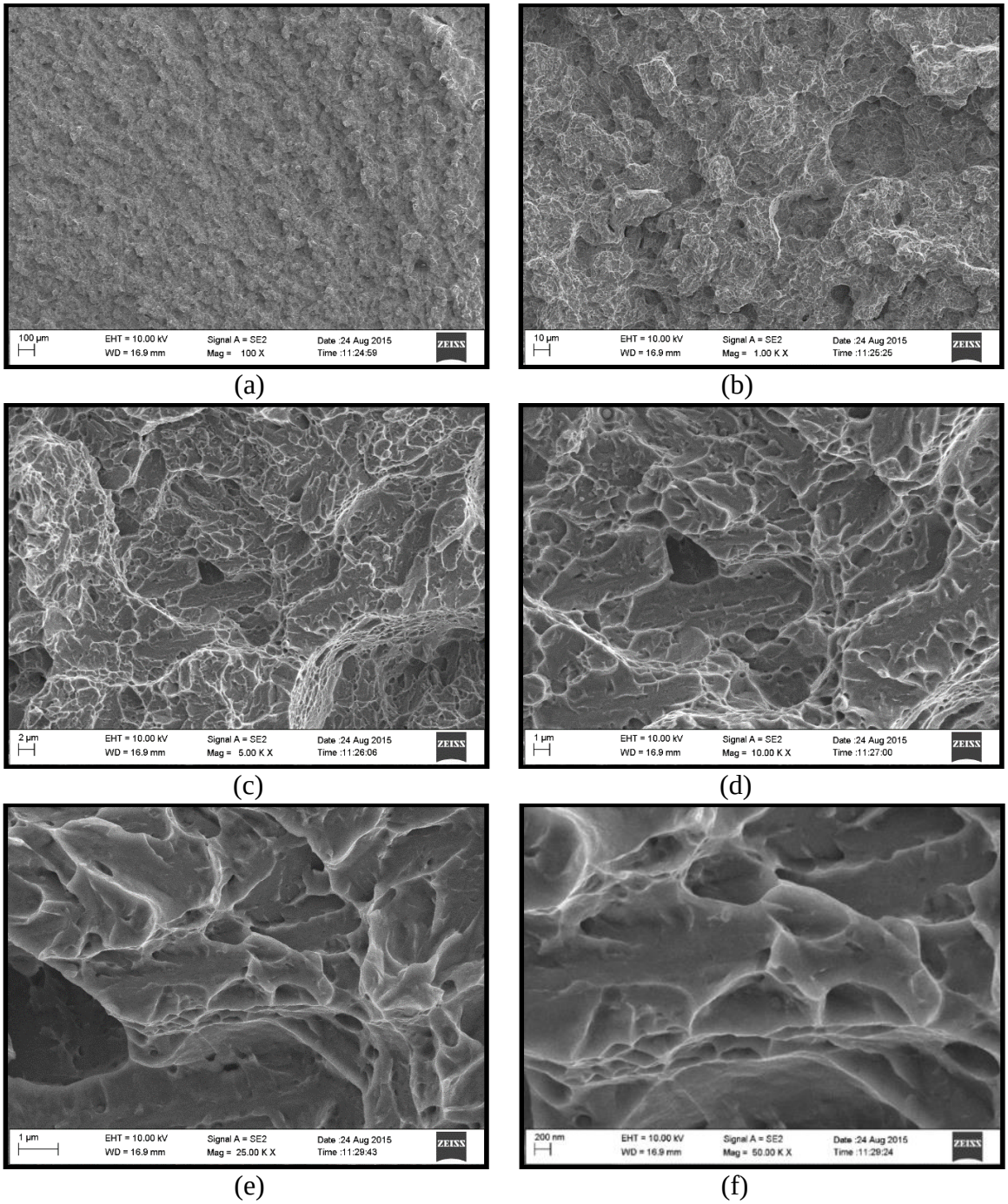

Fig. C.1 Initial H13 SEM Fracture Surface Analysis 100x - 50Kx
Nominal Energy to Failure: 265,683 J/m^2

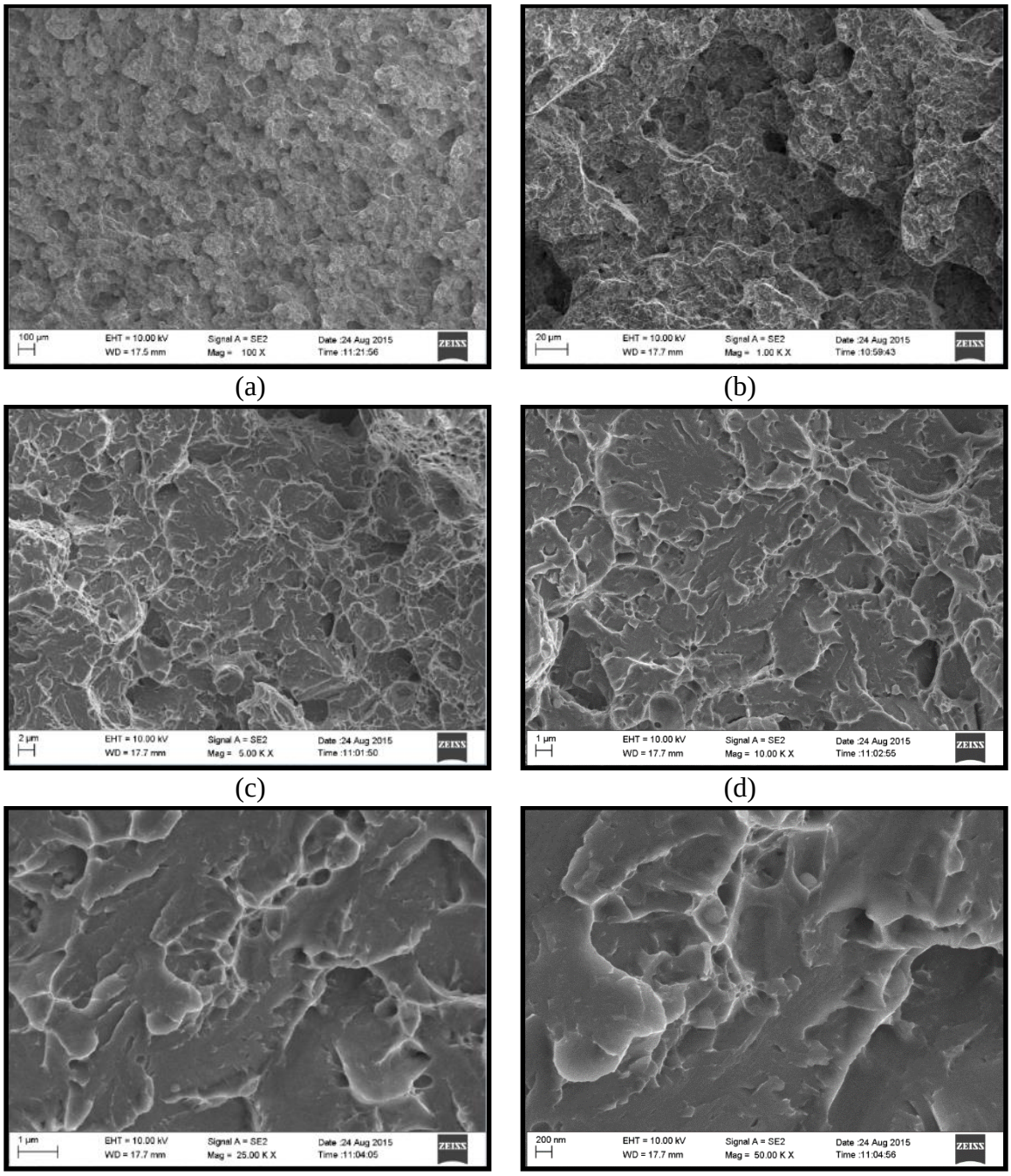

Fig. C.2 High Impact Energy H13 SEM Fracture Surface Analysis 100x -50Kx
Nominal Energy to Failure: 377,979 J/m^2

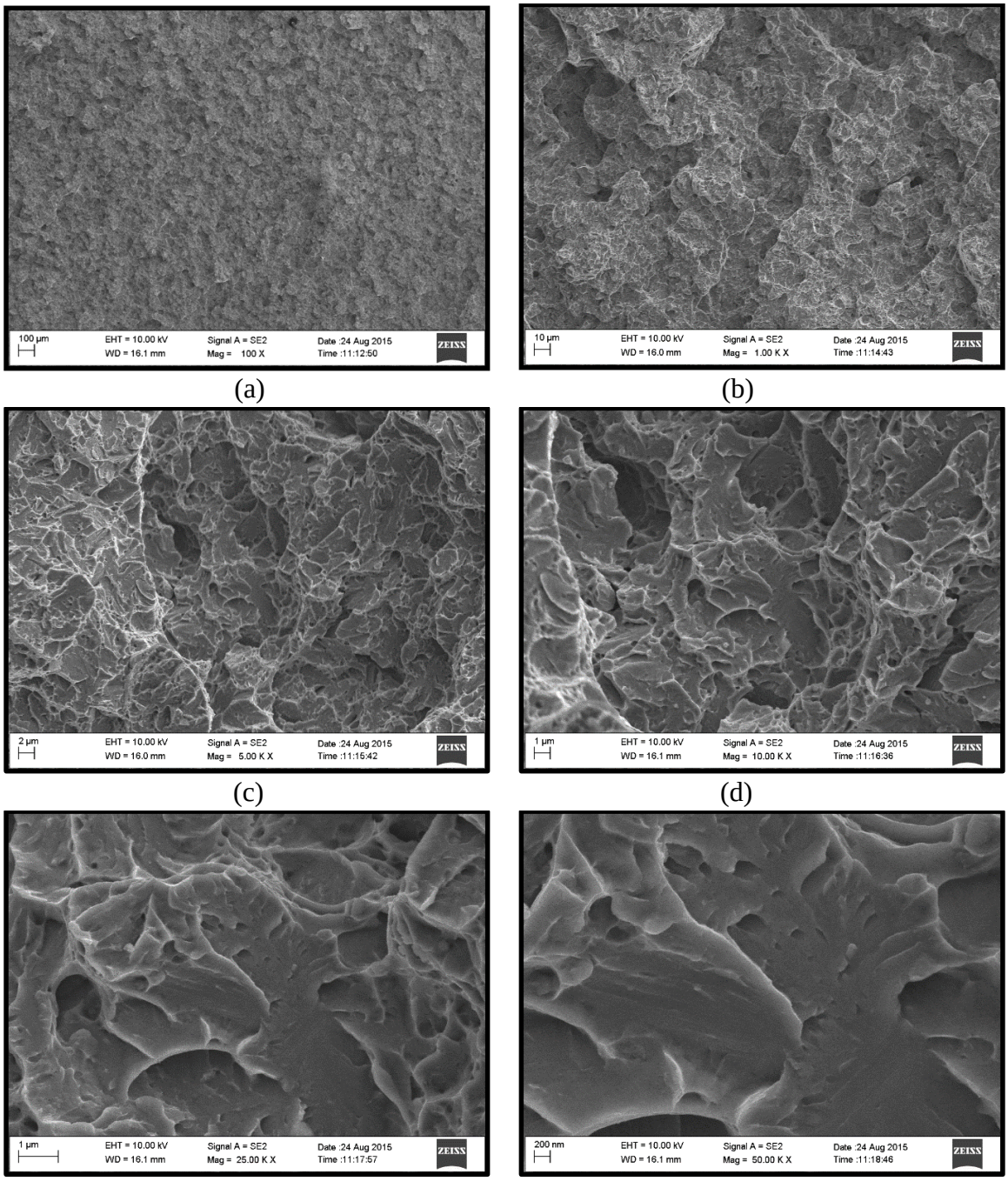

Fig. C.3 Low Impact Energy H13 SEM Fracture Surface Analysis 100x - 50Kx
Nominal Energy to Failure: 123,885 J/m^2

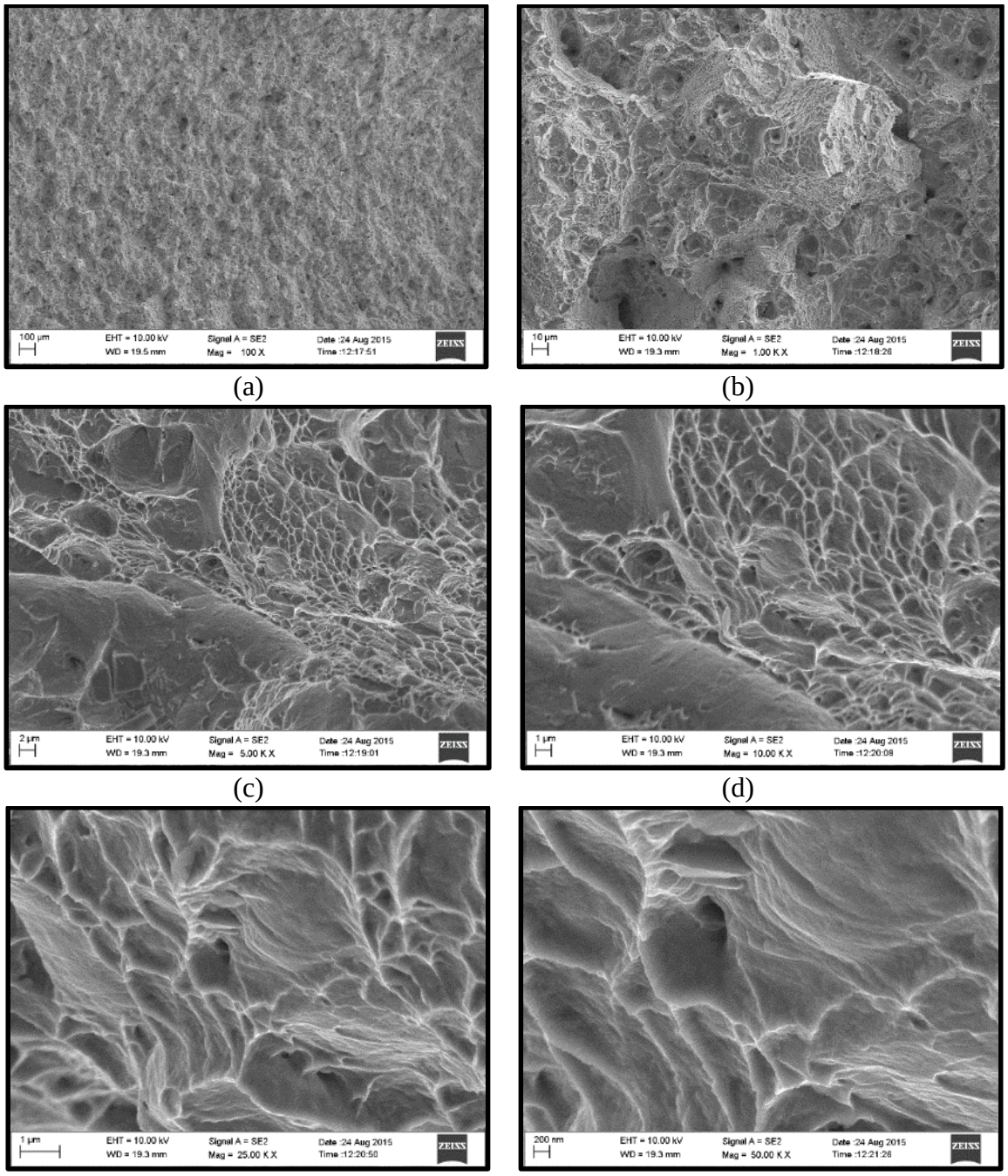

Fig. C.4 Initial MP159 SEM Fracture Surface Analysis 100x – 50Kx
Nominal Energy to Failure: 414,096 J/m^2

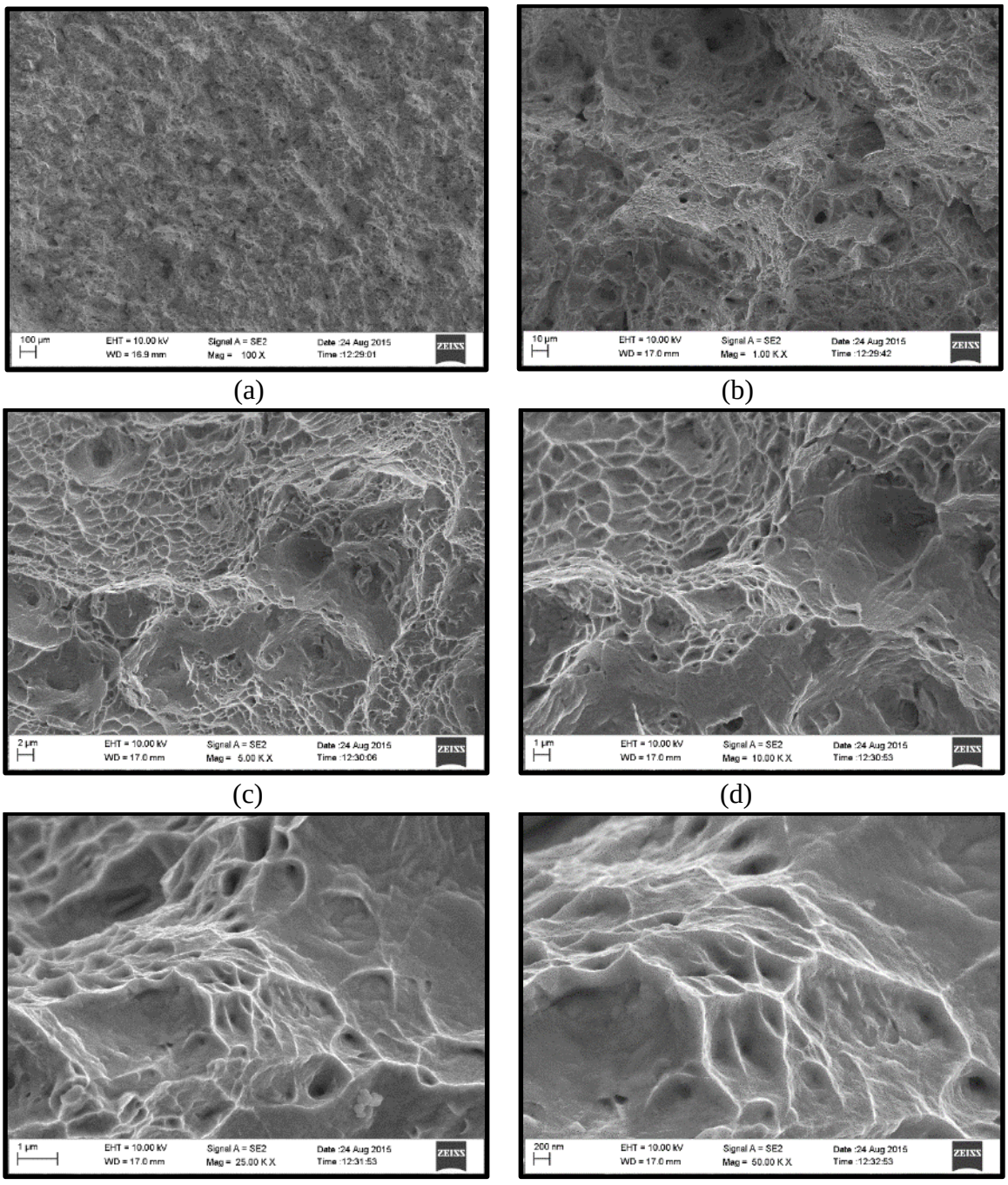

Fig. C.5 Low Impact Energy MP159 SEM Fracture Surface Analysis 100x -50Kx
Nominal Energy to Failure: 278,183 J/m^2

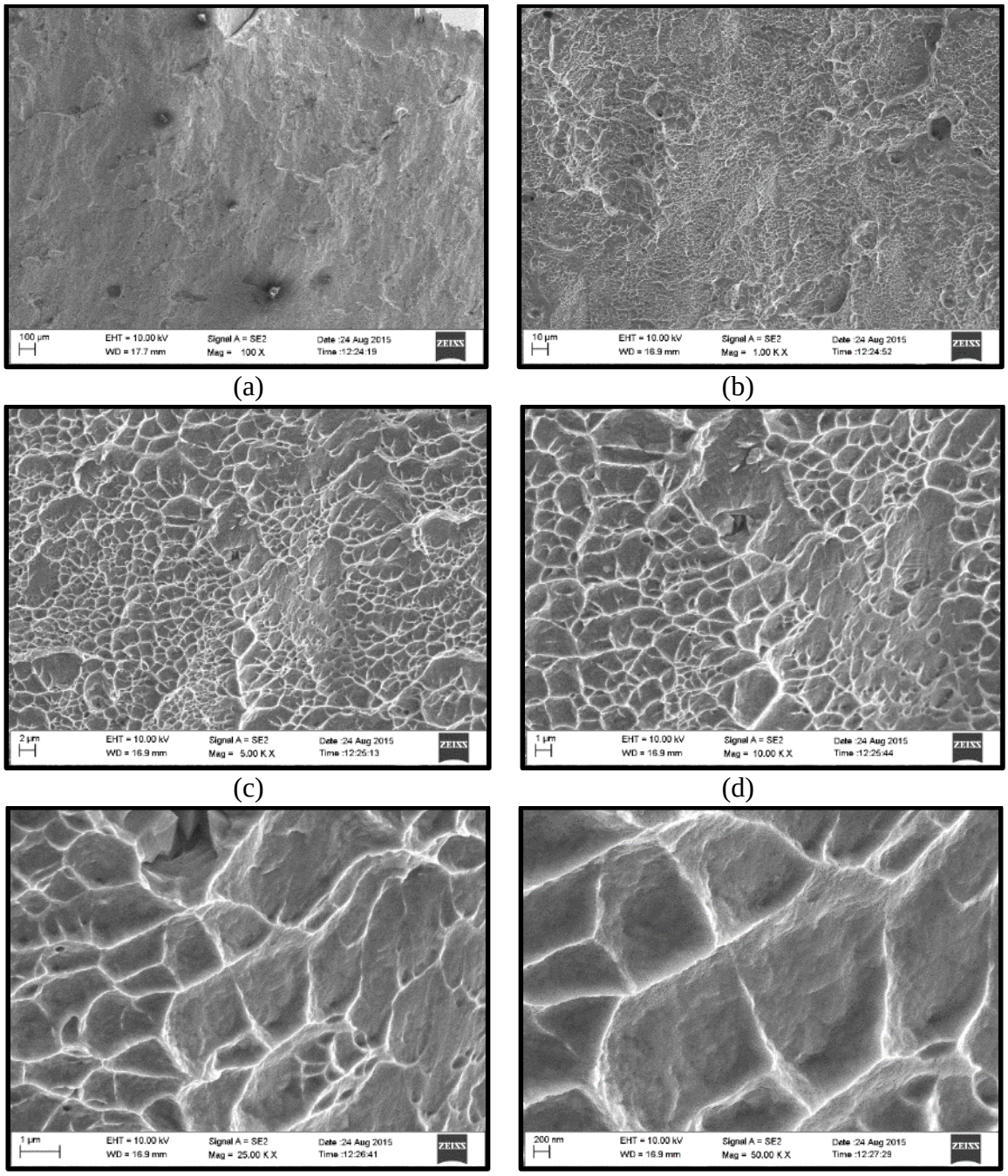

Fig. C.6 Initial MP159 Shear Lip SEM Fracture Surface Analysis 100x - 50Kx
Nominal Energy to Failure: 414,096 J/m^2

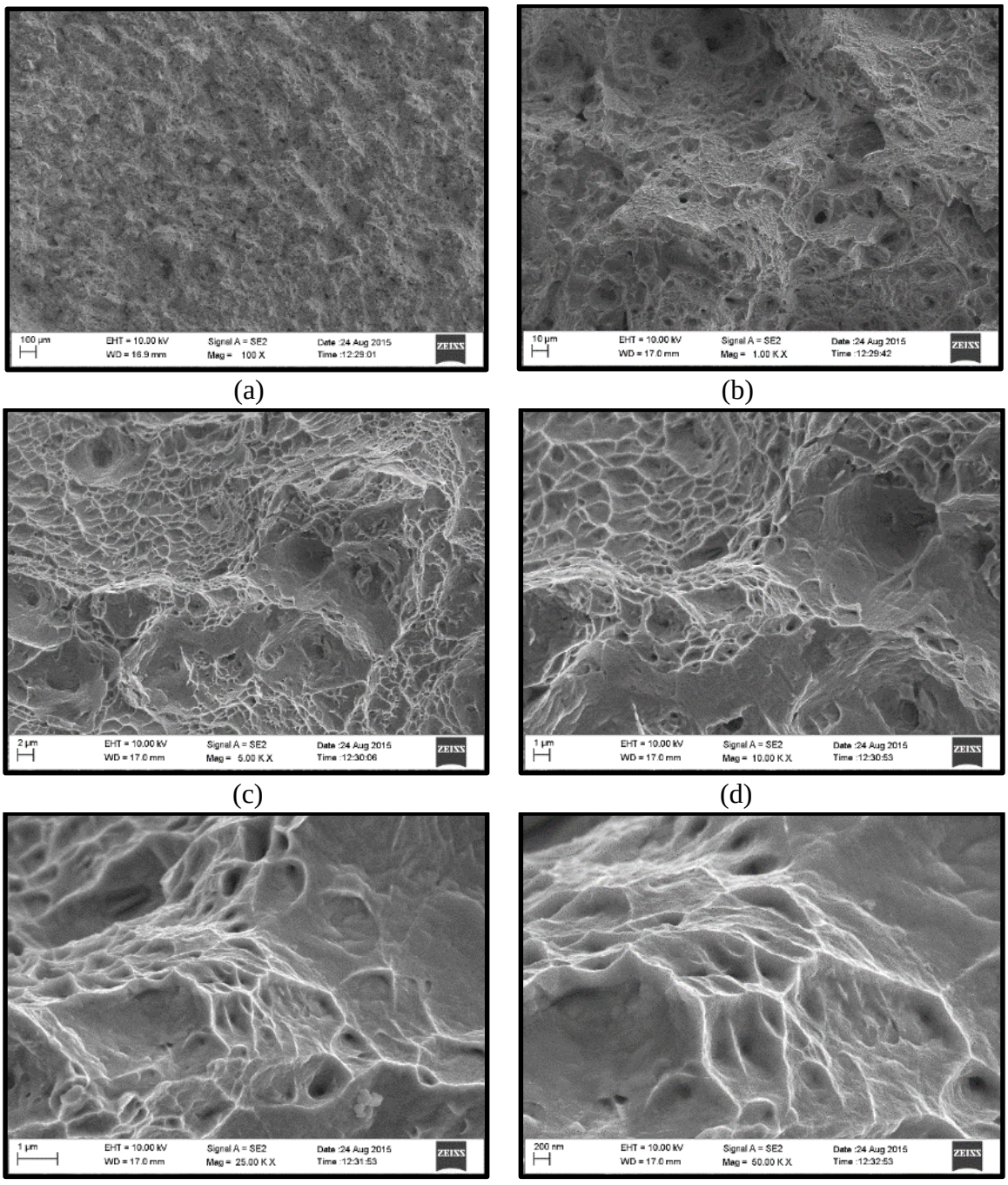

Fig. C.7 Low Impact Energy MP159 Shear Lip SEM Fracture Surface Analysis
Nominal Energy to Failure: 278,183 J/m^2

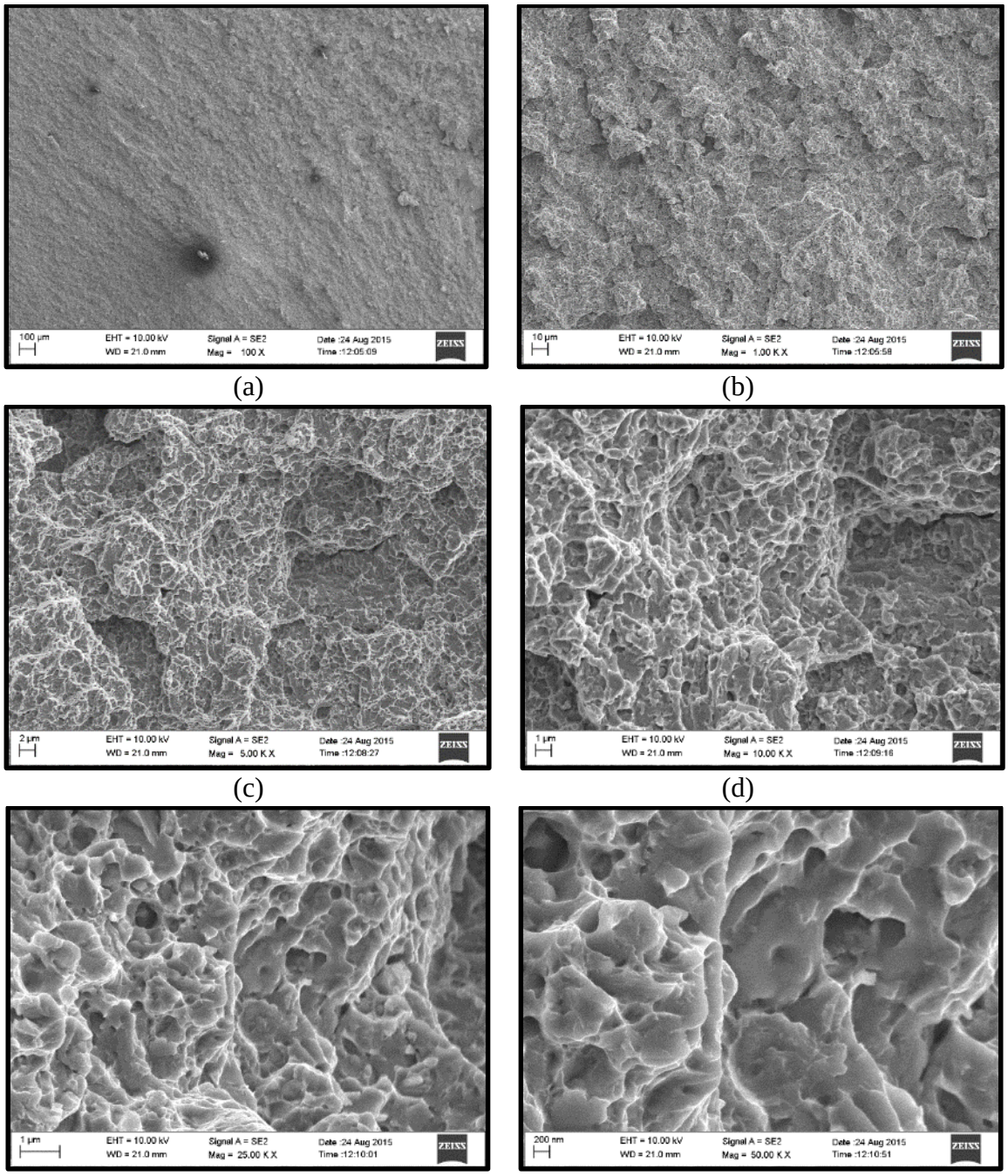

Fig. C.8 Initial TSP1 SEM Fracture Surface Analysis 100x - 50Kx
Nominal Energy to Failure: 49,405 J/m^2

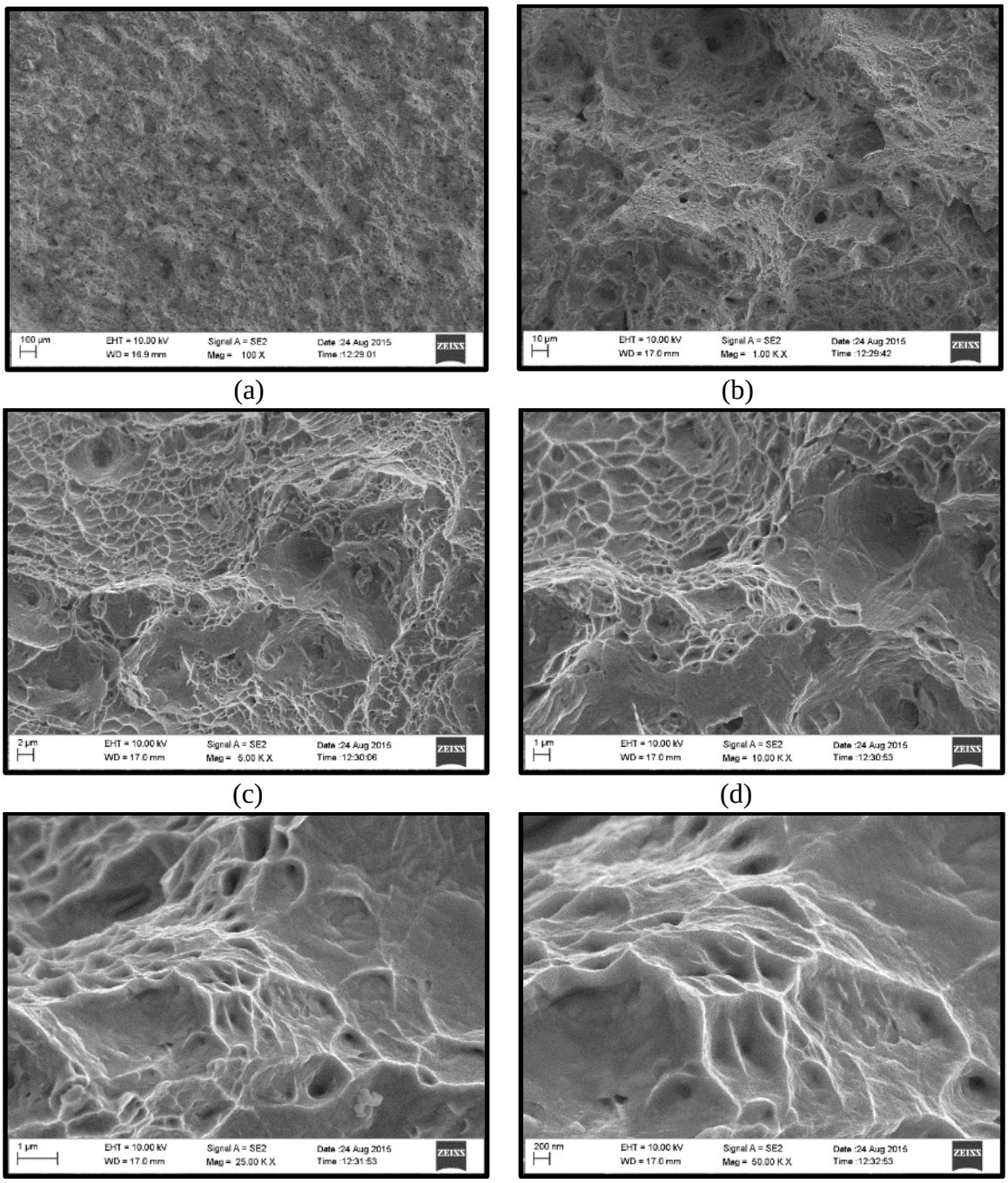

Fig. C.9 Low Impact Energy TSP1 SEM Fracture Surface Analysis
Nominal Energy to Failure: 22,578 J/m^2

APPENDIX D: SEM ALUMINUM DIFFUSION EXPERIMENT 2 SE2 IMAGES

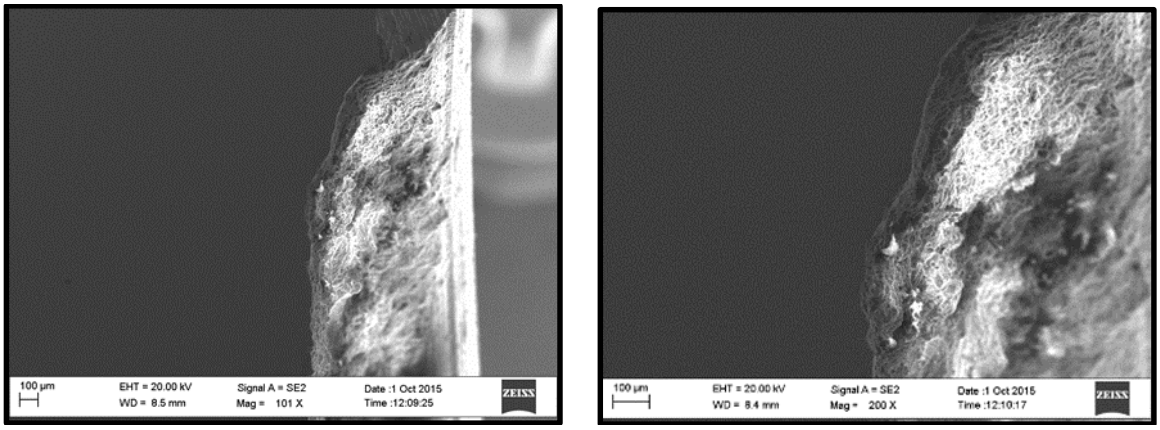

(a) (b)

Fig. D.1 Initial H13 SEM SE2 Tool Shoulder Images at 100x (a) and 250x (b)

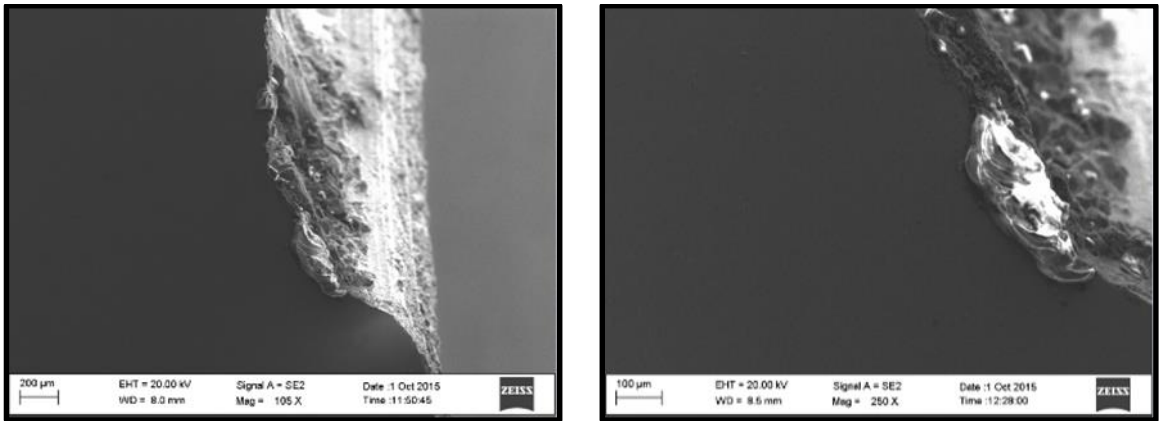

(a) (b)

Fig. D.2 525 °C 200 hours H13 SEM SE2 Tool Shoulder Images at 100x (a) and 250x (b)

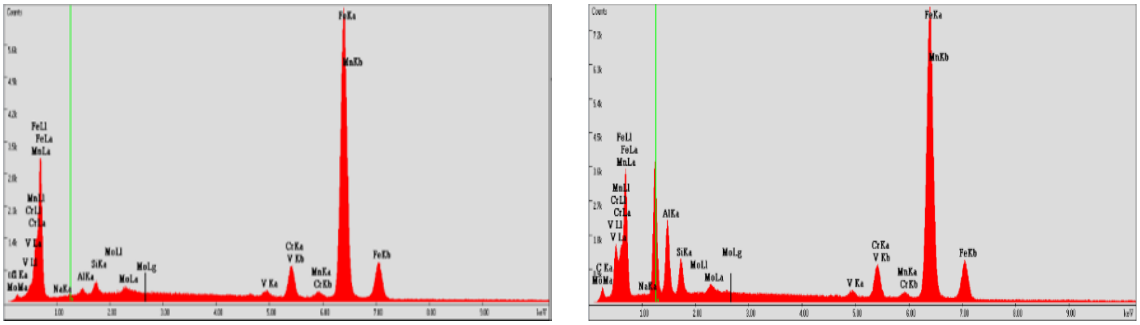

(a) (b)

Fig. D.3 Initial H13 (a) & 525 °C 200 hour H13 (b) EDS Spectrum

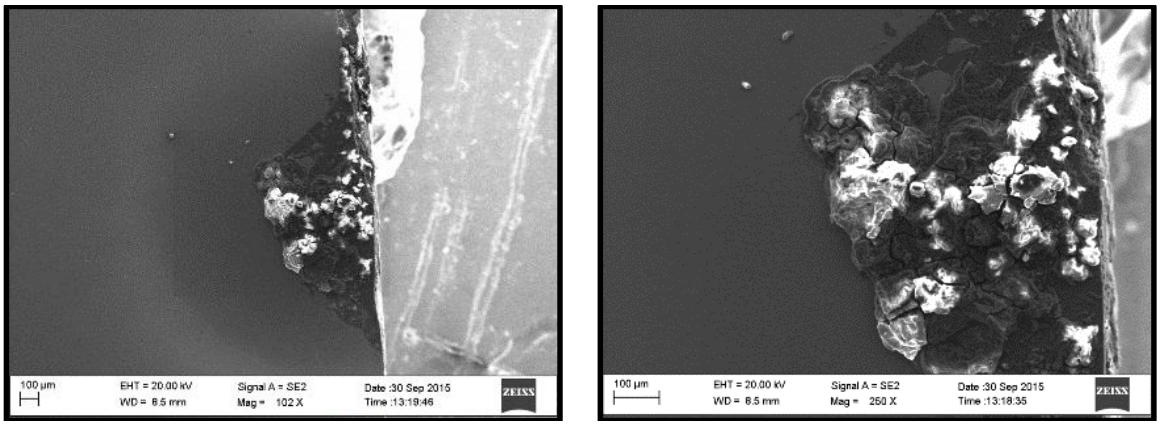

(a) (b)

Fig. D.4 Initial TSP1 SEM SE2 Tool Pin Images at 100x (a) and 250x (b)

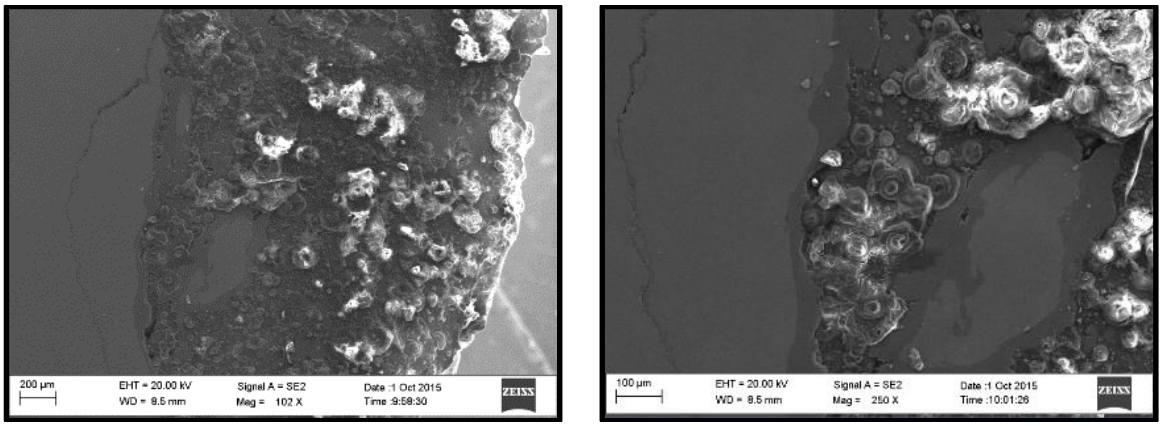

(a) (b)

Fig. D.5 525 °C 200 hours TSP1 SEM SE2 Tool Pin Images at 100x (a) and 250x (b)

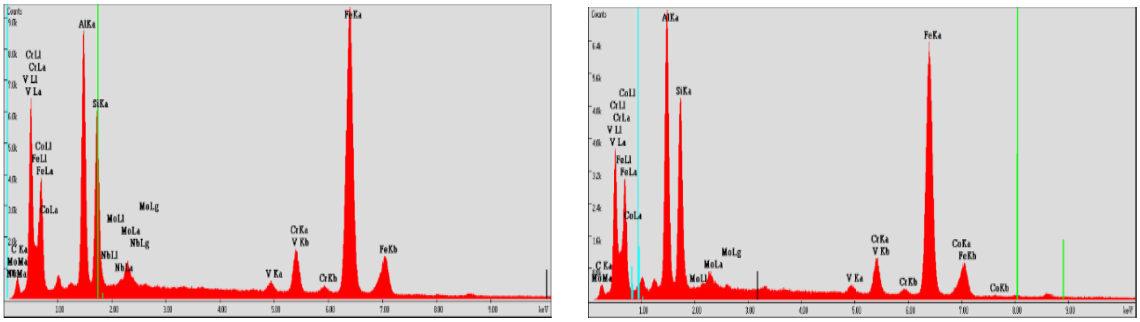

(a) (b)

Fig. D.6 Initial TSP1 (a) & 525 °C 200 hour TSP1 (b) EDS Spectrum

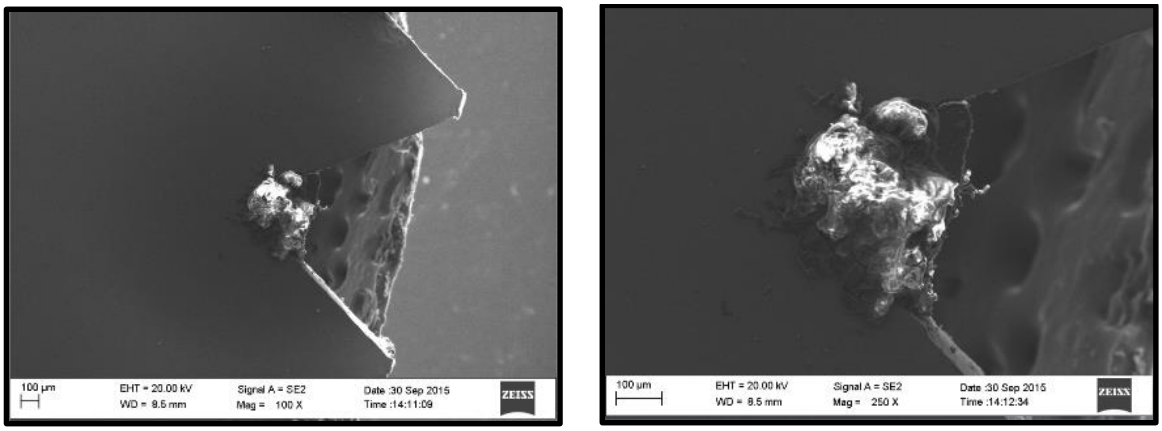

(a) (b)

Fig. D.7 Initial MP159-1 SEM SE2 Tool Pin Images at 100x (a) and 250x (b)

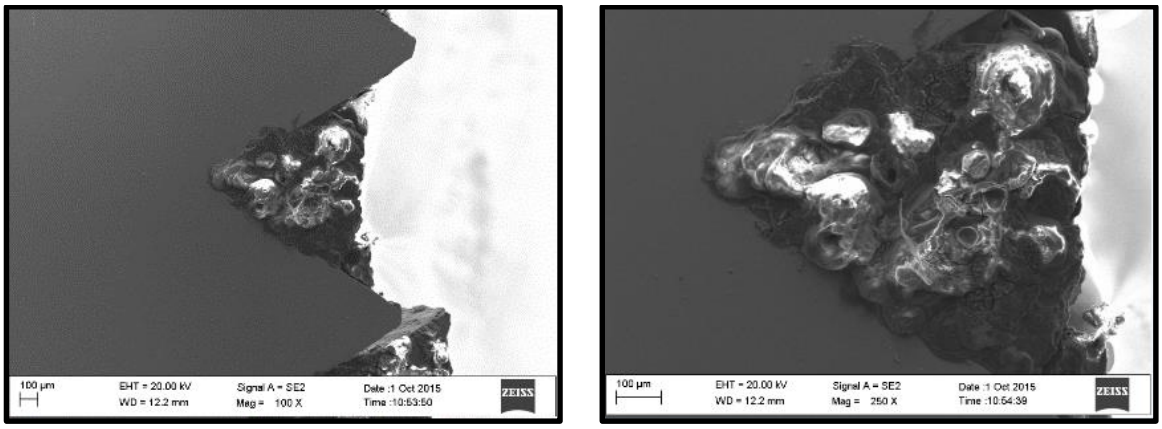

(a) (b)

Fig. D.8 525 °C 200 hours MP159-1 SEM SE2 Tool Pin Images at 100x (a) and 250x (b)

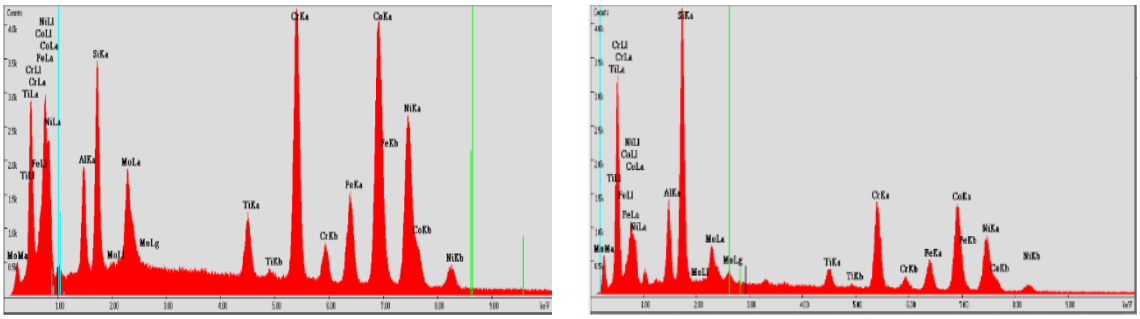

(a) (b)

Fig. D.9 Initial MP159-1 (a) & 525°C 200 hour MP159-1 (b) EDS Spectrum

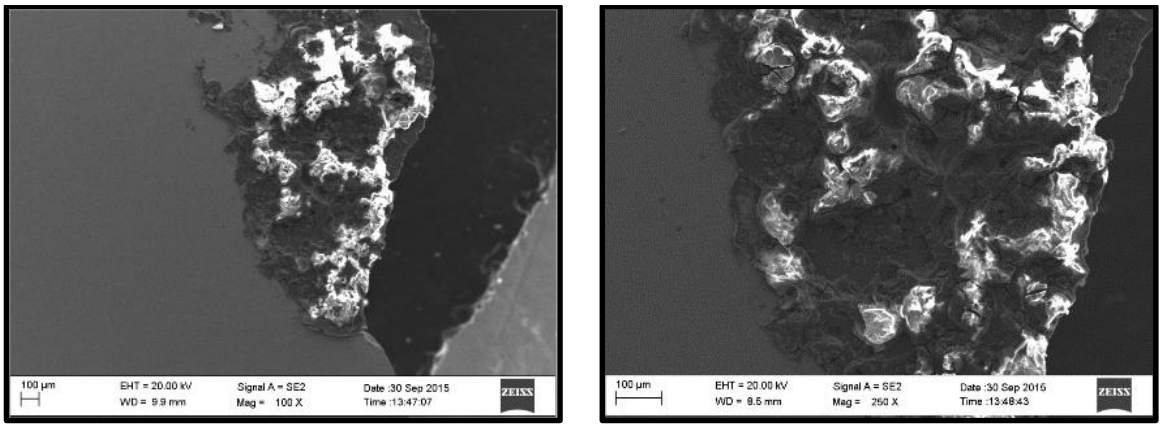

(a) (b)

Fig. D.10 Initial MP159-2 SEM SE2 Tool Pin Images at 100x (a) and 250x (b)

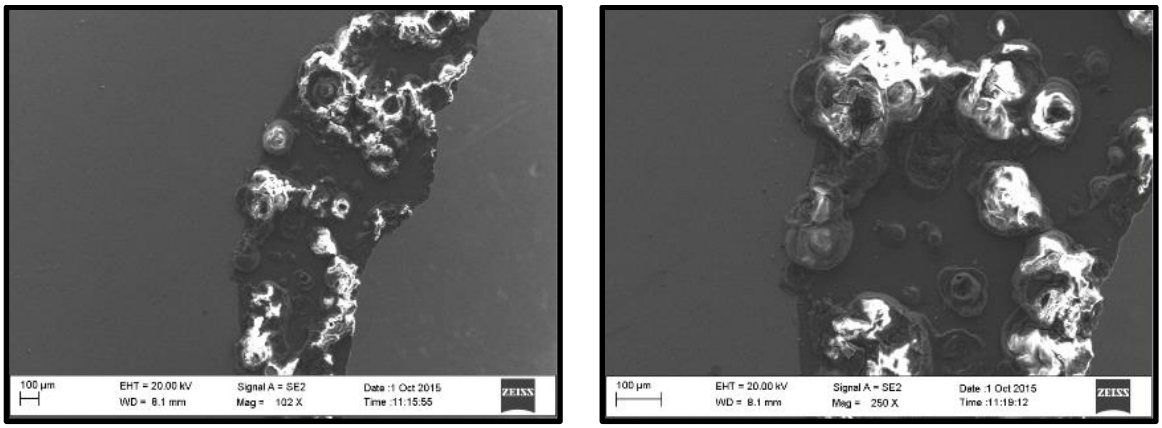

(a) (b)

Fig. D.11 525 °C 200 hour MP159-2 SEM SE2 Tool Pin Images at 100x (a) and 250x (b)

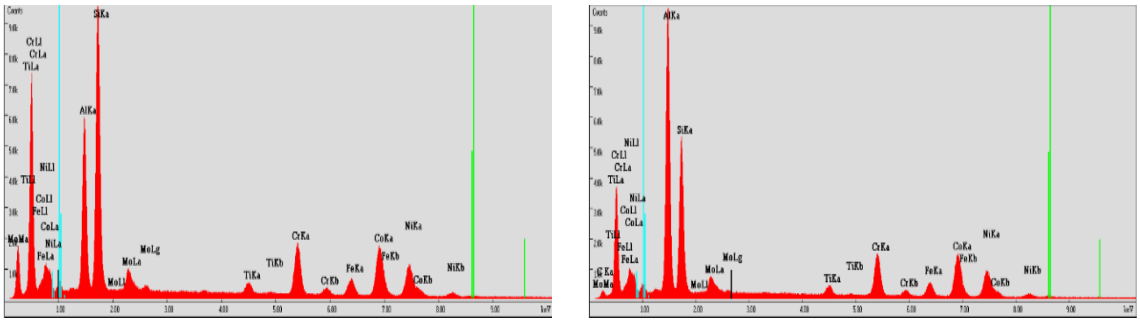

(a) (b)

Fig. D.12 Initial MP159-2 (a) & 525°C 200 hour MP159-2 (b) EDS Spectrum

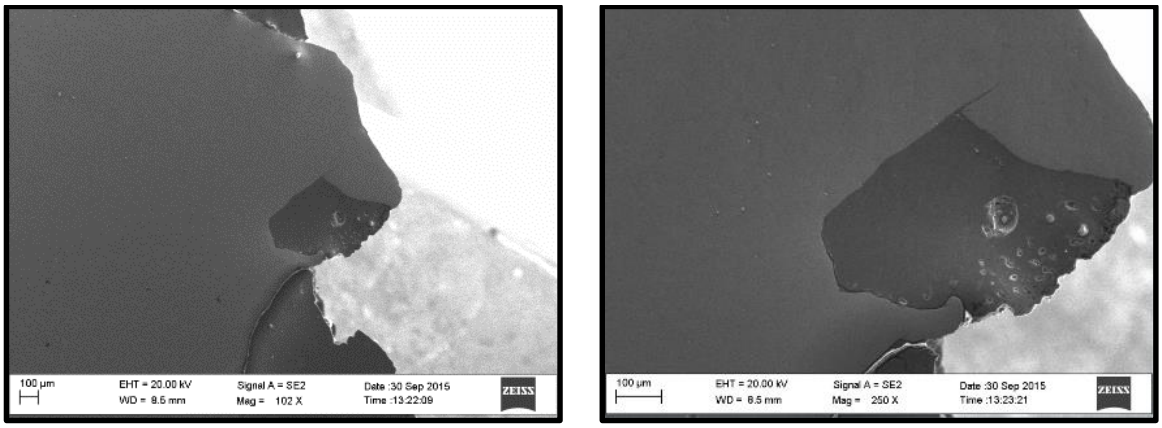

(a) (b)

Fig. D.13 Initial MP159-3 SEM SE2 Tool Pin Images at 100x (a) and 250x (b)

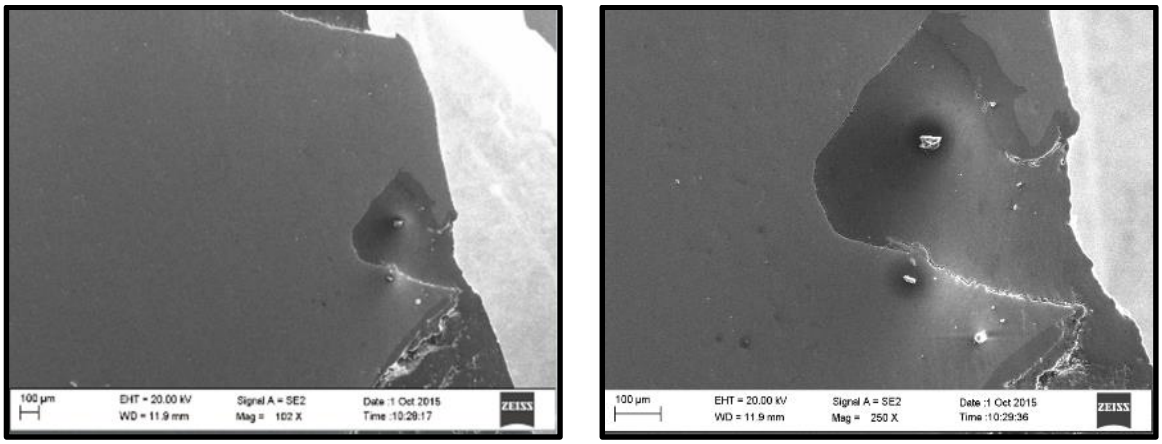

(a) (b)

Fig. D.14 525 °C 200 hour MP159-3 SEM SE2 Tool Pin Images at 100x (a) and 250x (b)

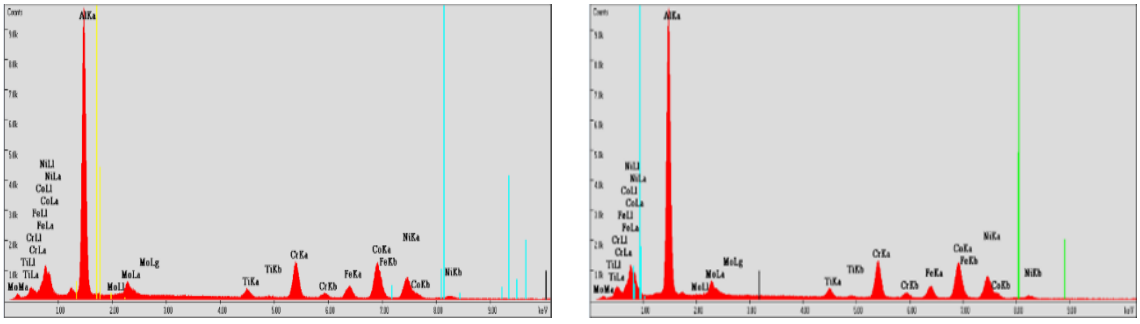

(a) (b)

Fig. D.15 Initial MP159-3 (a) & 525 °C 200 hour MP159-3 (b) EDS Spectrum